J. RHEE

PH.D.

2000

This is to certify that the

dissertation entitled

Automated Selection of Metal Poor
Stars in the Galaxy

presented by

JAEHYON RHEE

has been accepted towards fulfillment
of the requirements for

Ph.D. degree in Astrophysics

Major professor
T. Beers

Date 8/19/00

AUTOMATED SELECTION OF METAL-POOR STARS IN THE GALAXY

By

Jaehyon Rhee

A DISSERTATION

Submitted to
Michigan State University
in partial fulfillment of the requirements
for the degree of

DOCTOR OF PHILOSOPHY

Department of Physics and Astronomy

2000

ABSTRACT

AUTOMATED SELECTION OF METAL-POOR STARS IN THE GALAXY

By

Jaehyon Rhee

In this thesis I have developed algorithms for the efficient reduction and analysis of a large set of objective-prism data, and for the reliable selection of extremely metal-poor candidate stars in the Galaxy.

Automated computer scans of the 324 photographic plates in the HK objective-prism / interference-filter survey of Beers and colleagues have been carried out with the Automatic Plate Measuring (APM) machine in Cambridge, England. Highly automated software tools have been developed in order to identify useful spectra and remove unusable spectra, to locate the positions of the Ca II H (3969 Å) and K (3933 Å) absorption lines, and to construct approximate continua. Equivalent widths of the Ca II H and K lines were then measured directly from these reduced spectra. A subset of 294,039 spectra from 87 of the HK survey plates (located within approximately 30 degrees of the South Galactic Pole) were extracted. Of these, 221,670 (75.4%) proved to be useful for subsequent analysis.

I have explored new methodology, making use of an Artificial Neural Network (ANN) analysis approach, in order to select extremely metal-poor star candidates with high efficiency. The ANNs were trained to predict metallicity, [Fe/H], and to classify stars into 6 groups separated by temperature and metal abundance, based on two accurately measured parameters – the de-reddened broadband $(B\text{-}V)_0$ color for known HK survey stars with available photometric information, and the equivalent width of the Ca II K line in an 18 Å band, the K18 index, as measured from follow-up

medium-resolution spectroscopy taken during the course of the HK survey. When provided with accurate input data, the trained networks were able to estimate [Fe/H] and to determine the class with high accuracy (with a robust estimated one-sigma scatter of S_{BI} = 0.13 dex, and an overall correction rate of 91%).

The ANN approach was then used in order to recover information on the K18 index and $(B-V)_0$ color directly from the APM-extracted spectra. Trained networks fed with known colors, measured peak fluxes, and the raw fluxes of the low-resolution digital spectra were able to predict the K18 index with a one-sigma scatter in the range $1.2 < S_{BI} < 1.4$ Å, depending on the color and strength of the line. By feeding on calibrated, multiple-band, photographic measurements of apparent magnitudes, peak fluxes, and the fluxes of estimated continua of the extracted APM spectra, the trained networks were able to estimate $(B-V)_0$ colors with a scatter in the range $0.13 < S_{BI} < 0.16$ magnitudes.

From an application of the ANN approach, using the less accurate information obtained from the calibrated estimates of K18 and $(B-V)_0$ colors, it still proved possible to obtain metal abundance estimates with a scatter of S_{BI} = 0.78 dex, and to carry out classifications with an overall correction rate of 40%. By comparison with a large sample of known metal-poor stars, on the order of 60% of the candidates predicted to have a metallicity [Fe/H] < -2.0 indeed fell in this region of abundance (representing a three-fold improvement over the visual selection criteria previously employed in the HK survey). The recovery rate indicated that at least 30% of all such stars in our sample would be identified in a blind sampling, limited, for the most part, by the lack of accurate color information. Finally we report 481 extremely metal-poor star candidates in 10 plates of the HK survey, selected by our newly developed methodology.

For the glory of the Lord

ACKNOWLEDGMENTS

I sincerely express my respect and thanks to my advisor, Dr. Timothy C. Beers. In the course of my graduate study, I was able to learn from him how to observe stars and do science with them – invaluable experiences for my future research. He always encouraged me in the pursuit of research and kindly understood my situations in all aspects. I especially appreciate his proofreading to my thesis. He was a true teacher to me and this will remain in my mind forever.

I would like to thank Robert Argyle and Mike Irwin for carrying out the digital scans of all 324 HK survey plates for the past three years. Without their collaboration with the APM facility, this project would not have been possible. I would also like to thank my dissertation committee – Horace Smith, Eugene Capriotti, Suzanne Hawley, S. D. Mahanti, and Daniel Stump – for the classes I took from them and for their comments on my thesis. Thanks also to Robert Stein for offering a class in the format of a self-paced study, which made it possible to complete my course work on time.

I would like to acknowledge various financial supports of assistantships and fellowships from Department of Physics & Astronomy and Michigan State University. In particular, the Graduate School Dissertation Completion Fellowship enabled me to focus on writing and finishing up this thesis.

I wish to give many thanks to my father and mother for their endless love and prayers for me, and my parents-in-law for their ceaseless encouragement. Thanks also to my brother, Jaesuk, for his brotherliness and regards to me.

To my lovable son, Wonho, and daughter, Irene, I really appreciate their love and smiles by which I was cheered up. Finally I would like to express my great thanks and love to my wife, Seunghae. I am indebted to her devoted support and sacrifices that made it possible for me to study comfortably and to complete my graduate study successfully. The time we spent together for our studies at Michigan State will remain good memories in our minds forever.

TABLE OF CONTENTS

LIST OF TABLES

LIST OF FIGURES

Chapter 1

INTRODUCTION

1.1 From the Universe, to the Galaxy, to Stars

1.1.1 Universe

The Big Bang theory is the most generally accepted concept to explain the origin and evolution of the Universe. According to the theory, developed by Gamow, Alpher and Herman in the late 1940s and early 1950s (see Pagel 1997 for more details), the Universe originated from a singularity where everything - matter and radiation - was confined in an infinitesimally small volume, so the temperature and density were infinite. With a violent explosion about 15 billion years ago, the Universe began to expand, eventually cooling to the point where fundamental particles such as protons and neutrons could form. In the first few minutes following the Big Bang, light nuclei of H, D, ^{3}He, ^{4}He and ^{7}Li were created by primordial nucleosynthesis at a temperature on the order of 10^9 K, resulting in primordial mass fractions of 0.76 for hydrogen, 0.24 for helium, and 0.00 for metals (all elements heavier than helium). The current helium abundance in the Universe is much greater than that predicted by hydrogen burning in stars – only some form of early nucleosynthesis can explain this surplus.

During the first few 10^5 years, the Universe consisted of ionized baryonic gas that was opaque to radiation, and consequently was in thermal equilibrium. Cooling continued as the expansion continued. When the Universe was about 300,000 years old, at a temperature of about 3000K, the plasma became neutral by recombination (the capture of electrons by protons) and, for the first time, the Universe became transparent to radiation. Since that time, the cosmic background radiation has been red-shifted due to the expansion of the Universe. In 1965, Penzias and Wilson were able to observe this source of blackbody radiation with a temperature of about 3 K, whose intensity was nearly equal in all directions in space. Observations by the Cosmic Background Explorer (COBE), a NASA satellite launched in 1989, confirmed that the cosmic background radiation has a blackbody spectrum with a temperature of 2.73 K. The Hot Big Bang theory is strongly supported by these three observations: (1) the primordial abundances of light nuclei, (2) the existence of the cosmic background radiation, and (3) the expansion of the Universe.

In 1992, COBE also detected random irregularities of the microwave background in temperature on the order of 1 part in 10^5. This anisotropy is attributed to fluctuations of density (or expansion rate) when the Universe was about 10% of its current age. The expansion rate of gas in slightly denser regions became smaller than the average value and, eventually, it could decouple from the Hubble flow. Such gas clouds began to collapse to form galaxies, the fundamental "large scale" building blocks of our Universe. Several efforts to make three-dimensional maps of the Universe such as CfA Redshift Survey (Geller 1990; Da Costa et al. 1994) and others – the 2dF Galaxy Redshift Survey (Colless 1998, 2000) and the Las Campanas Redshift Survey (Bharadwaj 2000), reveal that the Universe is composed mostly of empty space surrounded with "walls" of galaxies. The distribution of galaxies is neither uniform nor random, but rather, has the appearance of soap bubbles.

1.1.2 The Galaxy

- **Thin Disk**

Our Sun resides in the Milky Way Galaxy, a prominent (though not the most luminous) member of the Local Group – a collection of N ~ 35 galaxies within a sphere of radius ~ 2 Mpc. Our Galaxy is a large spiral, whose main components are its disk and spheroid structures. The so-called thin disk consists of gas, dust, open clusters, and both old and young stars, collectively referred to as Population I. These move along roughly circular orbits around the center of the Galaxy, with rotational speed (at the Sun's location) of roughly 220 km/s, with no large component of velocity perpendicular to the disk. Population I stars have heavy elements abundances similar to those of the Sun and are believed to have been created from chemically enriched interstellar medium (ISM) by the ejecta of Type I and Type II supernovae, over the lifetime of the disk. The rotating disk has a mass of about 6×10^{10} solar masses, and a vertical scale height of 0.325 kpc. The diameter of the luminous portion of the disk is approximately 50 kpc. The Sun lies roughly 8 kpc away from the center, and is located perhaps 30 pc above the mid-plane.

- **Thick Disk**

It is generally accepted that thick disk is a constituent of the Milky Way Galaxy. The thick disk contains stellar components whose chemical and kinematical properties are intermediate between those of the thin disk and the halo, thus they are often referred to as Intermediate Population II (IPII). Although the metal abundance, [Fe/H], of IPII stars falls in the range $-1.6 < [Fe/H] < 0.0$, with a mean and a peak of metallicity distribution near $[Fe/H] = -0.6$, several recent investigations have proposed the existence of a metal-poor tail in the thick disk abundance distribution reaching to as low as $[Fe/H] = -2.0$ (the so-called metal-weak thick disk – see, e.g., Chiba & Beers 2000). The age of the thick disk is thought to be nearly the same as that of the halo, but it exhibits dynamical properties that are more similar to the thin disk. Relative to the stellar component of the thin disk, IPII stars rotate about the Galactic center with slower speeds and have a larger vertical velocity dispersion (roughly 60 km/s). The vertical scale height of the thick disk is roughly 1-1.4 kpc.

- **Bulge**

The central region of the Galaxy has a flattened and elongated bulge. The bulge, with a mass of $2\text{-}4\times10^{10}$ solar masses, is confined within a diameter of 2 kpc, and has a vertical scale height of roughly 0.4 kpc. As a whole, it has little gas and dust, and is thought to consist mainly of old stars. However, some young stars are found, along with signs with ongoing star formation, in the inner regions. According to studies of the abundance of the bulge populations (McWilliam & Rich 1994), metallicities for a sample of K giants cover a wide range, $-1.25 < [Fe/H] < +0.5$, with a mean value of $[Fe/H] = -0.25$, surprisingly somewhat lower than the mean abundance of stars in the solar neighborhood. In addition, the bulge does not appear to suffer from the so-called "G dwarf problem" - the lack of metal-poor stars compared to predictions of the Simple model - unlike the disk. From COBE surface photometry (Binney et al. 1997), the optical depth to microlensing (Alcock et al. 1995), and photometry of the millions of stars through Baade's Window (Stanek et al. 1994), there is convincing evidence for the existence of a bar attached to the Galactic bulge.

- **Halo**

The final luminous component of the Galaxy is the halo. The faint stellar halo has a roughly spherical distribution of stars that extend more than 100 kpc from the Galactic center. It is thought that there is little present-day star formation taking place in the halo, owing to the paucity of gas. The halo, which contains only about 1% of the stellar population of the Milky Way, is made up of individual field stars and globular clusters (themselves roughly 1% of the visible halo). The halo stars are believed to be older than most disk stars, and their ages of 14 to 17 billion years are comparable with the time which is thought to have elapsed since the epoch of Galaxy formation. They clearly posses lower abundances of heavy elements than stars in the disk. Their metallicity ranges from [Fe/H] = 0.0 down to [Fe/H] = –4.0, with a peak near [Fe/H] = –1.6. The G-dwarf problem does not appear to occur in the halo. These old, metal-poor stars and globular clusters, in the spheroidal components of the Galaxy (the bulge and the halo) are collectively referred to as Population II. Unlike the Population I stars in the disk, halo stars have "hot" kinemetical characteristics. They move with high velocities on highly elongated orbits around the Galactic center and show random orbits in 3 dimensional space (that is, not confined on the disk), hence their vertical velocity dispersions are quite large (typically in excess of 100 km/s).

- **Models of Galaxy Formation**

There are two extreme models for the formation of the early Galaxy: (1) a rapid and monolithic dissipative collapse, and (2) a gradual, fragmentary, chaotic collapse. Perhaps the first milestone associated with the former picture is the paper by Eggen, Lynden-Bell, and Sandage (1962, hereafter ELS). From 221 well-observed dwarf stars in their sample, ELS found correlations between ultraviolet excess (a property which correlates with metal deficiency) and (a) the orbital eccentricities, (b) vertical velocities with respect to disk, and (c) orbital angular momenta. They observed that a greater number of stars with high ultraviolet excesses (lower metal abundance) had a tendency to reside farther above the Galactic plane, with higher eccentricities and larger vertical velocities, than the stars with lower ultraviolet excess (higher metal abundance). These results led to a picture of a relatively rapid collapse scenario. According to the ELS model, about 10 billion years ago, the Milky Way formed from a single rotating and roughly spherical protogalactic cloud (with a radius of roughly 100 kpc) comprised of extremely metal-deficient gas. As the cloud cooled down, it collapsed rapidly in near free-fall over a timescale of a few times 0.1 billion years. This contraction resulted in condensations of gas, and then the formation of the first generation of globular clusters and metal-poor stars in the Galactic halo. In addition, the rate of rotation increased due to the conservation of angular momentum, and the gas became more flattened, eventually forming the Galactic disk. During this collapse, massive star formation and supernova explosions took place continuously, enriching chemical elements inside the Galaxy. This model predicted the existence of a metallicity gradient of the stellar population over the Galactic radius (larger radius → less metal abundance). Although the ELS model is consistent with their original observations, there have been numerous authors who have called into suspicion the effects of bias in the ELS sample selection (e.g., Sarajedini 1997).

The second picture for the formation of the Galaxy was derived from the landmark work of Searle and Zinn (1978, hereafter SZ). From their abundance studies for 19 globular clusters, SZ found that no radial abundance gradient exists for the clusters in the outer halo (beyond a Galactocentric distance of 8 kpc). This was contrary to the predictions of the ELS rapid-collapse model. SZ also found that the outer halo clusters exhibited no correlation between their metallicities, with a wide range of color distributions for stars on the horizontal branch (HB) (the 2^{nd} parameter problem), while the inner halo clusters showed little color dispersion in their horizontal branches of similar metallicities. Later, Zinn (1985) found that the older metal-poor globular clusters, with [Fe/H] < –0.8, are nearly spherically distributed around the Galactic center, while the younger, more metal-rich globular clusters with [Fe/H] > –0.8 primarily are found near the Galactic plane. These findings led to a gradual collapse scenario, which held that the Galactic halo was created from a large number of independent gas fragments, each of which evolved independently over a few billion years. Each fragment is predicted to possess its own chemical and dynamical history, hence a metallicity gradient with Galactocentric distance or height above the disk are not expected.

- **Halo Substructure**

Many kinematical and chemical studies for the stellar component in the Milky Way halo have suggested the possible existence of halo substructure. The halo field stars near the Galactic plane (less than about 3 kpc) appear to have metallicity gradient (Sandage and Fouts 1987), but no metallicity gradient seems to be present beyond about 5.5 kpc (Majewski 1992). The halo stars may exhibit two different rotational directions, although their speeds are relatively mild (a few times 10 km/s). Several studies reveal both pro-grade rotation (e.g., Norris 1986) and retrograde rotation (e.g., Majewski 1992) in the halo field stars. These discrepancies can be reconciled by suggesting the idea of dual halo populations: (1) high halo stars characterized by low metal abundance without metallicity gradient and a retrograde motion, and (2) low halo ("flattened potential") stars described by low metal abundance and mild pro-grade motion (Majewski 1993; Carney 1996). Recently, however, dynamical analysis for metal-poor stars selected *without* kinematic bias has recently revealed that the outer part of the halo presents no systematic rotation, whereas the inner part of the halo shows a pro-grade rotation and a highly flattened density distribution

(Beers & Sommer-Larsen 1995; Chiba & Beers 2000). In addition, these stars exhibit no apparent correlation between [Fe/H] and orbital eccentricity, contrary to previous results based on kinematically biased samples.

Armandroff (1989, 1993) found that the inner halo clusters (inside 8 kpc) exhibit a weak metal abundance gradient over Galactocentric distance and height above the disk, while SZ found no metallicity gradient for the outer halo clusters (outside 8 kpc), as seen above. Regarding to their geometrical arrangement, the inner globular clusters are distributed in a flattened manner, but the outer globular clusters are distributed in spherical way (Hartwick 1978). Like the field stars, there have been claims for the existence of a group of globular clusters in highly retrograde orbits (Rodgers & Paltoglou 1984), but recent measurements reveal that some globular clusters have a radially anisotropic velocity distribution and highly eccentric orbits (Dinescu et al. 1999). To harmonize these distinctive differences, Zinn (1993) proposed two populations by age for the Galactic halo: (1) the "Old Halo" in which globular clusters were formed during the collapse and so have little age variations and (2) the "Younger Halo" comprised of globular clusters that were accreted from satellite systems, are found at greater Galactocentric distances, and show a significant age spread.

Taking these results in together, the present consensus for the Galaxy formation scenario would be a mixture of ELS and SZ models. That is, the inner halo rapidly collapsed in a monotonic fashion during a few times 0.1 billion years, whereas the outer halo was created from a number of gas fragments that were accreted from satellite systems over much longer time scales.

1.1.3 Nucleosynthesis

The metal-poor stars of the halo and thick disk provide vital clues for unraveling the dynamical and chemical history of the Milky Way, and large spiral galaxies in general. Here, it is worth understanding the general process of chemical enrichment of the Universe after primordial nucleosynthesis. It is presently understood that the chemical elements (beyond H and He) which are found in the Universe today were produced by nuclear reactions that took place inside of stars. As explained already, hydrogen and helium were built up by cosmological nucleosynthesis in the few minutes following the Big Bang. Heavier elements (up to iron) can be synthesized by successive nucleosynthesis processes which occur during the main-sequence lifetimes of stars, though not exclusively. Stars with initial masses greater than about 8 solar masses become Type II supernovae at the end of their lifetimes, and produce the majority of the elements beyond the iron peak from explosive nucleosynthesis processes (by adding neutrons into elements through the r- and s-processes). These stars, as well as lower mass stars which end their lives more “peacefully,” but suffer mass loss over their extended lifetimes, eject heavy nuclei into interstellar space, so that subsequent generations of stars are produced from the more chemically enriched ISM. Stars with initial masses less than 0.8 solar mass have main sequence lifetimes that exceed the current age of the Universe, and hence, if formed at the early stages of our Galaxy’s life, should remain observable today. These low-mass metal-poor stars have “locked up” a record of the chemical composition of the ISM at the time of their formation, hence provide a tool for exploration of evolution of nucleosynthesis over the entire history of the Galaxy. The search for these very metal-deficient stars is the primary goal of this project.

1.2 Automation Techniques

Astronomy differs from many other sciences in several respects. The extremely long lifetimes of the objects of study, the difficulty in collecting data, and the impossibility of conducting controlled experiments with astronomical samples, to name just a few. These properties of data demand somewhat different approaches to astronomical research. Astronomers do observations (rather than experiments) on astronomical objects such as stars and galaxies, which are presently existing in the Universe. In order to understand the important physical properties and processes, a large number of spectra and images need to be collected over a wide range of physical parameters (e.g., temperature, abundances, and age). Such statistical approaches have led astronomers to develop many fruitful and powerful theories – such as stellar evolution and the formation and evolution of the Milky Way.

As an example it is beneficial to review a historical development of the Henry Draper Catalog – a cornerstone work closely related to stellar classification (Hearnshaw 1986, 1987). Annie Cannon (1863-1941) made 225,300 spectral classifications from the collection of Harvard objective-prism plates from October 1911 to September 1915, and they were published as the Henry Draper Catalog in nine volumes of the Harvard Annals (Cannon and Pickering 1918-1924). She continued her research to publish 47,000 spectral classifications as the Henry Draper Extension (Cannon 1925-1936) and additional 87,000 spectral classifications as Henry Draper Extension Chart (Cannon 1949). Obviously, this was a monumental effort, but some questions arise as to the suitability of the methodology employed. Classifications were performed by a well-trained classifier by comparing the overall appearance of new spectra to that of standard spectra. This method takes a great deal of time. For example, Cannon was able to classify about 400,000 stellar spectra in about 30 years, which corresponds to an average of only 37 spectra per day, although she was an excellent classifier. In addition, such a qualitative analysis may suffer from lack of objectivity. Even the same classifier could easily classify the same stellar spectrum into two different classes, depending on a wide variety of variables. Finally, each new classifier needs to spend a great deal of time in learning detailed criteria to distinguish spectra which have small differences. With the improvement of astronomical instrumentation, large numbers of spectra and images can now be obtained very rapidly, for example, the Sloan Digital Sky Survey (SDSS 2000), the Global Astrometric Interferometer for Astrophysics (GAIA) (Lindegren et al. 1996; Perryman et al. 1997), the APM Survey (Maddox et al. 1990), and the 2dF Galaxy Redshift Survey (Colless 1998, 2000). Efficient processing of such large databases, which offer the advantages of speed, objectivity, and comparability between different researchers, has been an interesting challenge for the astronomical community.

Zekl (1982) developed a FORTRAN program to classify 117 digitized stellar spectra based on various properties (e.g., equivalent widths and half-widths) of spectral lines for 58 standard stellar spectra. This effort produced a mean error of 0.7 subclasses in spectral classification, and favorable results for the early type stars of classes V-III in luminosity classification. In his Ph.D. thesis, Kurtz (1982) made use of cross correlation and the techniques of multivariate analysis and pattern recognition to classify low-resolution (14 Å) stellar spectra. The cross-correlation method obtained a poor luminosity classification and a mean error of 2.2 subtypes for non-supergiants in the spectral range B0 to M2. Kurtz also demonstrated that O-type stars and supergiants earlier than A5 can be selected by principal component analysis. LaSala (1994) has applied metric-distance techniques for the classification of some 250 low-resolution stellar spectra.

New methodology is now revolutionizing the analysis of large astronomical databases. One exampel of this, the Artificial Neural Network (ANN) technique, is a computational tool that began to be applied actively in various fields of astronomy in the early 1990's, and varied uses of ANNs have been expanding with time. Wider applications of ANNs in astronomy can be found in Miller's paper (1993) and the 38th volume of Vistas in Astronomy (Storrie-Lombardi et al. 1994). In general, the applications of ANNs can be divided into stellar classification, estimation of physical parameters, star/galaxy separation, and galaxy classification, as follow.

von Hippel et al. (1994) used ANNs for stellar classification of 575 stars, and reported temperature classification better than 1.7 spectral subtypes, from B3 to M4. Gulati et al. (1994) applied ANNs to classify a set of 158 test spectra into 55 spectral types. The training set was able to classify the test set with a one-sigma error of 2 spectral subclasses. ANNs were used with equivalent widths in spectral classification of the near-infrared spectra of A-type stars to produce an accuracy of 0.4 subclasses in temperature and 0.15 classes in luminosity (Weaver & Torres-Dodgen 1995). These authors further showed that ANNs could classify O to M-type spectra, with 512 stellar flux values, to an accuracy of about 0.5 subclasses in temperature and about 0.25 classes in luminosity (Weaver & Torres-Dodgen 1997). Vieira & Ponz (1995) made use of both metric-distance techniques and ANNs for the classification of low-dispersion spectra of stars in the spectral type range O3 to G5 taken with the International Ultraviolet Explorer. It turned out that ANNs were able to classify with an accuracy of 1.1 spectral subclasses, which was a substantially better results than obtained with the metric-distance approach. ANNs have been employed in two-dimensional MK classifications with a set of over 5000 optical spectra to report on an accuracy of 0.82 subtypes in the range of spectral types B2 to M7, and correction rate for luminosity classes over 95 percent of both dwarfs and giants (Bailer-Jones et al. 1998a). Singh et al. (1998) trained multilayer back-propagation networks with a set of 55 spectra compressed by principal component analysis in the range of O to M and obtained as good as 2.24 subtypes of 1 sigma error for unseen 158 spectra.

Bailer-Jones et al. (1997) trained ANNs with a set of 155 synthetic spectra to yield effective temperatures for 5000 observed stellar spectra (B-K type), and their temperature calibration agreed well with those in the literature. In order to determine physical parameters for a large number of stars on GAIA mission, ANNs have been trained to map from a large grid of synthetic spectra to physical parameters, as a function of spectral resolution and signal-to-noise ratio (SNR) (Bailer-Jones 2000). The trained network had the ability to predict effective temperate and metal abundance with accuracy of 1% and 0.2 dex respectively, and surface gravities, log g, with an accuracy of 0.2 dex, for stars earlier than G type. Prieto et al. (2000) used ANNs to obtain estimates of [Fe/H] and $(B\text{-}V)_0$ colors for 731 stars from several spectral indices, and found 12 new stars with [Fe/H] < –3.0. ANNs were employed to estimate the same parameters from moderate-resolution stellar spectra (Snider 1999). The trained network produced effective temperature, log g, and [Fe/H] with internal one-sigma errors of 121 K, 0.17 dex, and 0.11 dex, respectively.

Odewahn et al. (1992) used ANNs to separate images into either star or galaxy classification based on a set of 14 image parameters. The trained discriminators were able to separate images with success rates of 99% for objects of B <= 18.5 and over 95% with 18.5 <= B <= 19.5. Odewahn et al. (1993) trained ANNs that could discriminate between stars and galaxies with a success rate of 90% in the range 19.5 < B < 20.0. Bazell (1998) showed the networks trained with somewhat high-resolution (17 × 17 pixel) images could separate objects with over a 93% success rate.

An ANN was used to perform morphological classification of galaxies from 13 galaxy parameters and generated a success rate of 64 % only for exact matching and 90 % including class of 2nd highest probability (Storrie-Lombardi et al. 1992). Naim et al. (1995) made use of ANNs to morphologically classify galaxies and achieved an rms error of 1.8 Revised Hubble types.

1.3 Goals of the Thesis

Metal-poor stars identified in the HK objective-prism/interference-filter survey of Beers and colleagues so far have successfully answered many aspects of early nucleosynthesis and chemodynamical history in the Milky Way (see Chapter 2). However, one must keep in mind that a large fraction of the cooler metal-poor stars on the HK survey have likely been missed by the visual selection procedure that was previously employed. Therefore, we still need to collect additional metal-deficient stars at a wider range of temperatures, in order to assemble a more representative data set.

We are in the process of selecting new candidate metal-poor stars based on automated digital scans of the HK survey plates with APM (Automatic Plate Measuring) facility at the Institute of Astronomy in Cambridge, England. These new identifications are of particular value because they will not suffer from the biases and confounding of the sample, especially among the cooler stars, as did the visual selection. As of July 2000, all 324 usable plates from the HK survey have been scanned and over 1.5 million stellar spectra have been extracted from these plates.

The goals of the thesis are: (1) to develop and refine an algorithm for the optimal identification and analysis of "interesting" stars from the digitally scanned HK survey plates, (2) to investigate the application of artificial neural networks with the equivalent width of Ca II K line and broadband $(B-V)_0$ color in the identification of metal-poor stars, and (3) to construct a new set of candidate metal-poor stars in the direction toward the South Galactic Pole. This new data set will be used to direct subsequent photometric and spectroscopic follow-up efforts that will provide us with a deeper understanding of the kinematic history and chemical evolution of the Galaxy.

1.4 Chapter Overview

In Chapter 2, the history of the HK survey is briefly reviewed and its results are discussed. The APM (Automatic Plate Measuring) system for digital scans of the HK plates is introduced. Algorithms developed for efficient data reduction are explained and the results are summarized.

Chapter 3 presents the application of an Artificial Neural Network (ANN) to known metal-poor stars. ANNs of various architectures are trained from known color $(B-V)_0$ color and K18 index to predict metallicity, [Fe/H], and classify stars into 6 groups divided by temperature and metal abundance.

K18 index calibration derived directly from scanned spectra is demonstrated in Chapter 4. Metallicity and classifications of stars are determined by the trained network feeding on known colors and estimated K18 index derived from the calibration process.

In Chapter 5, $(B-V)_0$ color calibration is performed by making use of various kinds of magnitudes and fluxes of the digitized continua from the prism spectra. The trained networks predict [Fe/H] and the classes of stars from the estimated colors and K18 indices. The efficiency and recovery of the results are discussed. Re-calibration methods are suggested to improve results.

In Chapter 6, new extremely metal-poor candidate stars, which will form targets for new spectroscopic follow-up in the near future, are selected by employing the methodology developed previously.

Chapter 7 presents the conclusions of this thesis and suggestions for future work. A general introduction to ANNs is provided in the Appendix.

Chapter 2

DATA REDUCTION

2.1 The HK Survey

The HK prism survey of Beers and collaborators has been extremely successful in the identification of large numbers of metal-deficient stars in the thick disk and halo of the Galaxy. Since we are making use of the same objective-prism plates as originally employed in the HK survey, it is valuable to review the particulars of this approach. Much more detailed information can be obtained from inspection of Beers et al. (1985), Beers et al. (1992), Beers (1999a), and Christlieb (1999).

In 1978, George Preston and Stephen Shectman of the Carnegie Observatories of Washington initiated the HK interference-filter / objective-prism survey, in order to identify large numbers of metal-poor and field horizontal-branch (FHB) stars in the Milky Way. There were on the order of 70 usable prism plates in this original effort. Beers joined the program in 1983, and by 1992, had expanded the survey by obtaining additional 240 plates in the southern and northern hemispheres. In total, 367 wide-field ($5^{\circ} \times 5^{\circ}$) plates were obtained – 211 plates in the southern hemisphere using the 61-cm Curtis-Schmidt telescope at the Cerro Tololo InterAmerican Observatoiry (CTIO; 103aO emulsion, 90 minutes exposure) and 156 plates in the northern hemisphere using the 61-cm Burrell-Schmidt at Kitt Peak National Observatory (KPNO; IIaO emulsion, 90 minutes exposure). Not all of the plates were useful for survey work – some suffered from poor focus, others from too much plate fog from moonlight, and others were repeats obtained for the purpose of providing cross-checks. After elimination of these, roughly 7,000 square degrees ($1/6^{th}$ of the entire sky) are covered by the remaining 275 unique plates.

In the HK survey approach, an interference filter near the focal plane restricts the bandpass to 150 Å centered near the Ca II H and K lines at 3950 Å. The interference filter enables long exposures without undue sky fog or confusion of the spectra. The faintest stars in the HK survey have apparent magnitudes B ~ 15.5 – 16.0, several magnitudes fainter than that obtained by previous surveys using the objective-prism technique. The effective spectral resolution is seeing dependent, but is typically 5 Å. Visual scans of the HK plates were performed (originally by Preston, later by Beers) using a 10X binocular microscope. From the visual inspection a variety of interesting objects were identified. These include metal-poor F- and G-type stars (identified from their weak or absent lines of Ca II K), FHB- and other A-type stars (identified from the strength of the H-ε line, which dominates the Ca II H line for hotter stars), as well as subdwarf O- and B-type stars, white dwarfs, and emission-line objects.

However, as a result of the visual search for candidate metal-poor stars, a severe selection bias was introduced into the sample. Since for cooler stars (with broadband colors $(B-V)_0 > 0.6$) the resonance line of Ca II K line remains quite strong even at relatively low metallicities ($[Fe/H] < -2.0$), visual inspection without the benefit of color information could easily overlook these stars, as they appear quite similar to the more metal-rich, but slightly hotter stars, that dominate the population of bright stars in the solar neighborhood. The recovery of those cooler metal-deficient stars is one of the goals of this thesis.

To date, broadband UBV photometry and medium-resolution (1-2 Å) spectroscopy have been obtained for roughly half of the low metallicity candidates in the HK survey. Thus far, broadband photometric observations have taken place for roughly 5,000 candidate stars, and is being used in estimation of metallicities and distances to the stars (Preston et al. 1991; Doinidis et al. 1990, 1991; Norris et al. 1999). In addition, intermediate-band Stromgren photometry for some 750 survey stars was obtained by Anthony-Twarog et al. (2000). Spectroscopic observations of 1,044 metal-poor HK survey stars was reported by Beers et al. (1992). A large set of new spectroscopic results for some 5,000 metal-deficient stars, observed in collaborative works using telescopes at the European Southern Observatory, the Isaac Newton Telescope on La Palma (Canary Islands), Siding Spring Observatory in Australia, as well as at KPNO, will be submitted for publication soon (Cayrel et al. 2000, Rebolo et al. 2000, Norris et al. 2000, Beers et al. 2000).

Estimation of stellar metal abundance, based on the medium-resolution spectroscopy and broadband photometry (where available), is made with two complimentary methods (Beers et al. 1999). The first technique uses empirically derived relations between the equivalent width of the Ca II K line (3933 Å), metallicity [Fe/H], and de-reddened $(B-V)_0$ color. The second method is based on a Fourier Auto-Correlation Function (ACF), as originally described by Ratnatunga & Freeman (1989). The former approach is useful for metal-poor stars with [Fe/H] < -1.5, while the latter is particularly efficient for stars with [Fe/H] > -1.5, where the strength of Ca II K line begins to saturate as metallicity increases. The combination of these methods yields an acceptably small error (on the order of 0.15 – 0.20 dex) in the determination of stellar metal abundance over the entire range of abundance exhibited by stars in the Milky Way, $-4.0 <$ [Fe/H] < 0.3. Figure 2.1 shows a distribution of the equivalent width of the Ca II K line (as measured of a band of 18 Å width – designated as K18), and de-reddened color, $(B-V)_{0,}$ for stars of various

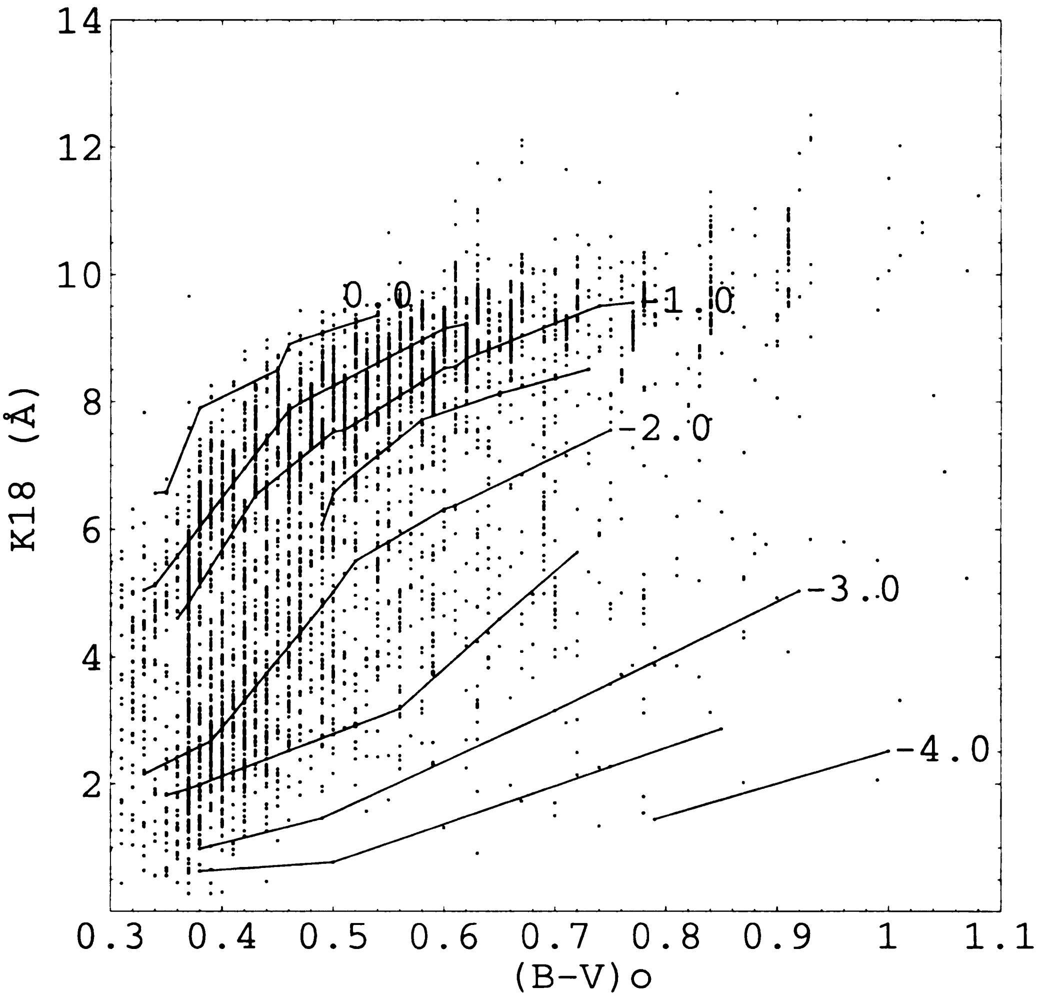

Figure 2.1 Distribution of K18 index and de-reddened color $(B-V)_0$ color for stars of various metallicities. Iso-metallicity contours are drawn with increments of 0.50 dex.

metallicities. A few curves are drawn by passing lines through data points whose metal abundances are the same. It is clear that lower metallicity stars exhibit smaller K18 at a given $(B-V)_0$. At a given metalicity, the cooler stars have relatively larger K18 than the hotter stars. In Chapter 3, we train Artificial Neural Networks (ANNs) to assign [Fe/H] as a function of K18 and $(B-V)_0$.

Observational follow-up of the HK survey has produced a list of some 4,700 metal-poor stars in the halo and thick disk of the Galaxy – including about 1,000 stars with [Fe/H] < –2.0 and roughly 100 stars with [Fe/H] < –3.0. As defined by Beers (1999b), the effective yield (EY) enables us to quantify the efficiency for the detection of stars of interestingly low abundance among the metal-poor candidates

$$EY_x \equiv \frac{N_{stars} \; with \; [Fe/H] < x}{N_{stars,observed}}$$

where *x* represents the target metallicity. For the HK survey the EY of stars whose metallicity is less than [Fe/H] = –2.0 is 32% (11%) with (without) previous B-V color information. The EY decreases to 11% (4%) for stars with [Fe/H] < –2.5. We expect to increase the EY by at least a factor of two using the candidate metal-poor stars derived from this thesis work.

Figure 2.2 is a histogram of the metallicity distribution for some 4,700 metal-poor HK survey stars. The dip in the distribution near [Fe/H] ~ –1.5 is attributed to the bias in the visual selection for cooler stars, mentioned above. However, it should be noted that extremely metal-poor stars (with [Fe/H] < –2.5) do not suffer from this selection bias, since the strength of Ca II K line is reasonably weak even for cooler stars. Another particularly important result from this figure deserves emphasis – the apparent ABSENCE of metal-poor stars with metallicity less than [Fe/H] = – 4.0. IF this limit proves consistent with the actual termination of the low end of the

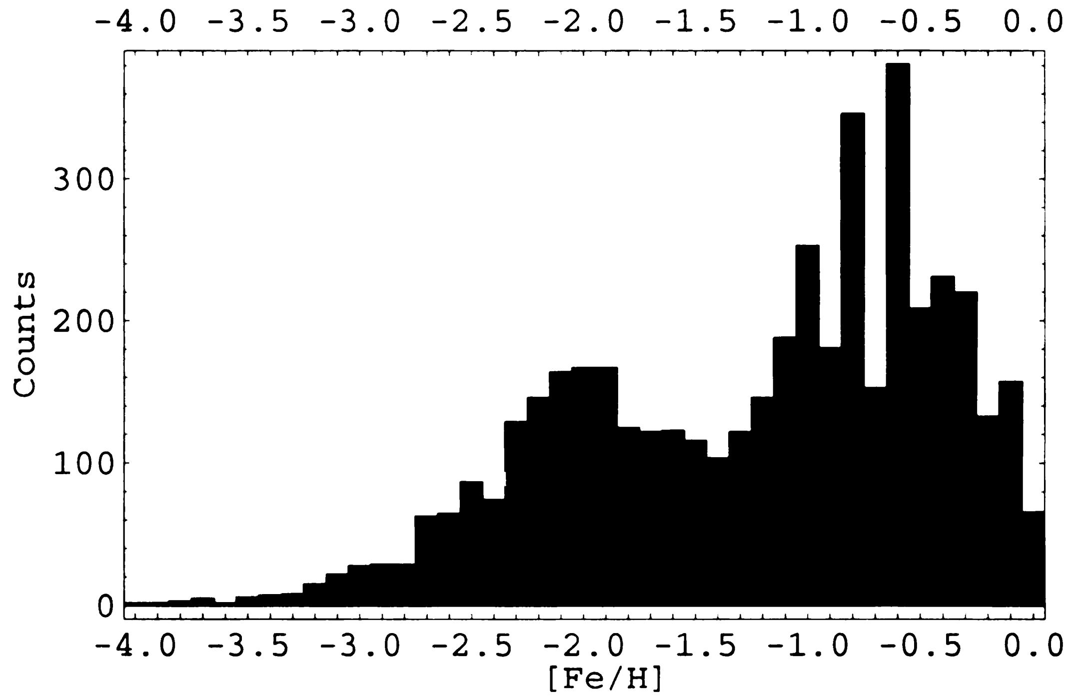

Figure 2.2 Histogram of the metallicity distribution for 4688 metal-poor stars selected in the "visual" HK Survey (HK1). Bins are 0.10 dex in width.

metallicity distribution function, this discovery is not consistent with the predictions of the so-called Simple Model (or closed-box model) of Galactic chemical evolution, which assumes that initial material in the Galaxy was absolutely free from heavy elements (Talbot et al. 1971; Hartwick 1976). This means that the extant oldest stars were created from an interstellar medium which was chemically polluted by the very FIRST generation of (presumably, quite massive) stars. A number of interesting projects which are suitable for exploration of these ideas, based on high-resolution spectroscopic information for the most metal-poor HK survey stars, are already underway at a number of 8-10m class telescopes (the Very Large Telescope in Chile; SUBARU and KECK in Hawaii).

2.2 The Automatic Plate Measuring System

As part of this thesis effort, a total of 324 HK survey plates have been digitally scanned in collaboration with Robert Argyle and Mike Irwin of the Institute for Astronomy, located in Cambridge, England, using the Automatic Plate Measuring machine (APM – Irwin et al. 1984; Kibblewhite et al. 1984; Cawson et al. 1987; Irwin 2000).

The APM was specifically designed to efficiently scan large data sets (images or spectra) from large-scale (e.g., $6^{\circ} \times 6^{\circ}$) photographic plates. It is composed of a speedy and precise laser scanning micro-densitometer and a series of on-line computers to process the data. The APM has the ability to process over 10 Gbytes of information per day, extracting the physical parameters for about 1 million images. Over 1,000 plates can be digitally scanned per year.

Typically, a two-pass procedure is required for obtaining measurements with the APM. The first pass is the estimation of sky background at all positions, derived from

2

A

f

c

fi

b

st

re

re

to

fog

29

are

an array of 64 × 64 intensities in each partitioned pixel. On the second pass, an image scan is performed to extract useful stars or galaxies by filtering all images with intensities larger than a specified isophote. In its objective-prism mode, the APM generates a data set of intensity verses approximate wavelength directly from the spectra identified on the plates.

Once fully processed, the extracted spectra of the digitally scanned HK survey plates are free from sky background, and provide the basis for a quantitative analysis which should enable us to avoid the selection bias incurred in the original visual inspection approach.

2.3 Semi-Automated Data Reduction

As of June 2000, 293 plates in the HK survey were digitally scanned with the APM facility. The processing of the remaining of 31 plates was done by July 2000, completing the digital scans of a total of 324 (available) plates in the HK survey. The first set of 293 scanned plates form the basis for this thesis work; the other plates will be included in our final set of analysis. Hereafter, the data set of known metal-poor stars identified during the observational follow-up of the visually selected stars will be referred to as "HK1." Those stars selected from the digitally scanned plates will be referred to as "HK2."

The number of useful HK2 spectra differs from plate to plate (from roughly 2,000 to 15,000), depending on the direction in which the plate was taken, and on the sky fog of that particular exposure. A total of 1,447,395 stellar spectra were found in the 293 plates – each plate contains 4,939 stellar spectra on average. If all 324 plates are considered, the total number of stellar spectra is expected to be well over 1.5

million. In this context I was motivated by an obvious task – "How can I process such a huge data set in efficient way?"

As mentioned in Section 2.1, the stellar spectra in the HK survey were obtained over a relative short wavelength range of 150 Å, including Ca II K (3933 Å) and H (3969 Å) lines. Depending on the accuracy of the wavelength calibration of the online APM processing, each plate can have different pixel numbers assigned for the positions of H and K lines in the digital spectra, even though the differences in pixel number between two lines are same. Therefore, the general procedure for data reduction will be: (1) obtain positions of Ca II H and K lines, (2) construct an appropriate stellar continuum, and (3) to calculate equivalent widths of those lines. However, one should keep in mind that this method is applicable to useful stellar spectra only. Thus, classifying unusable spectra needs to be a part of the data reduction procedure, and a procedure for filtering out these spectra, with little manual intervention, had to be designed.

2.3.1 Positioning the Ca II H and K lines

Figure 2.3 (a) is a representative stellar spectrum from the digitally scanned plates (HK2). From a match of its positional coordinates with known metal-deficient stars in HK1, it turns out to be a cooler metal-poor star (the HK1 Star: CS 22948-091) with [Fe/H] of –2.01 and $(B\text{-}V)_0$ of 0.61. In the title of the spectrum, the first 5 digits (22948) stand for ID number of plate, and the second 4 digits (3812) refers to HK2 ID number of star. Right Ascension (RA) and Declination (DEC) are shown in the upper left-hand corner, and the spectrum is classified as normal (i.e., useful) by the algorithms described below. The absorption lines near pixel numbers 130 and 155 are the Ca II K line and H lines, respectively. The positional difference between the

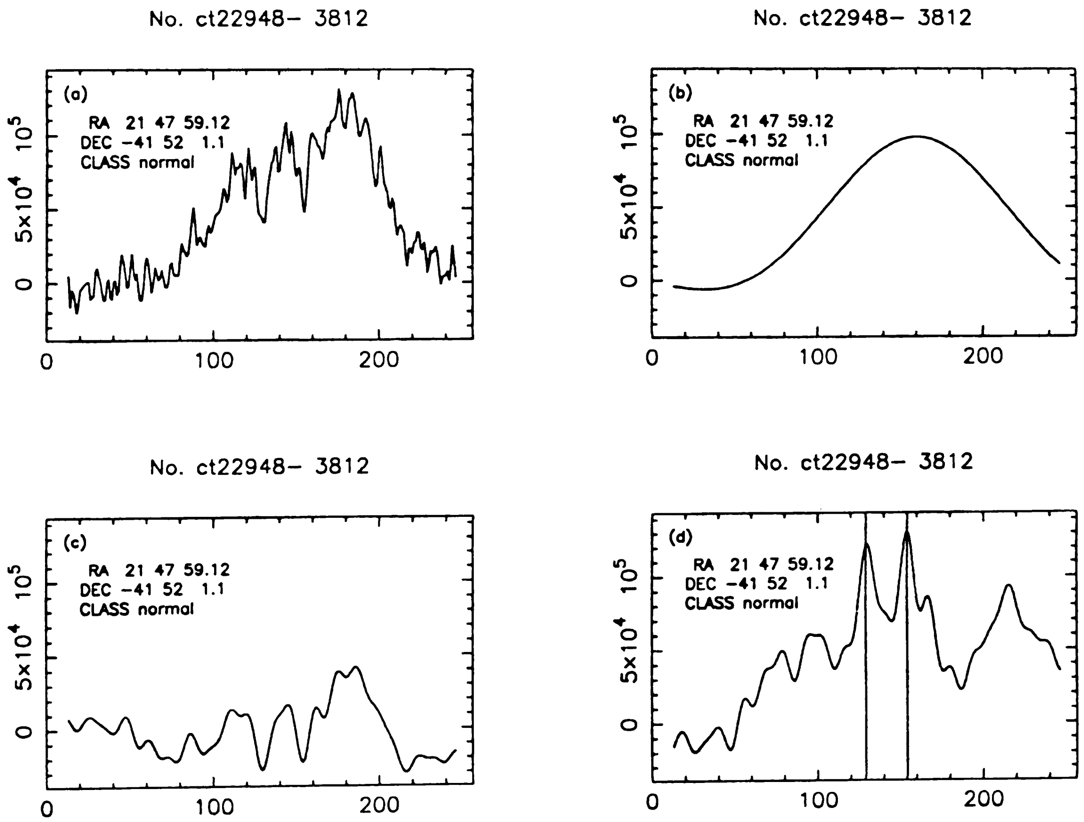

Figure 2.3 Positioning of the Ca II H and K lines in a representative stellar spectrum from HK2. (a) the raw spectrum, (b) very low frequency information, (c) intermediate frequency information, and (d) the difference between (b) and 1.5 × (c). From this curve, the positions of the Ca II H and K lines are readily identified.

absorption lines is about 25.3 pixels (= 34.81 Å) on average, derived by considering 3269 HK2 spectra for known metal-poor stars (in Chapter 4).

A Fast Fourier Transformation (FFT) approach was employed to find the positions of the Ca II H and K lines in an automated fashion. Figure 2.3 shows the raw extracted stellar spectrum (hereafter, referred to as "flux") spanning 256 pixels. Before the flux is passed into into the FFT program, it is extended to cover 512 pixels by adding (1) the half of an average of last 10 fluxes over 5 pixels and (2) appending zeros over 123 pixels on both the right-hand side and left-hand side (i.e. 512 = 123 + 5 + 256 + 5 + 123). This is useful because improved Fourier components can be obtained, and the rapid decline of low-pass filtered fluxes can be avoided when the spectrum is shifted to the right side or left side. Figure 2.3 (b) presents *very* low frequency information, which is obtained by Fourier transforming the extended raw spectrum into frequency domain, passing only first 4 lowest Fourier components (low-pass filter), and then reverse Fourier transforming back into the real domain. Intermediate frequency information in Figure 2.3 (c) can be obtained by passing the 4^{th} to 43^{rd} lowest Fourier components. The difference between the very low frequency information (overall shape) and three halves of the intermediate frequency information (absorption line information without overall shape and noise) is shown in Figure 2.3 (d). The Ca II H or K lines occur at the pixel locations of the highest values on this curve. By scanning its neighbor pixels, the pixel of the second highest value is found (and is either the Ca II H or K line, depending on the temperature and metallicity of the star). In this example, the left one of them is the Ca II K line.

As possible approaches to accomplish this job automatically, the techniques of cross-correlation and local minimization have been employed. By cross-correlating a spectrum with a "standard spectrum" that contains distinctive absorption lines with a good continuum, the positions of the absorption lines can be identified from the maximum of the cross-correlation function. However, this method does not always work well for these spectra, since the presence of the absorption lines themselves sometimes broadens the correlation function to the point that its peak is difficult to determine with accuracy. In order to use the local minimization approach, the spectra need to be smoothed to the point that they exhibit absorption lines only, and a minimum of noise. However, it is impossible to get rid of all the valleys in the spectra due to noise without distortion of true absorption lines. The algorithm with FFT ensures very stable results in the determination of positions of Ca II H and K lines, thus only this method was used in the end.

2.3.2 Construction of Continuum

Once the positions of Ca II K and H lines are determined, the construction of spectral continuum follows. Figure 2.4 (b) shows low frequency information derived by passing the first 40 lowest Fourier components. This curve contains Ca II H and K line information above the continuum. By scanning neighboring pixels of both lines, three points are determined – the position where the K-line absorption begins, where the K-line ends (set to the position where the H-line begins), and the positions where the H-line ends. As can be seen in Figure 2.4 (c), the absorption line information is then removed and a linear interpolation is performed over the three points. Finally, the Savitzky-Golay smoothing filter (Press et al. 1992) is passed across the entire flux distribution to produce the continuum shown in Figure 2.4 (d). The Savitzky-Golay smoother works by replacing the flux at a given pixel with the summation of differently weighted fluxes surrounding the pixel. The central pixel at a

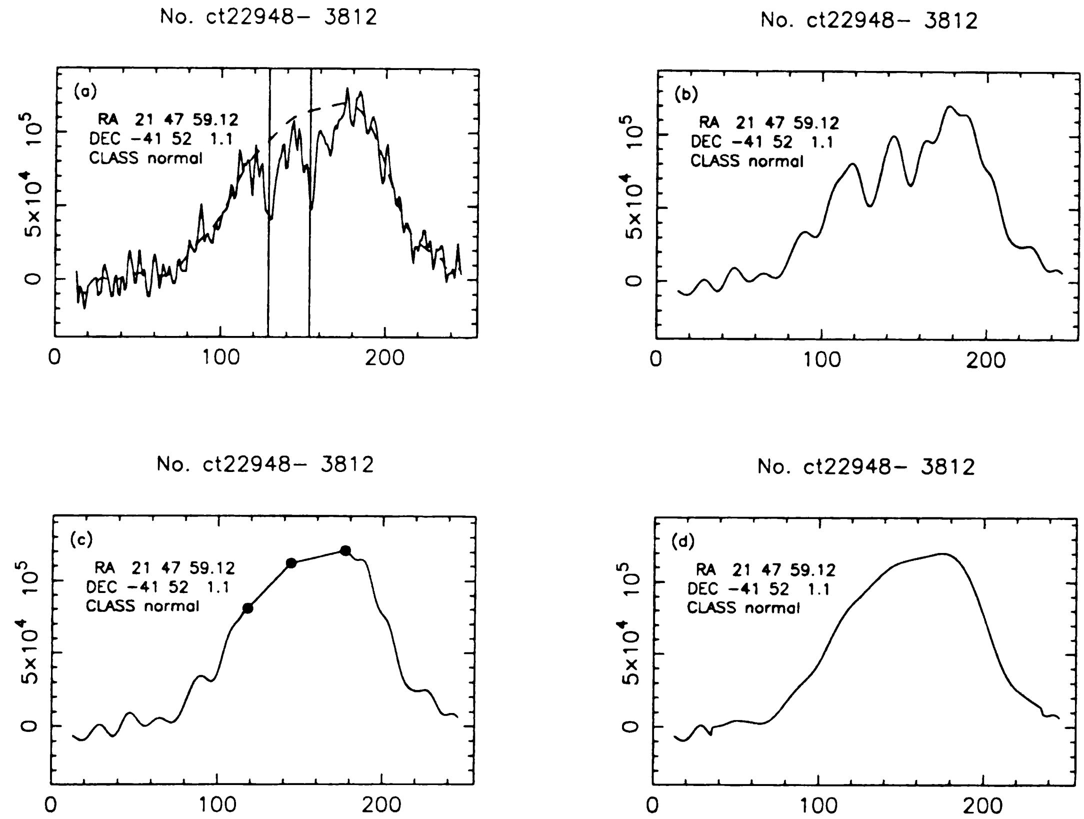

Figure 2.4 Construction of the stellar continuum. (a) raw spectrum (solid) with its continuum (dashed), (b) low frequency information, (c) linear interpolation over the ends of absorption lines, and (d) the continuum obtained by smoothing

box has the highest weight. A box with 33 pixels was used in the smoothing process. The raw stellar spectrum (solid line) with its continuum (dashed line) is shown in Figure 2.4 (a).

Lasala et al. (1985) have developed a method of spectral rectification by division of the raw spectrum by a very low-pass filtered spectrum. This fast and reliable technique is argued to obtain better results than the method that just removes low-frequency information from the raw spectrum. However, this method is not applicable to our case, because our spectrum spans a relatively short pixel range (256 pixels), so that the very low-passed frequencies do not allow the construction of appropriate continuum (especially when the spectrum is shifted too much). As one possible alternative, the combinational use of median and boxcar filtering might prove useful (e.g., Bailer-Jones et al. 1998b).

2.3.3 Equivalent Widths

With the raw spectrum (flux) and its continuum in hand, the estimation of equivalent width is straightforward. The equivalent width indicates the strength of an absorption line relative to its continuum. The division of flux by continuum is called a profile. The equivalent width is estimated by integration of the depth (= 1- profile) over a given bandpass. In our case, the integration was performed over 13 pixels (= 18 Å) around the Ca II H and K lines – the results are referred to as H18_2 and K18_2, respectively.

2.3.4 Classification of Useful / Unusable Spectra

Although the objective-prism technique produced large numbers of useful stellar spectra, it also produces a variety of unusable stellar spectra, which occur for reasons such as:

(1) Saturated spectra: The brightest stars in the HK survey have apparent magnitudes B ~ 11.0. Most of the fluxes in spectra of these stars (or brighter) are greater than the maximum value to which the photographic emulsion could respond, so the Ca II H and K lines look very weak or disappear completely.

(2) Noise (and null) spectra: The faintest stars in the HK survey have apparent magnitudes B ~ 15.5 – 16.0. In this case, the fluxes are comparable to plate noise, thus the Ca II H and K lines cannot be identified appropriately.

(3) Multiple spectra: Two (or more) spectra can be presented in a spectrum. This can happen when a star's light dispersed by the objective prism overlaps with the spectrum of a neighboring star.

(4) Odd spectra: Some spectra show a tendency of flux that linearly increases or decreases. Some others present unexpected features. The cause of these odd spectra is not known in all cases, but it is often associated with spectra from the edges of the plates, which become distorted by the imperfect field flattening of the Schmidt corrector used in combination with the objective prism.

The unusable spectra were identified and ruled according as follows. If the ratio of the low-pass filtered flux (Figure 2.4 (b)) at the Ca II H line, as compared to the filtered flux at the point where Ca II H line ends, is greater than 0.80, the spectrum was classified as saturated (the flat portion of the generally rising spectrum indicating that the star is saturated). Noisy spectra were filtered out if the maximum of the raw spectrum is less than 30,000 counts. In case of multiple spectra, the brighter stars are picked up as useful spectra, but human inspection was required to make sure whether they were contaminated by their neighbors or not. If the correlation coefficient between an arbitrary linear line and 120 raw fluxes (Figure 2.3

(a)) around the maximum of very low-passed spectrum (Figure 2.3 (b)) is greater than 0.87 (or less than -0.87), the spectrum is classified as linearly increasing (or decreasing). If there are any absorption lines, experimentation revealed that the correlation coefficient can not attain values as high as 0.87. Also, if the two highest points are not identified (unlike Figure 2.3(d)) in process of locating the Ca II H and K lines, the spectrum is classified as "odd." Nonetheless, there do exist some (rare) unusable spectra which cannot be detected by previous methods. These unusable spectra need to be identified by human inspection.

2.3.5 The Complete Data Reduction Procedure

For each plate, three steps were involved for reducing spectra. In the first step, a program was designed which classifies spectra into useful and unusable (i.e. saturated, noisy, and odd), and displays for consideration only the useful spectra, with the position of Ca II H and K lines marked. If some spectra need to be considered again (due to wrong positions of absorption lines or wrong classification), they are marked to be treated in the second step by human intervention. A second program displays the saturated, odd, and marked spectra that were derived from the first process. Some of these spectra can be "salvaged" with human intervention. Those that appear possible are identified, and the positions of the Ca II H and K lines are determined interactively. With the positions of lines for the useful spectra (the vast majority having been selected by the first program, and the remainder from the second program), a third program is then run to construct continuum and estimate equivalent widths of Ca II H and K lines as described above. It turns out that the complete processing time required for one plate is about 45 minutes, including resting of the of human classifier. It is interesting to note that this time is roughly equivalent to that required for a single pass at visual inspection of an entire plate, though of course the return of information is orders of magnitudes greater.

Table 2.1 shows data reduction statistics for the 87 plates used in the remainder of this thesis work, selected to the plates covering the South Galactic Cap, corresponding to plates with Galactic latitudes in the region of b < -55. The column translations are as follows:

Column (1):	Plate ID in the HK survey
Column (2):	The number of digitally scanned stellar spectra on the plate
Column (3) & (4):	The number of stellar spectra identified as useful and its percentage as compared to the total number of extracted spectra on the plate (= Col(3) / Col(2) * 100)
Column (5) & (6):	The number of spectra identified as useful in the first step and its percentage as compared to the total number of useful spectra on the plate (= Col(5)/Col(3) * 100)
Column (7) & (8):	The number of spectra identified as useful in the second step and its percentage as compared to the total number of useful spectra on the plate (= Col(7)/Col(3) * 100)
Column (9) & (10):	The number of stellar spectra identified as unusable and its percentage as compared to the total number of extracted spectra on the plate (= Col(9)/Col(2) * 100)
Column (11), (12),: & (13)	Classifications of unusable spectra – saturated, odd, and noise, respectively

As can be seen in the last row of Column (2), a total of 294,039 stellar spectra were extracted from the 87 HK survey plates. Among those, three-quarters turned out to be useful (columns (4) and (10) on the last line). Most of the useful spectra (96%) were determined automatically in the first step; the remaining useful spectra (4%) were identified by human intervention (columns (6) and (8) at the bottom). This means that most of the useful spectra can be obtained effectively and rapidly without the second step, which demands careful attention and required a great deal of time.

Table 2.1 Data Reduction Statistics for 87 HK Plates

(1)	(2)	**(3)**	**(4)**	(5)	(6)	(7)	(8)	**(9)**	**(10)**	(11)	(12)	(13)
BS 17579	3911	**1138**	**29.1%**	1017	89.4%	121	10.6%	**2774**	**70.9%**	10	194	2570
CS 22881	4881	**3717**	**76.2%**	3506	94.3%	211	5.7%	**1164**	**23.8%**	250	208	706
CS 22882	2828	**2085**	**73.7%**	2024	97.1%	61	2.9%	**743**	**26.3%**	169	95	479
CS 22886	4342	**3392**	**78.1%**	3252	95.9%	140	4.1%	**950**	**21.9%**	229	165	556
CS 22887	4012	**3126**	**77.9%**	2970	95.0%	156	5.0%	**886**	**22.1%**	233	130	523
CS 22888	3481	**2597**	**74.6%**	2452	94.4%	145	5.6%	**884**	**25.4%**	210	138	536
CS 22892	4621	**3483**	**75.4%**	3346	96.1%	137	3.9%	**1138**	**24.6%**	220	358	560
CS 22893	3564	**2556**	**71.7%**	2451	95.9%	105	4.1%	**1008**	**28.3%**	260	140	608
CS 22894	3651	**2689**	**73.7%**	2551	94.9%	138	5.1%	**962**	**26.3%**	198	187	577
CS 22960	4137	**3009**	**72.7%**	2868	95.3%	141	4.7%	**1128**	**27.3%**	311	172	645
CS 22961	3357	**2325**	**69.3%**	2199	94.6%	126	5.4%	**1032**	**30.7%**	296	178	558
CS 22962	3071	**2330**	**75.9%**	2226	95.5%	104	4.5%	**741**	**24.1%**	159	188	394
CS 22966	3223	**2280**	**70.7%**	2204	96.7%	76	3.3%	**943**	**29.3%**	268	233	442
CS 22967	3189	**2333**	**73.2%**	2235	95.8%	98	4.2%	**856**	**26.8%**	170	194	492
CS 22968	4391	**3054**	**69.6%**	2974	97.4%	80	2.6%	**1337**	**30.4%**	296	336	705
CS 29526	3383	**2530**	**74.8%**	2463	97.4%	67	2.6%	**853**	**25.2%**	260	88	505
CS 29527	2735	**2076**	**75.9%**	2019	97.3%	57	2.7%	**659**	**24.1%**	142	124	393
CS 29528	3022	**2206**	**73.0%**	2124	96.3%	82	3.7%	**816**	**27.0%**	180	135	501
CS 30304	3275	**2342**	**71.5%**	2283	97.5%	59	2.5%	**933**	**28.5%**	212	126	595
CS 30310	3025	**2160**	**71.4%**	2113	97.8%	47	2.2%	**865**	**28.6%**	223	108	534
CS 30315	3375	**2522**	**74.7%**	2472	98.0%	50	2.0%	**853**	**25.3%**	212	148	493
CS 30316	3079	**2255**	**73.2%**	2191	97.2%	64	2.8%	**824**	**26.8%**	196	136	492
CS 30323	3583	**2677**	**74.7%**	2624	98.0%	53	2.0%	**906**	**25.3%**	223	153	530
CS 30324	3054	**2162**	**70.8%**	2083	96.3%	79	3.7%	**892**	**29.2%**	112	78	702
CS 30327	4472	**3288**	**73.5%**	3119	94.9%	169	5.1%	**1184**	**26.5%**	142	136	906
CS 30337	4270	**3108**	**72.8%**	3037	97.7%	71	2.3%	**1162**	**27.2%**	247	247	668
CS 30339	2984	**2139**	**71.7%**	2082	97.3%	57	2.7%	**845**	**28.3%**	168	144	533
CS 30344	3728	**2660**	**71.4%**	2593	97.5%	67	2.5%	**1068**	**28.6%**	252	223	593
CS 30493	3461	**2715**	**78.4%**	2631	96.9%	84	3.1%	**746**	**21.6%**	155	134	457
CS 31060	3057	**2073**	**67.8%**	1949	94.0%	124	6.0%	**984**	**32.2%**	85	82	817
CS 31062	2943	**2297**	**78.0%**	2140	93.2%	157	6.8%	**646**	**22.0%**	45	150	451
CS 31065	3061	**2354**	**76.9%**	2209	93.8%	145	6.2%	**707**	**23.1%**	40	127	540
CS 31066	2766	**2138**	**77.3%**	2004	93.7%	134	6.3%	**628**	**22.7%**	56	90	482
CS 31069	5351	**3658**	**68.4%**	3207	87.7%	451	12.3%	**1693**	**31.6%**	55	694	944
CS 31070	5354	**3650**	**68.3%**	3141	86.1%	509	13.9%	**1695**	**31.7%**	51	668	976
CS 31077	3025	**2242**	**74.1%**	2129	95.0%	113	5.0%	**783**	**25.9%**	64	115	604
CS 31082	2801	**2150**	**76.8%**	2059	95.8%	91	4.2%	**651**	**23.2%**	57	123	471
CS 31086	2750	**2138**	**77.7%**	2002	93.6%	136	6.4%	**612**	**22.3%**	99	85	428
CS 31088	5050	**3384**	**67.0%**	3077	90.9%	307	9.1%	**1666**	**33.0%**	71	925	670
CS 31089	2845	**2164**	**76.1%**	2059	95.1%	105	4.9%	**681**	**23.9%**	68	150	463
CS 31090	2850	**2108**	**74.0%**	1975	93.7%	133	6.3%	**742**	**26.0%**	51	148	543
CS 22166	2859	**2299**	**80.4%**	2225	96.8%	74	3.2%	**560**	**19.6%**	152	183	225
CS 22170	2923	**2365**	**80.9%**	2269	95.9%	96	4.1%	**558**	**19.1%**	162	198	198
CS 22171	2611	**2242**	**85.9%**	2117	94.4%	125	5.6%	**369**	**14.1%**	180	128	61
CS 22172	3416	**2901**	**84.9%**	2803	96.6%	98	3.4%	**515**	**15.1%**	193	238	84

Table 2.1 (continued)

(1)	(2)	**(3)**	**(4)**	(5)	(6)	(7)	(8)	**(9)**	**(10)**	(11)	(12)	(13)
CS 22174	2653	**2286**	**86.2%**	2216	96.9%	70	3.1%	**367**	**13.8%**	150	129	88
CS 22175	2889	**2459**	**85.1%**	2400	97.6%	59	2.4%	**430**	**14.9%**	152	180	98
CS 22179	2925	**2483**	**84.9%**	2385	96.1%	98	3.9%	**442**	**15.1%**	156	158	128
CS 22180	2680	**2338**	**87.2%**	2225	95.2%	113	4.8%	**342**	**12.8%**	143	109	90
CS 22181	3015	**2567**	**85.1%**	2471	96.3%	96	3.7%	**448**	**14.9%**	131	189	128
CS 22183	2758	**2354**	**85.4%**	2226	94.6%	128	5.4%	**404**	**14.6%**	100	169	135
CS 22184	2978	**2562**	**86.0%**	2466	96.3%	96	3.7%	**416**	**14.0%**	160	172	84
CS 22185	2963	**2527**	**85.3%**	2455	97.2%	72	2.8%	**436**	**14.7%**	185	172	79
CS 22188	2815	**2120**	**75.3%**	1865	88.0%	255	12.0%	**695**	**24.7%**	62	232	401
CS 22189	2951	**2537**	**86.0%**	2421	95.4%	116	4.6%	**414**	**14.0%**	156	154	104
CS 22875	3703	**2950**	**79.7%**	2872	97.4%	78	2.6%	**753**	**20.3%**	281	294	178
CS 22941	3147	**2558**	**81.3%**	2500	97.7%	58	2.3%	**589**	**18.7%**	216	254	119
CS 22942	2484	**2081**	**83.8%**	1995	95.9%	86	4.1%	**403**	**16.2%**	194	110	99
CS 22945	4727	**3871**	**81.9%**	3786	97.8%	85	2.2%	**856**	**18.1%**	368	372	116
CS 22946	2502	**2101**	**84.0%**	2033	96.8%	68	3.2%	**401**	**16.0%**	195	120	86
CS 22949	3238	**2760**	**85.2%**	2700	97.8%	60	2.2%	**478**	**14.8%**	201	200	77
CS 22951	4989	**3985**	**79.9%**	3873	97.2%	112	2.8%	**1004**	**20.1%**	484	383	137
CS 22952	2959	**2480**	**83.8%**	2384	96.1%	96	3.9%	**479**	**16.2%**	264	159	56
CS 22953	3878	**3054**	**78.8%**	2955	96.8%	99	3.2%	**824**	**21.2%**	410	333	81
CS 22954	2985	**2425**	**81.2%**	2330	96.1%	95	3.9%	**560**	**18.8%**	316	166	78
CS 22957	2901	**2468**	**85.1%**	2384	96.6%	84	3.4%	**433**	**14.9%**	173	175	85
CS 22958	3184	**2670**	**83.9%**	2619	98.1%	51	1.9%	**514**	**16.1%**	208	207	99
CS 22963	3263	**2709**	**83.0%**	2626	96.9%	83	3.1%	**554**	**17.0%**	248	200	106
CS 29491	3607	**2281**	**63.2%**	2228	97.7%	53	2.3%	**1326**	**36.8%**	112	152	1062
CS 29493	5036	**3982**	**79.1%**	3870	97.2%	112	2.8%	**1054**	**20.9%**	171	213	670
CS 29494	3128	**2350**	**75.1%**	2311	98.3%	39	1.7%	**778**	**24.9%**	160	119	499
CS 29496	3091	**2256**	**73.0%**	2226	98.7%	30	1.3%	**835**	**27.0%**	131	98	606
CS 29497	2752	**1979**	**71.9%**	1940	98.0%	39	2.0%	**773**	**28.1%**	161	73	539
CS 29499	3390	**2525**	**74.5%**	2486	98.5%	39	1.5%	**865**	**25.5%**	151	139	575
CS 29500	2869	**2066**	**72.0%**	2030	98.3%	36	1.7%	**803**	**28.0%**	204	102	497
CS 29503	2940	**2092**	**71.2%**	2051	98.0%	41	2.0%	**848**	**28.8%**	247	146	455
CS 29504	2861	**2064**	**72.1%**	2001	96.9%	63	3.1%	**797**	**27.9%**	216	132	449
CS 29505	4610	**3384**	**73.4%**	3276	96.8%	108	3.2%	**1227**	**26.6%**	288	214	725
CS 29509	2676	**1990**	**74.4%**	1931	97.0%	59	3.0%	**686**	**25.6%**	173	107	406
CS 29510	3169	**2224**	**70.2%**	2183	98.2%	41	1.8%	**945**	**29.8%**	204	217	524
CS 29512	4378	**3399**	**77.6%**	3287	96.7%	112	3.3%	**979**	**22.4%**	179	208	592
CS 29513	3572	**2454**	**68.7%**	2410	98.2%	44	1.8%	**1118**	**31.3%**	256	228	634
CS 29514	3025	**2276**	**75.2%**	2226	97.8%	50	2.2%	**749**	**24.8%**	209	151	389
CS 29515	2991	**2075**	**69.4%**	2039	98.3%	36	1.7%	**916**	**30.6%**	285	195	436
CS 29517	3037	**2274**	**74.9%**	2227	97.9%	47	2.1%	**763**	**25.1%**	153	176	434
CS 29518	2901	**2078**	**71.6%**	2025	97.4%	53	2.6%	**823**	**28.4%**	211	185	427
CS 29519	3661	**2459**	**67.2%**	2404	97.8%	55	2.2%	**1202**	**32.8%**	303	224	675
Total	**294039**	**221670**	**75.4%**	**212812**	96.0%	8858	4.0%	**72371**	**24.6%**	**16199**	**16716**	**39456**

Chapter 3

ANNs FOR KNOWN METAL-POOR STARS

3.1 Overview

We make use of 4688 metal-poor stars with previously obtained estimates of metallicity and measured (or estimated) broadband color, originally selected from the visual HK survey (HK1), to train a set of Artificial Neural Networks. The networks are then used to (1) estimate metallicity, [Fe/H], and to (2) classify stars by their colors and metal abundance from two input variables – the observed color, $(B-V)_0$, and the measured K18 index (the equivalent width of Ca II K line over a band of 18 Å). The trained networks for prediction and classification will be referred to as mp-p.net and mp-c.net respectively, and are used in the process of metallicity estimation and classification for the digitized HK2 stellar spectra.

3.2 Prediction of [Fe/H]

3.2.1 Data Set

The data set consists of the K18 index, $(B-V)_0$ color, and metal abundance, [Fe/H], for 4688 known metal-poor stars (HK1). The K18 index is measured from the medium-resolution spectra obtained during the course of the observational follow-up of the HK survey. The $(B-V)_0$ color is obtained either from direct photometric measurements obtained during the course of the HK survey follow-up, or is an approximate value estimated from the of the Balmer lines in the follow-up spectra – in particular Hδ (see Beers et al. 1999). The metallicity, [Fe/H], is determined from the abundance estimation techniques explained in detail in Chapter 2. These three parameters are believed to be quite accurate (Δ K18 ~ 0.2 A, Δ $(B-V)_0$ ~ 0.03 – 0.08 magnitudes, Δ [Fe/H] ~0.2 dex).

First, the 4688 metal-poor stars are evenly divided into two groups according to their input parameters of [Fe/H], $(B-V)_0$, and K18. The metallicity distribution functions of the two groups are nearly identical, as are their distributions in $(B-V)_0$ color and K18 index. Each group contains data across the entire range of those parameters. A proper separation of these subsets is particularly important because the networks need to learn a general relation between inputs and outputs – preparation of a well-distributed training set ensures the success of the training process. The first set of 2344 metal-poor stars is used in the training process, and the other set of 2344 metal-deficient stars is used to objectively validate the trained network. These data sets are referred to as "seen" data and "unseen" data respectively, since the former participates in the training process while the latter is never involved in training process, and hence can be used to make an objective validation of the procedure.

Table 3.1 Data Set for Prediction

Training Set (Seen Data)	Validation Set (Unseen Data)
2344	2344

3.2.2 Artificial Neural Network

An Artificial Neural Network (ANN) is a computational tool that can learn and generate general relations between available input variables and some desired output variables. ANNs are composed of three main components - an input layer where input parameters are entered into the network, hidden layers that are made up of "neurons," and an output layer where generated output parameters emerge.

The neurons in the hidden layers are connected to all of the input nodes and output nodes (or neurons in next layer). Initially, the ANN assigns random connection weights between the neurons, and hence produces a random set of output values. Errors between the outputs and the inputs are then propagated backward through the network, and the ANN is allowed to change the weights assigned to the neurons in order to produce predictions that are closer to the goal. This training process is continued until the network obtains optimized connection weights that map the inputs to the outputs. The trained networks then can be used to produce new outputs for other input data. A more detailed discussion of the principles of ANNs can be found in the Appendix.

In this thesis, feed-forward and back-propagation ANNs have been employed. In the process of training, a supervised learning mode was used – providing the networks with both correct answers (desired outputs) and their corresponding inputs. The ANN architectures were constructed with a single hidden layer and a few neurons within it (from 2 to 50 nodes). Theoretically there is no limitation to the number of hidden layers, but it is generally accepted that the use of a single hidden layer is often appropriate (Masters 1993).

One of problems that should needs to be avoided in the application of ANNs is referred to as over-fitting. This can occur when too many neurons are used, so that the trained networks only "remember" the outputs with respect to specific inputs, rather than learn general relations between them. Use of a single hidden layer is prevents the generation of too many connection weights among neurons. Practically, it is also known that little significant improvement is obtained with the use of multiple hidden layers in almost all cases (Masters 1993; Zeanah 2000).

For the analysis of metal-poor stars with ANNs, I have employed a commercial neural network software product called "BackPack," by Z Solutions, LLC (2000). This program is particularly useful since one can easily manipulate the network parameters (e.g., learning rate, momentum, and weights), and the package automatically determines the point at which training needs to be stopped. BackPack promptly generates results with graphics and statistical quantities. One can construct a single hidden layer with up to 50 hidden nodes, and also apply it to problems with up to 24 classification levels.

3.2.3 Training and Prediction Results

The $(B-V)_0$ color and K18 index of the training set are used as input variables in training a few networks to predict one output variable – the metallicity, [Fe/H]. Because the known [Fe/H] are provided for the networks, training was in supervised mode. Various numbers of neurons in a single hidden layer were tested to determine an optimized ANN structure. Then these trained networks were applied to both the seen data set (itself) and to the unseen data set, and predicted metallicities were compared with real (known) metallicities.

The results of these approaches are summarized in Table 3.2. The first column displays the ANN architectures in the form of i:j:k, where i is the number of inputs, j is the number of neurons in a single hidden layer, and k is the number of outputs. Note that i and k are always 2 and 1 in this case. The second and third columns show the linear correlation coefficient (c.c.) and biweight estimator of scale (S_{BI}) between the predicted and true metallicities in seen data set. The biweight scale estimator is a robust and resistant estimator of the rms residual which remains stable in the presence of outliers (Beers et al. 1990). If a data set is drawn from a Gaussian parent population, the biweight estimator approaches the more conventional standard deviation. Even when the data set is non-Gaussian, the robustness of the biweight scale estimator ensures that the scale estimate remains valid. The fourth and fifth columns are the same quantities for the unseen data set, which enable us to objectively evaluate the performance of the trained network. All trained networks were able to predict metallicity [Fe/H] successfully with correlation coefficients greater than c.c. = 0.94. For the validation set, the correlation coefficient has a tendency to increase until the case of 2:10:1 and then decrease as the number of neurons increases. This particular architecture exhibits the lowest value of the biweight estimator, S_{BI}. Also, the trained networks are properly learning general relations between the inputs and outputs since no apparent differences between correlation coefficients for seen and unseen samples are found.

Table 3.2 Prediction Results

Architecture	Training Set		Validation Set	
	c. c.	S_{BI}	c. c.	S_{BI}
2 : 2 : 1	0.95	0.23	0.9440	0.2295
2 : 4 : 1	0.98	0.12	0.9734	0.1257
2 : 6 : 1	0.98	0.12	0.9733	0.1252
2 : 8 : 1	0.98	0.13	0.9733	0.1267
2 : 10 : 1	**0.98**	**0.12**	**0.9735**	**0.1249**
2 : 12 : 1	0.98	0.14	0.9695	0.1413
2 : 14 : 1	0.98	0.13	0.9720	0.1325
2 : 16 : 1	0.98	0.15	0.9688	0.1454
2 : 18 : 1	0.98	0.14	0.9691	0.1421
2 : 20 : 1	0.98	0.14	0.9701	0.1420
2 : 30 : 1	0.95	0.24	0.9404	0.2424
2 : 40 : 1	0.95	0.24	0.9405	0.2418
2 : 50 : 1	0.95	0.25	0.9405	0.2444

The trained network 2:10:1, which shows the best results, was picked to be used in the metal abundance estimation for the stellar spectra in HK2. This network will be referred as to “mp-p.net” in this thesis. Figure 3.1 shows a plot of the predicted [Fe/H] compared to the real [Fe/H], derived by applying mp-p.net to the validation set. Most of data points are well distributed near the one-to-one line. A few of the stars appear to deviate from this relation, especially near [Fe/H] = 0. These outliers should not be a problem since we are interested in the identification of new extremely low abundance stars with [Fe/H] < -2.0. Not that the predicted [Fe/H] has a tendency to saturate near [Fe/H] = –3.5. This phenomenon, which is not a surprise, is a characteristic of the transfer function used in artificial neurons: the non-linear sigmoid function saturates to a constant when the summation of weighted inputs attains a certain value. Many papers making use of ANNs have reported a similar phenomenon.

In order to see how well the mp-p.net predicts metallicity, a grid of artificial $(B\text{-}V)_0$ colors and K18 indices were prepared and fed into the trained net. The contours of [Fe/H] derived from the mp-p.net are drawn over the space of $(B\text{-}V)_0$ and K18 in Figure 3.2. It is worthwhile to compare this plot with Figure 2.1, obtained by application to the inputs obtained from real stars. The results are quite encouraging. For the metal-poor stars with [Fe/H] > –3.0, mp-p.net is able to estimate metallicity correctly over the entire range of stellar temperatures. For the extremely metal-deficient stars with [Fe/H] < –3.0, the network does a good job for hotter stars but seems to overestimate metallicity for cooler stars. This is an unavoidable consequence of the lack of cooler metal-poor stars in the training set (see Figure 2.1). Therefore, when we analyze candidate cooler metal-deficient stars derived by the net, we anticipate the need to reduce the metallicity estimates for those stars. Now we have a powerful network (mp-p.net) in the prediction of metallicity. If we are able to estimate $(B\text{-}V)_0$ and K18 from the low-resolution prism spectra (HK2) with

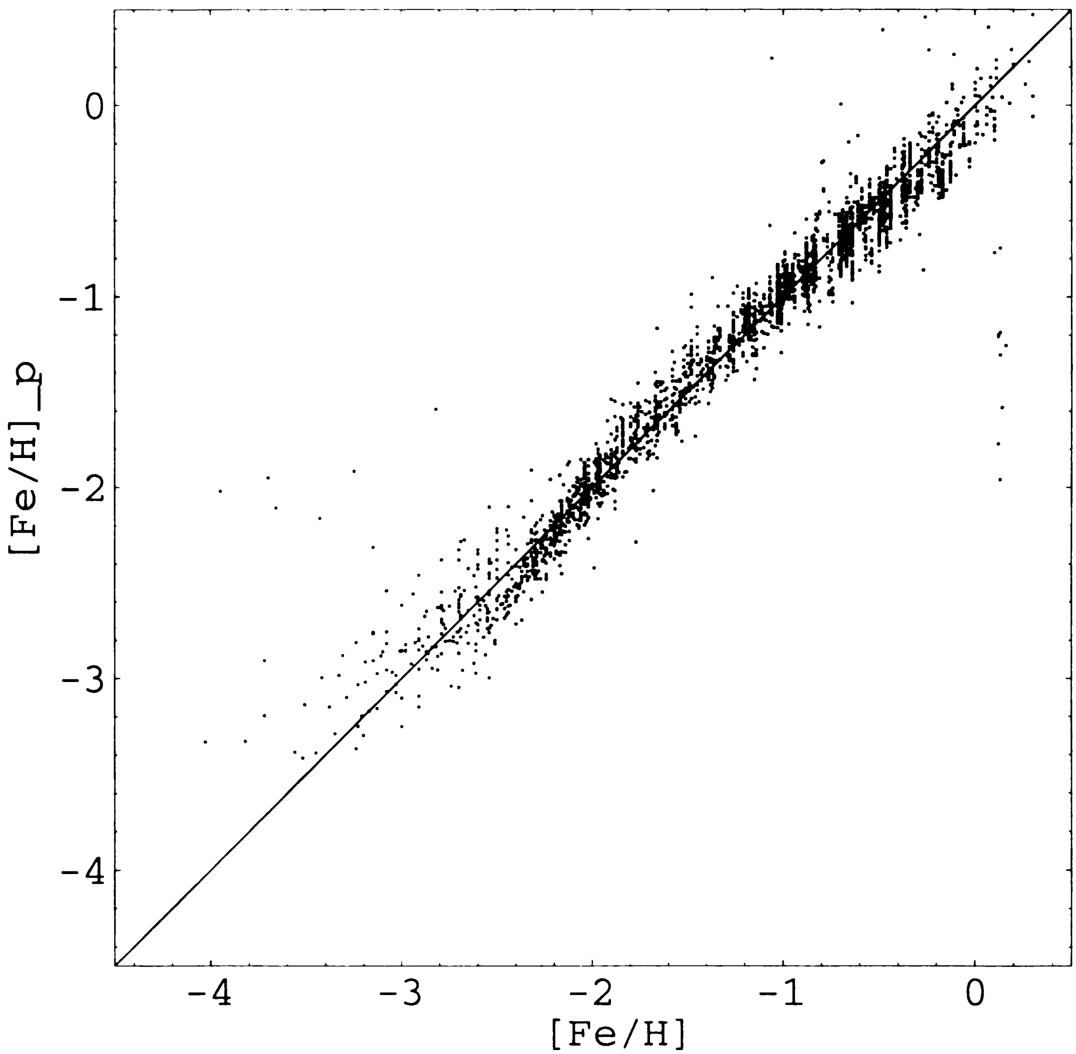

Figure 3.1 Predicted [Fe/H] compared to known [Fe/H] for metal-poor stars in the validation set (unseen data). The metal abundance is estimated from known colors and known K18 indices.

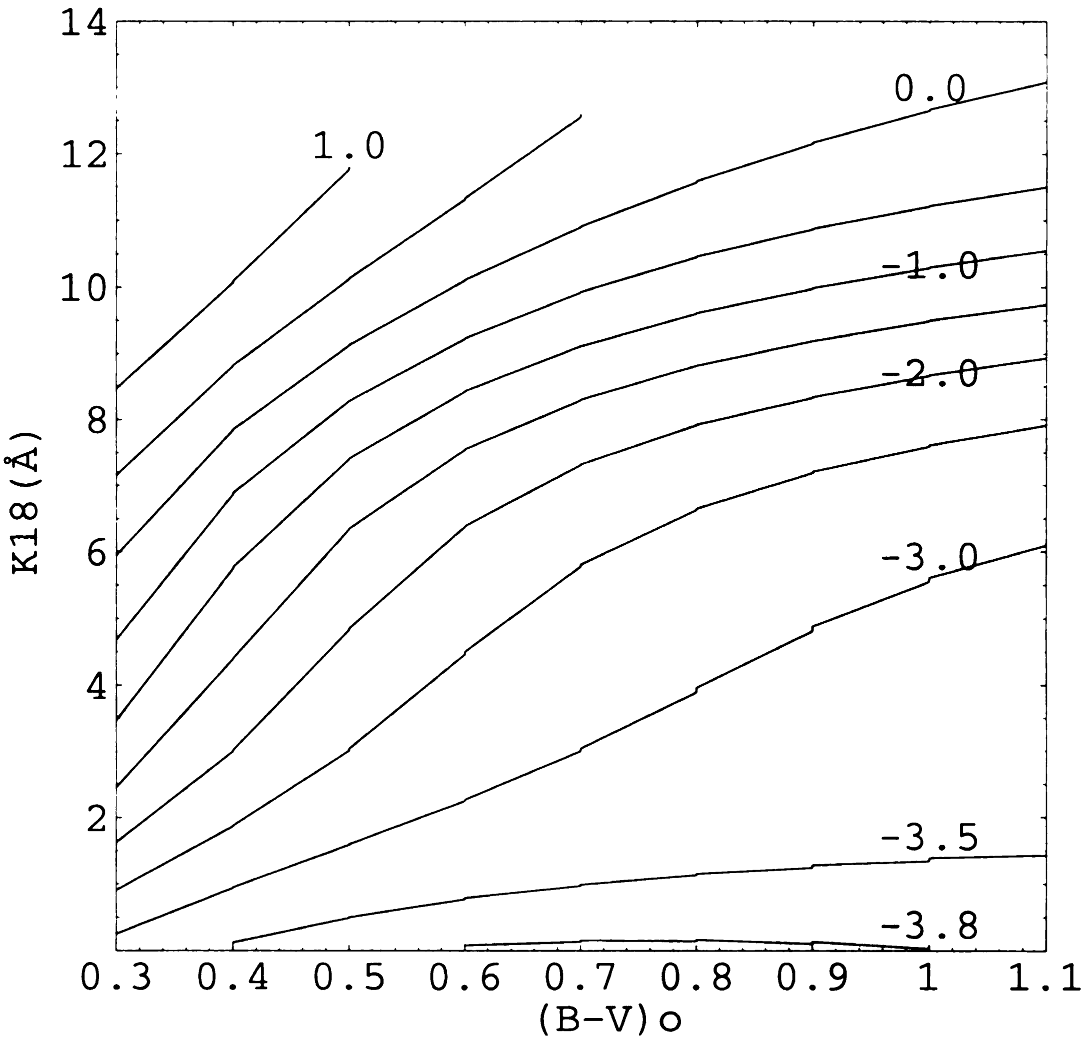

Figure 3.2 Iso-metallicity contours of [Fe/H], as derived from the trained network over the space of $(B\text{-}V)_0$ and K18.

accuracy approaching that of the measured values, [Fe/H] can be obtained rapidly with high accuracy.

3.3 Classification

3.3.1 Data Set

The data sets for the classification process are the same ones used in the prediction process. Here, the metal-poor stars were divided into 6 groups according to their colors and metallicities. The groups will be referred to as "MP-class." A summary of MP-class with classification category and the number of data is shown in Table 3.3. The ultimate goal of this project is to identify extremely metal-poor star candidates, which are expected to be classified in MP-class 1 and 2. Because the metal-poor stars were evenly divided into training and validation sets according to their input parameters, they contain a similar number of stars in each MP-class.

Table 3.3 Data Set for Classification

MP-class	$(B-V)_0$	[Fe/H]	Total	Training Set	Validation Set
1	0.30 – 0.50	-4.00 to -2.00	684	340	344
2	0.51 – 1.27	-4.00 to -2.00	370	187	183
3	0.30 – 0.50	-1.99 to -1.00	782	390	392
4	0.51 – 1.50	-1.99 to -1.00	684	343	341
5	0.30 – 0.50	-0.99 to 0.30	1016	509	507
6	0.51 – 1.45	-0.99 to 0.30	1152	575	577
Total			4688	2344	2344

3.3.2 ANN Architecture

Unlike the prediction process, probability mode was employed in the classification approach. This means that the number of neurons in the output layer is the same as the number of classification groups. In our case, there are 6 output neurons in the output layer. A trained network generates the "probability" for each output node, instead of estimating a physical parameter. Each object is classified into the group where the maximum probability occurs.

3.3.3 Training and Classification Results

The $(B-V)_0$ color and K18 index in the training set were used as input variables and the output vector for MP-class was provided as an output variable. For example, MP-class 1 has a vector of (1,0,0,0,0,0). Once again, various numbers of neurons in a single hidden layer were tested to determine an optimized ANN structure. Then the trained networks were applied to both seen data set (itself) and unseen data set to classify stars by their color and metallicity.

The classification results are summarized in Table 3.4. The first column displays the ANN architectures. Correction rates for all stars in the sample are seen on the third column. The correction rate is a ratio of the number of correctly assigned (by networks) stars to the number of all real stars in the group. The rest of the columns show correction rates for each MP-class. As the number of neurons in hidden layer increases, the overall correction rate increases gradually and then asymptotically approaches about 90%. The more metal-rich stars in MP-class 5 and 6 are classified well, with a correction rate generally over 90%, while the stars in other groups show some fluctuations. This is because the number of more metal-rich stars are larger than the other subsamples. The trained networks appear to be learning general relations between input parameters and output parameters, as there are no distinctive differences between correction rates for the training and validation sets.

The trained network 2:12:6 was picked to be used in the process of classification for the stellar spectra in HK2. This network will be referred as to "mp-c.net" in this thesis. Although the network with architecture 2:16:6 shows the best overall correction rate for the unseen set, the network 2:12:6 was selected since it showed consistent correction rates of over 83% for all MP-classes.

Table 3.4 Classification Result (Correction Rate)

Architecture	Set	Overall	MP-class 1	MP-class 2	MP-class 3	MP-class 4	MP-class 5	MP-class 6
2 : 2 : 6	Training	81.10 %	98.8 %	99.5 %	54.6 %	30.0 %	98.2 %	97.9 %
	Validate	80.76 %	98.0 %	98.9 %	55.6 %	27.3 %	98.2 %	98.1 %
2 : 4 : 6	Training	85.88 %	85.3 %	68.4 %	90.8 %	88.9 %	82.9 %	89.4 %
	Validate	86.43 %	84.6 %	70.5 %	92.1 %	88.0 %	83.4 %	90.5 %
2 : 6 : 6	Training	88.10 %	77.4 %	78.6 %	89.5 %	72.9 %	97.4 %	97.4 %
	Validate	87.12 %	75.9 %	76.5 %	89.5 %	70.4 %	96.6 %	97.1 %
2 : 8 : 6	Training	90.19 %	96.8 %	81.8 %	77.9 %	78.7 %	97.6 %	97.6 %
	Validate	89.80 %	95.9 %	84.7 %	77.0 %	78.0 %	96.8 %	97.2 %
2 : 10 : 6	Training	88.61 %	77.1 %	85.6 %	90.3 %	78.1 %	98.6 %	92.7 %
	Validate	88.31 %	75.6 %	86.3 %	89.8 %	78.6 %	98.0 %	92.7 %
2 : 12 : 6	Training	91.81 %	85.3 %	94.7 %	91.5 %	85.7 %	97.2 %	93.7 %
	Validate	**91.04 %**	**83.7 %**	**93.4 %**	**90.1 %**	**85.3 %**	**96.8 %**	**93.6 %**
2 : 14 : 6	Training	89.21 %	90.0 %	82.4 %	75.6 %	83.1 %	97.6 %	96.3 %
	Validate	88.23 %	89.5 %	81.4 %	73.7 %	81.8 %	96.6 %	95.8 %
2 : 16 : 6	Training	91.30 %	93.5 %	77.0 %	87.4 %	91.3 %	95.9 %	93.2 %
	Validate	91.30 %	92.7 %	79.8 %	87.8 %	90.9 %	95.1 %	93.4 %
2 : 18 : 6	Training	90.61 %	80.0 %	84.5 %	92.1 %	85.1 %	95.5 %	96.9 %
	Validate	90.15 %	79.4 %	86.9 %	90.6 %	84.5 %	94.9 %	96.5 %
2 : 20 : 6	Training	89.59 %	85.6 %	78.1 %	82.6 %	84.3 %	96.9 %	97.2 %
	Validate	89.38 %	84.6 %	81.4 %	83.2 %	81.5 %	96.3 %	97.6 %
2 : 30 : 6	Training	90.53 %	97.1 %	85.0 %	78.7 %	87.5 %	93.1 %	96.0 %
	Validate	90.36 %	97.4 %	88.5 %	77.8 %	85.9 %	92.7 %	95.8 %
2 : 40 : 6	Training	91.72 %	86.5 %	90.9 %	91.3 %	81.6 %	97.4 %	96.3 %
	Validate	91.13 %	86.0 %	91.8 %	90.1 %	80.1 %	96.4 %	96.5 %
2 : 50 : 6	Training	91.04 %	89.7 %	81.3 %	90.5 %	86.9 %	91.9 %	97.0 %
	Validate	90.49 %	89.5 %	83.1 %	90.1 %	85.0 %	90.7 %	96.7 %

Chapter 4

K18 INDEX CALIBRATION

4.1 Overview

With 3269 known metal-poor stars selected from the visual HK survey (HK1), and their corresponding low-resolution digital spectra (HK2), the Artificial Neural Networks are trained in order to estimate the K18 index (as originally measured from medium-resolution follow-up spectra of the visually-selected HK survey stars) directly from the low-resolution spectra extracted from the APM scans (HK2). The "predicted" K18 index (hereafter, referred as to K18_p) is used to obtain a new index, the "fit" K18 index (hereafter, called K18_f) that is the best estimated value derived directly from the HK2 spectra. The index K18_f and the observed $(B-V)_0$ colors are used as input variables into mp-p.net and mp-c.net (the trained networks discussed in Chapter 3) to estimate [Fe/H] and determine MP-class for these stars. The efficiency and recovery of these results are discussed.

4.2 K18 Index Calibration

4.2.1 Data Set

By matching up the positional coordinates between 4688 known metal-poor stars (HK1) and stellar spectra from 293 digitally scanned plates (HK2), 3787 metal-poor stars were matched with HK2 spectra (a match requiring an angular separation between the two positions of less than 20 seconds of arc). Among these matches, 518 spectra turned out to be unusable for the following reasons: saturated (15), noise (347), odd (65), bad quality of spectra (32), and multiple matches (59). The remaining 3269 metal-poor stars with known quantities ([Fe/H], $(B-V)_0$, and K18) and corresponding low-resolution spectra are the data set discussed in this chapter.

4.2.2 Measured K18 Index (K18_2)

In Section 2.3, the general algorithms for spectral data reduction and equivalent width measurement were explained fully. Recall that the measured equivalent width over 13 pixels (= 18 Å) around the Ca II K line in the HK2 spectra is called K18_2 in this thesis.

Figure 4.1 presents the relationship between the K18 indices (HK1) and K18_2 indices (HK2) for the 3269 metal-poor stars. K18 is believed to be very accurate since it was measured with the full analysis of medium-resolution stellar spectra. Overall, the two data sets show a linear relationship, but the distribution of K18 is too broad at a given K18_2 (especially near K18_2 = 5 Å) and the spread of K18_2 (in the horizontal direction) increases as K18 approaches 10 Å, where a saturation of K18 occurs. These uncertainties could cause the ANNs to suffer somewhat in the estimation of [Fe/H] and the determination of MP-class. For example, at K18_2 ~ 5 Å, K18 ranges between 1 and 10 Å. As seen in Figure 3.2, if the mp-p.net feeds on the incorrect K18_2 for stars of $(B-V)_0 = 0.5$ (for example), the trained network would predict a metallicity [Fe/H] of about –2.5 although its real value could be anywhere between –3.0 and 0.0 (since the true K18 is between 1 and 10 Å). Because the metallicity is a function of only the two variables of color and K18 index, and they both affect [Fe/H] significantly, the estimation of [Fe/H] can be sensitively distorted by even minor incorrect information in these quantities. Thus it is of crucial importance that K18_2 should be an accurate estimate of K18. Although a number of efforts for improvement of the continuum estimate and measurement of the K18_2

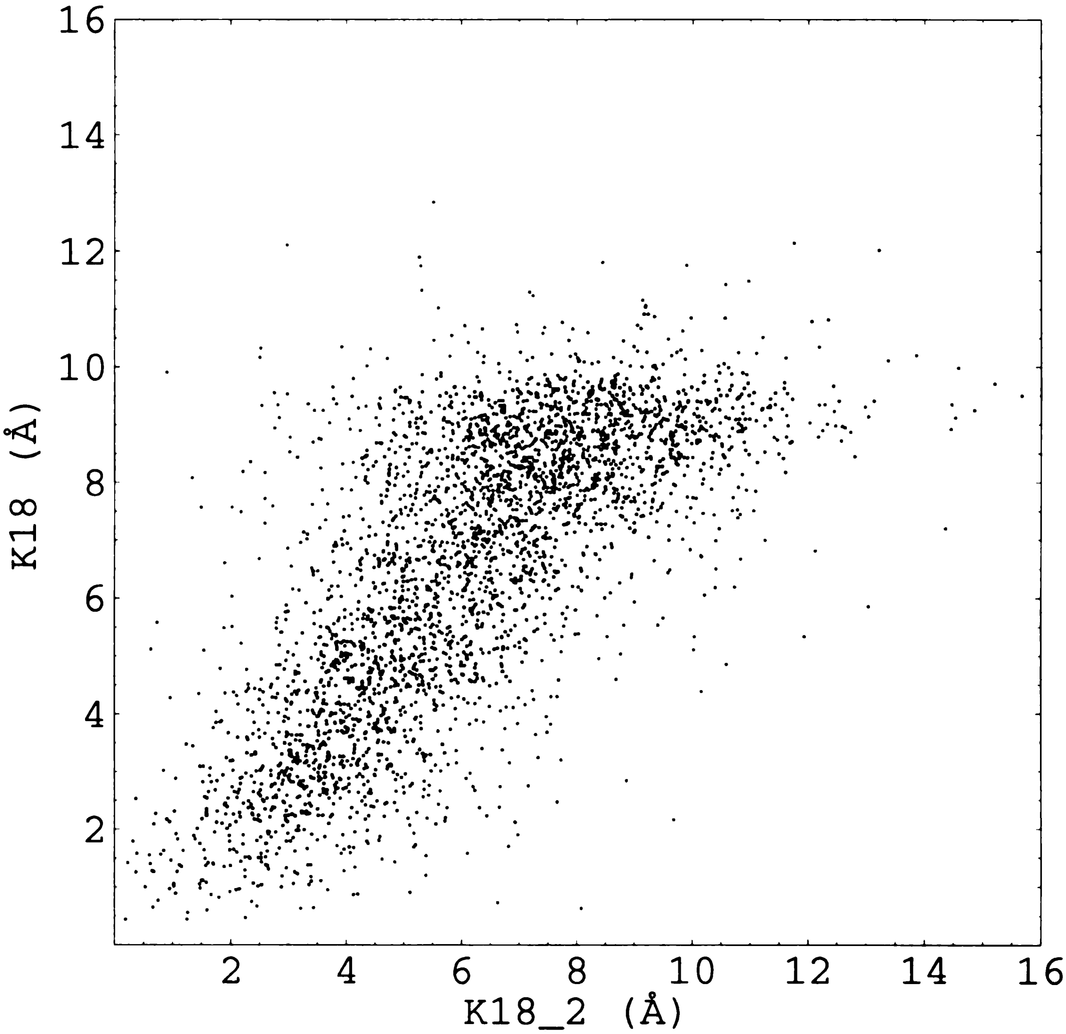

Figure 4.1 Relationship between K18 (HK1) and K18_2 (HK2). K18 is derived from medium-resolution spectra from the HK survey follow-up, while K18_2 is calculated from low-resolution APM spectra.

index have been made, the algorithms described earlier do generate the most reasonable and acceptable equivalent widths, shown in Figure 4.1. Nevertheless, the measured K18_2 does not satisfy the criteria to be used with the networks trained with K18 unfortunately – it must be adjusted.

Our task is then clear – can we develop a "new" methodology for estimating the K18_2 index directly from low-resolution spectra (HK2), ensuring a acceptable quality as good as the K18 index (HK1) ? In order to accomplish this task, we first must explore an analysis of the digital spectra themselves. Figure 4.2 shows again the distributions of K18 and K18_2 of stars for the validation sets only (Table 4.1), but separated according to the maximum counts in their spectral continua (dashed line in Figure 2.4 (a); hereafter, referred to as "flux_m"). The data points in Figure 4.2 (a), (b), and (c) belong to flux_m of 126,000 - 925,000 counts, 69,000 – 126,000 counts, and 14,000 – 69,000 counts, respectively. Each group has a similar number of objects – 614 stars, 559 stars, and 596 stars. This even distribution ensures enables a useful statistical comparison between the flux groups. Four features should be noted – as flux_m decreases from panel (a) to (c), (1) the distribution of data moves from lower K18 to higher K18 (the same applies to K18_2), (2) the average of the color $<(B-V)_0>$ increases (0.44, 0.52, and 0.60 respectively), (3) the horizontal distribution of K18_2 at a given K18 tends to be broader, and (4) the slope of the distribution tends to be decreased. The first two characteristics can be easily explained from an understanding of the stellar spectral types. As the spectral class changes from F-type to G-type (note that $(B-V)_0$ is ~0.35 for F0 type and 0.60 for G0 type), the overall fluxes near Ca II H and K line become weaker, due to the increasing strength of the metallic absorption lines relative to the stellar continuum. Meanwhile, the strength of Ca II K lines become stronger, since the energy levels in

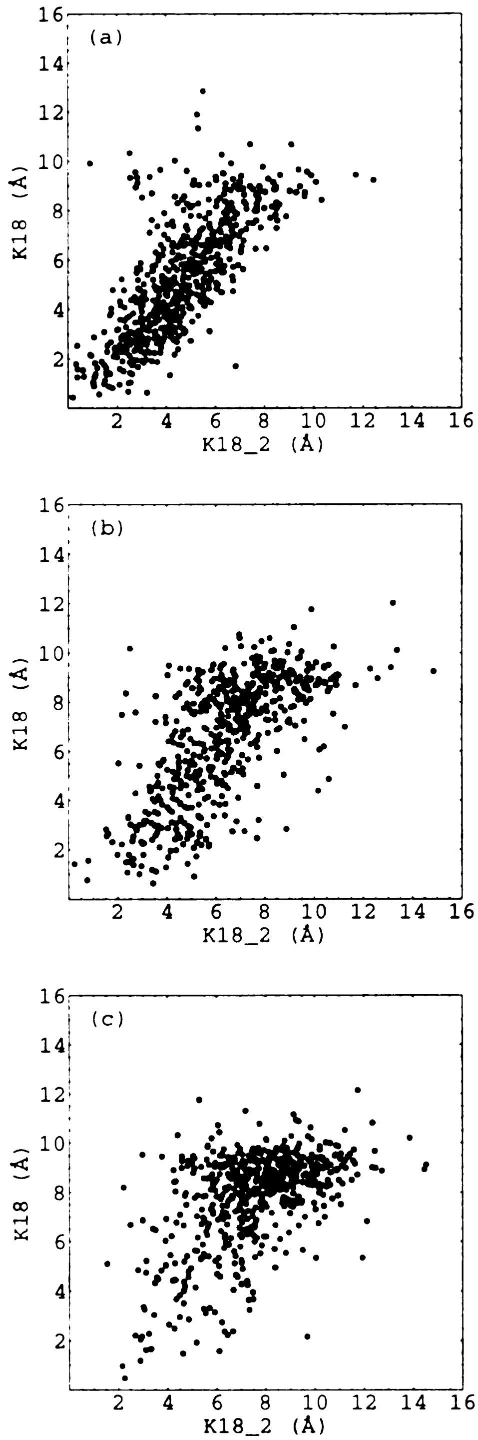

Figure 4.2 Distribution of K18 (HK1) and K18_2 (HK2) for three groups of stars separated by the value of their peak fluxes, flux_m. (a) high flux, (b) medium flux, and (c) low flux.

the Ca II ion effectively match the transitional energy at these temperatures. The last two properties resulted from the use of an identical exposure time for all stars regardless of their apparent brightness, which is an unavoidable situation with the objective prism technique. With regard to the third problem, the stellar spectra of faint stars without sufficient exposure time appear to be relatively noisy (although spectra which are too noisy to be useful, those with peak counts < 30,000, were eliminated in Chapter 2), so their continuum can be constructed inappropriately, leading to inaccurate equivalent width measurement. The final problem is due to excessive observing time for brighter stars (and the non-linear response of the photographic emulsion at high flux levels), which leads to a saturation of the continuum and underestimation of the measured equivalent widths. If the brighter stars were exposed for a shorter time, their K18_2 indices would be increased so the distribution slope in Figure 4.2 (a) would approach 1, like the others. Also, if the criterion for filtering out saturated spectra is reduced from 0.80 to a lower critical value (Subsection 2.3.4), spectra with better quality can be selected. However, we chose not to do this since we do not want to lose those spectra with acceptable quality.

4.2.3 Predicted and Fit K18 Index (K18_p & K18_f)

Improvement in the estimation of K18_2 could be achieved by individual consideration of the HK2 spectra with information of their temperatures, apparent brightness, and observing time. But this would require a great deal of time to accomplish, which breaks the spirit of this project – efficient data reduction in time as well as in quality (recall that there are 1.5 million stars in HK2 survey!).

Here, we make use of the ANNs to calculate the equivalent width of the Ca II K line with as high an accuracy as is feasible. To accomplish this goal, ANNs of various architecture were separately trained on each group by feeding on $(B\text{-}V)_0$ color, flux_m, and 50 raw fluxes around the Ca II K absorption line. The networks are expected to learn information concerning the apparent brightness of the star from the peak flux, flux_m. The supply of 50 raw fluxes is intended to help the network recognize a suitable continuum so K18_2 can be determined in an appropriate manner. In each group, the training set (seen data) consists of 500 metal-poor stars with their 52 input variables and one known output variable, K18 (Table 4.1). The validation sets (unseen data) for the trained networks are composed of 614, 559, and 596 stars, respectively, which have been shown in Figure 4.2 already. To avoid biasing our results, the seen and unseen data are divided according to K18 and color in a simliar manner.

Table 4.1 Data Set for K18_2 Calibration

	Flux_m (counts)	Training Set	Validation Set
Group 1	126,000 – 925,000	500	614
Group 2	69,000 – 126,000	500	559
Group 3	14,000 – 69,000	500	596

The feed-forward and back-propagation ANNs with a single hidden layer are employed once again. Masters (1993) has recommended that, as a general rule of thumb, the number of neurons in the hidden layer should be equal to the square root of the product of the number of inputs and the number of outputs, unless there are very few inputs and outputs. This guideline leads us to use about 7 neurons in this program because there are 52 input variables and 1 output variable. But one should note that this rule is only a rough approximation and can be applicable to only "significant" inputs to networks (those inputs which are not supplying redundant information), therefore various architectures should be tested to find the optimized structure.

As before, the trained networks were applied to both the training set (on itself) and the validation set, then the predicted K18_p were compared with the "true" K18. The results of this application are summarized by group in Table 4.2. For comparison, the same statistical parameters between true K18 and the "raw" (measured) K18_2 (discussed in Figure 4.2) are provided in the last two columns. In all cases of both seen and unseen data, the correlation coefficients and biweight estimator of scale, S_{BI}, of the residuals between K18_p and K18, are apparently improved relative to the results between K18_2 and K18 (in particular, for low fluxes). This means that the trained networks have learned how to produce the equivalent width from the complex input information, and the use of ANNs is superior to the direct calculation with an uncertain continuum. However, note that as flux_m decreases, the differences in the results between seen and unseen data increase. For the seen data sets in all groups, the correlation coefficients are larger than 0.82 with the biweight estimators less than 1.20 Å in the most of cases. But, for the validation sets, with the exception of Group 1, the results deviate from those for the seen data sets. This indicates that, for fainter stars, the trained networks are exhibiting a tendency to "remember" the relationships between inputs and the output, rather than learning general patterns. Nonetheless, the networks' results for unseen data are always much better than obtained from K18_2 itself, thus this method will be employed in the remainder of thesis. An interesting point is that the c.c. and S_{BI} can vary inconsistently. Note the results for the validation sets in Groups 2 and 3 – fainter stars show a worse c.c., but better S_{BI}, as compared to stars in the 2nd group. This is the reason why one should consider both the correlation coefficient and robust estimator of the residual scale simultaneously. The trained networks that produce the best results in each group are selected to be used in the K18 index calibration, and will be called "k18-h.net," "k18-m.net," and "k18-l.net" respectively, denoting high, medium, and low flux values.

Table 4.2 K18_2 Calibration Results

	Architecture	Training Set		Validate Set		K18 vs K18_2	
		c. c.	S_{BI}	c. c.	S_{BI}	c. c.	S_{BI}
Group 1	52 : 2 : 1	0.82	1.23	0.8032	1.31	0.74	1.38
	52 : 4 : 1	0.83	1.17	**0.8151**	**1.26**		
	52 : 6 : 1	0.83	1.20	0.8084	1.31		
	52 : 8 : 1	0.79	1.32	0.8010	1.28		
	52 : 10 : 1	0.84	1.16	0.8113	1.28		
Group 2	52 : 2 : 1	0.87	1.19	0.7901	1.38	0.67	1.87
	52 : 4 : 1	0.88	1.16	0.7954	1.36		
	52 : 6 : 1	0.87	1.22	0.7977	1.38		
	52 : 8 : 1	0.87	1.18	**0.7978**	**1.36**		
	52 : 10 : 1	0.87	1.17	0.7901	1.39		
Group 3	52 : 2 : 1	0.84	0.93	0.6821	1.11	0.51	1.97
	52 : 4 : 1	0.83	0.98	0.6872	1.21		
	52 : 6 : 1	0.82	1.01	**0.7005**	**1.19**		
	52 : 8 : 1	0.83	0.99	0.6891	1.15		
	52 : 10 : 1	0.84	0.96	0.6822	1.14		

The distributions between K18 and K18_p (as predicted by the selected networks) for the unseen data sets only are shown in Figure 4.3. As can be seen, K18 and K18_p have a much improved linear relationship, as compared to the results for K18 and K18_2 shown in Figure 4.2, although the scatter still becomes larger as the flux decreases. The slope of distribution of for the higher flux subsample becomes close to 1, and the scatter in lower fluxes are distinctively reduced. Note that the predicted indices saturate near 2 Å, which is a general result for the application of ANNs, as discussed previously.

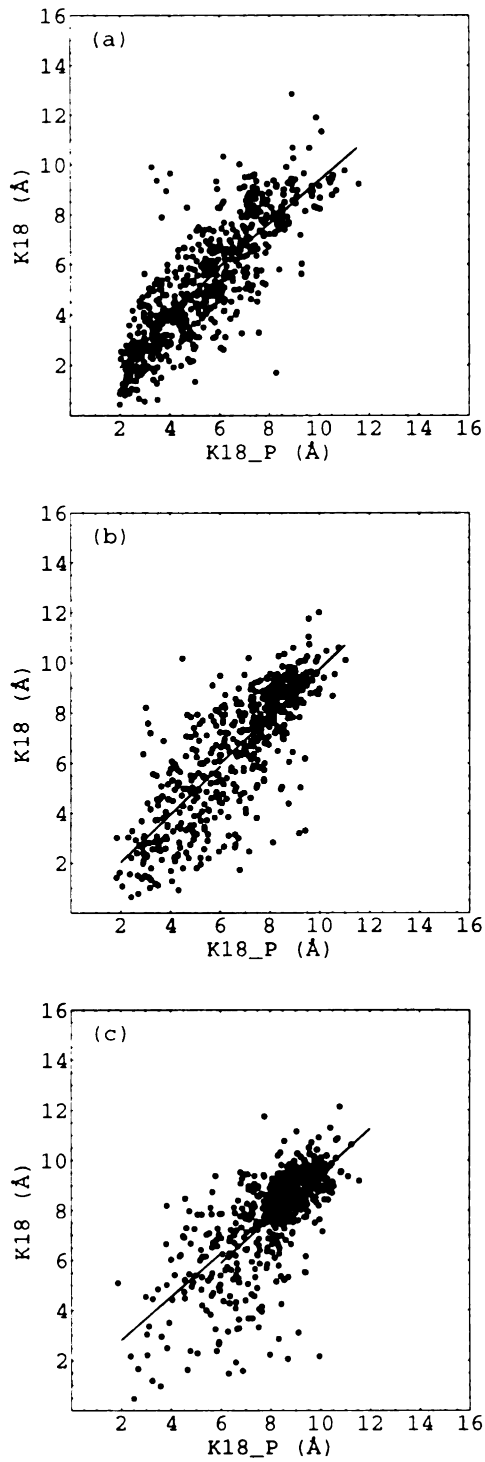

Figure 4.3 Predicted line index K18_p, as compared to K18, for three groups of stars separated by peak flux, flux_m. (a) high flux, (b) medium flux, and (c) low flux.

In order to make K18_p as reliable as possible, piecewise linear fittings were performed to the distributions between K18 and K18_p – the fit lines are shown together in Figure 4.3. Each group is divided into two parts at K18_p = 6 Å, which is the middle of the entire range of K18_p, and then fit separately to a linear relation with K18. The functional forms of the "fit" K18 indices (K18_f) and their robust estimator of the rms residual are presented in Table 4.3. These fit indices, K18_f, will be used as one of inputs into mp-p.net and mp-c.net for the process of prediction and classification.

Table 4.3 Fit Functions of K18_2

	K18_p < 6 Å		K18_p > 6 Å	
	Fit Function	S_{BI}	Fit Function	S_{BI}
Group 1	K18_f = 0.997 K18_p – 0.086	1.19	K18_f = 0.862 K18_p + 0.751	1.35
Group 2	K18_f = 0.962 K18_p + 0.104	1.67	K18_f = 0.943 K18_p + 0.327	1.14
Group 3	K18_f = 0.866 K18_p + 1.080	1.89	K18_f = 0.893 K18_p + 0.544	1.02

Figure 4.4 presents the relations of residuals (K18 – K18_f) over K18_f, grouped by line strength and flux. Generally they are evenly distributed around 0 in the vertical direction, but some outliers appear in the region of larger line strengths in groups 2 and 3. Histograms of the residuals for the groups, separated by equivalent width and flux, are shown in Figure 4.5.

4.3 Prediction and Classification

The 1769 known metal-deficient stars which were members of the three validation sets in K18 index calibrations were used again in the estimation of [Fe/H] and the determination of MP-class. Because their $(B-V)_0$ colors and metal abundance are in hand, and they have never been involved in the training process for the K18

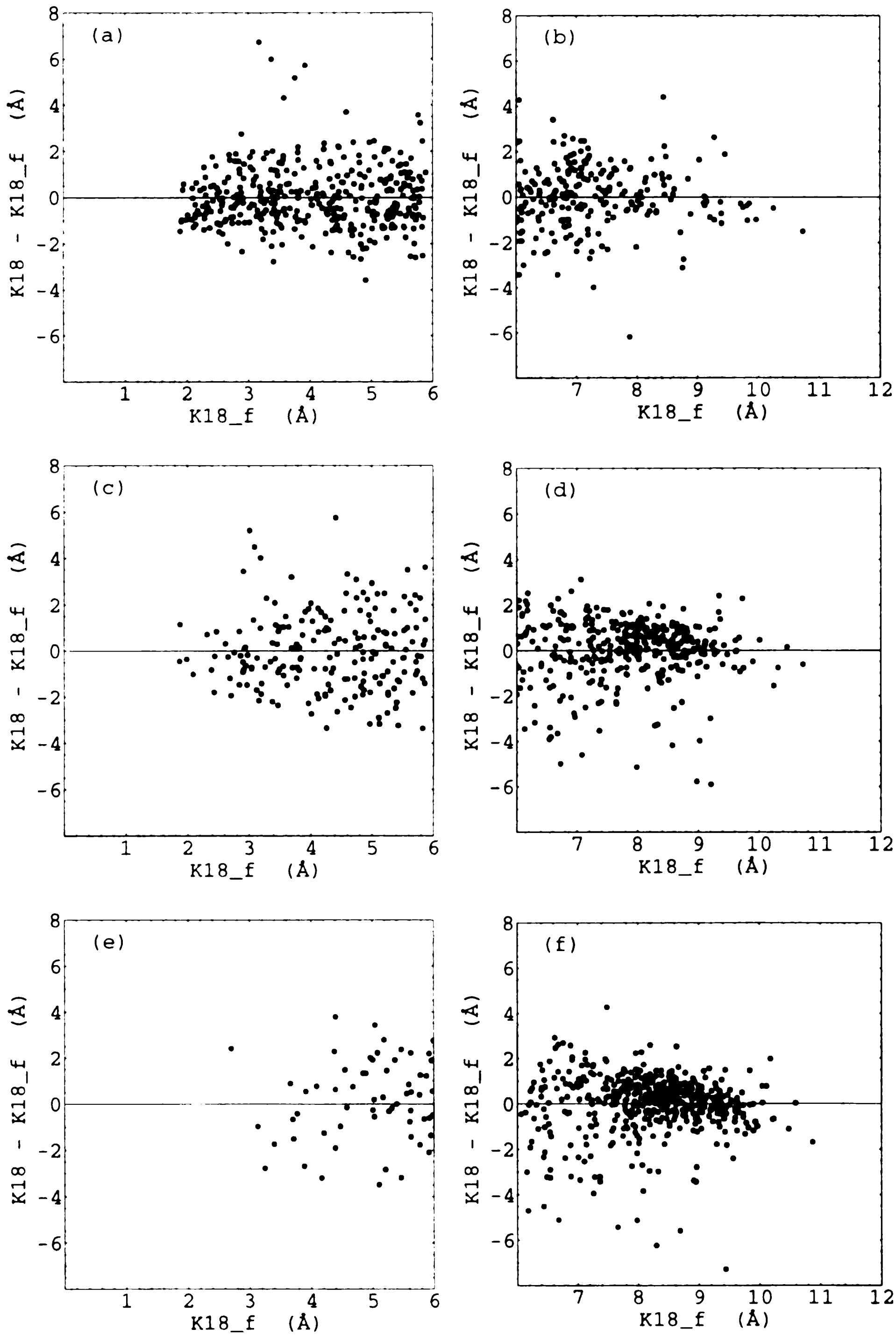

Figure 4.4 The residuals (K18-K18_f) shown as a function of K18_f, grouped by line strength and flux_m. (a) high flux / weaker line strength, (b) high flux / stronger line strength, (c) medium flux / weaker line strength, (d) medium flux / stronger line strength, (e) lower flux / weaker line strength, and (f) lower flux / stronger line strength.

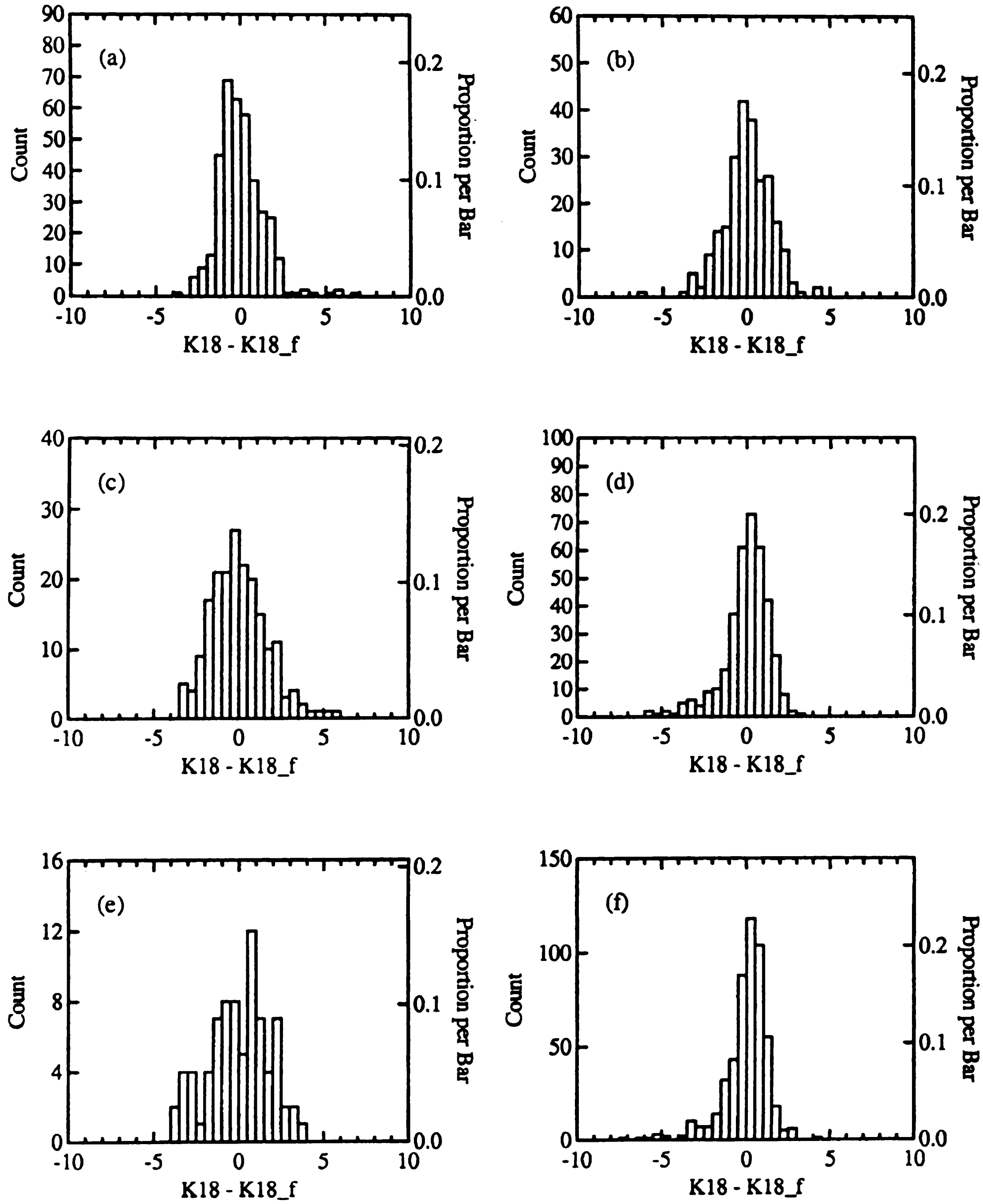

Figure 4.5 Histograms of the residuals for the groups, separated by line strength and flux_m. Bins are 0.5 Å in width. The order of the plots are the same as in Figure 4.4.

calibration, their use promises unbiased results, and thus an objective analysis is possible.

It is worth reviewing the entire procedure for the selection of candidate metal-poor stars in the case where colors are available. The HK2 spectra need to be classified into 3 groups by flux_m, and then the trained networks for K18 calibration (k18_h.net, k18_m.net, and k18_l.net) feed on 50 raw fluxes, known colors and flux_m to produce K18_p. The 6 fit functions are used to convert K18_p into K18_f. These procedures were fully demonstrated in the previous section. Finally the known $(B-V)_0$ color and K18_f are fed into mp-p.net and mp-c.net in order to predict their metallicity and determine MP-class.

Figure 4.6 shows the relationship between true [Fe/H] and predicted [Fe/H]_p estimated by mp-p.net with K18_f and real $(B-V)_0$. The correlation coefficient and robust estimator S_{BI} between [Fe/H] and [Fe/H]_p are 0.64 and 0.59 dex respectively. For stars with true [Fe/H] > −1, the trained network tends to underestimate the metallicity [Fe/H]_p. As seen in Figure 3.2, the vertical spacing between the contours of [Fe/H] > −1 is about 1 Å per 0.5 dex of [Fe/H], and the metal-deficient stars with [Fe/H] > −1 have K18 greater than 6 Å, generally. In all cases, the robust estimator S_{BI} between K18_f and K18 is greater than 1 Å (Table 4.3) and stars with large K18_f indices are underestimates relative to the true K18 (Figure 4.4 (d) and (f)). As a result, the metal abundances are underestimated for those stars. However, as [Fe/H] decreases, the vertical spacing between iso-metallicity contours increases gradually, so that metallicity is less affected by the scatter in K18_f. Thus, one obtains a better relationhip between [Fe/H] and [Fe/H]_p for the stars of lower metal abundance. Note, however, that [Fe/H]_p has a tendency

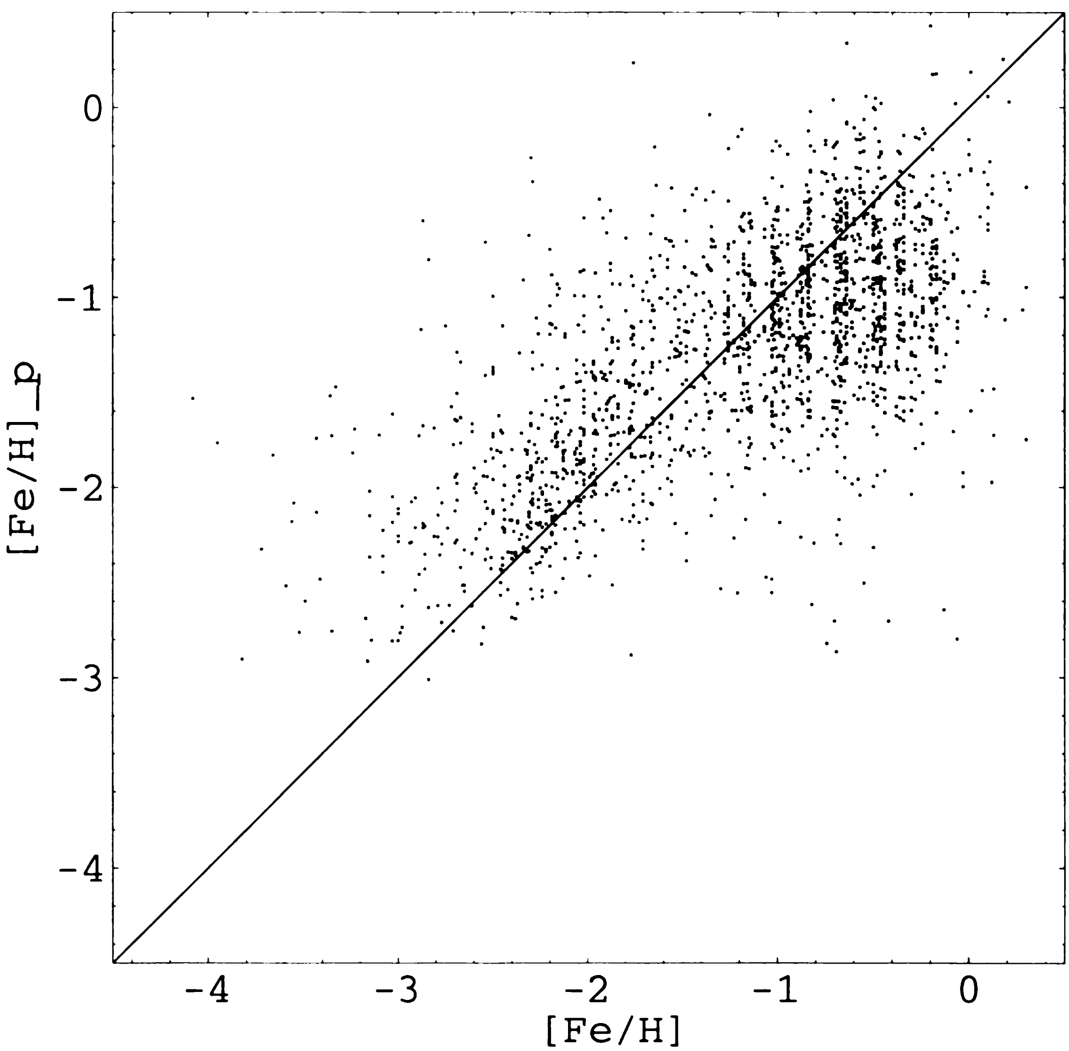

Figure 4.6 Predicted [Fe/H] compared to known [Fe/H] for metal-poor stars in the validation set. The metal abundance is estimated from known colors and the calibrated K18_f index. A one-to-one line is shown.

to saturate near [Fe/H] = –3.0. This is due to the saturation of K18_p and K18_f near 2 Å (Figure 4.3). As seen in Figure 3.2, mp-p.net does not generate estimates of [Fe/H] < –3.0 with K18 of 2 Å for stars hotter than $(B\text{-}V)_0 \sim 0.55$. Because stars with $(B\text{-}V)_0 < 0.55$ represent more than half in our sample, it is difficult for mp-p.net to generate metallicity estimates less than [Fe/H]_p = –3.0.

Although the results obtained with the calibrated K18_f index are not as good as are obtained from those with known K18, our results are still quite useful for pre-selection of candidate metal-poor stars. Tables 4.4 and 4.5 display statistical quantities for hotter stars and cooler stars, respectively. The meanings of columns are as follows:

Column (1): Metallicity cutoff
Column (2): Numbers of stars in the unseen set with known [Fe/H] below the cutoff
Column (3): Numbers of stars in the unseen set with predicted [Fe/H]_p below the cutoff
Column (4): Numbers of stars that have correctly assigned abundances below the cutoff
Column (5): Recovery – percentage of stars whose abundances are correctly assigned below the cutoff, as compared to all stars whose real abundances are below the cutoff (= col(4)/col(2) × 100)
Column (6): Efficiency – percentage of stars whose abundances are correctly assigned below the cutoff, as compared to all stars whose predicted abundances are below the cutoff (= col(4)/col(3) × 100)

For example, of the 148 cooler stars in the unseen set known to have [Fe/H] < –2.0, 93 stars are correctly predicted by the ANN to have [Fe/H] < –2.0. Thus 37.2% are missed, and 62.8% are recovered by the prediction procedure. Among 122 cooler stars in the validation set predicted to have abundance [Fe/H] < –2.0, 93 of them in fact satisfy this criterion (76.2% efficiency). In other words, if we were to observe 100 candidate metal-poor stars whose [Fe/H] was predicted to be less than –2.0, then we should be able to collect 76 true extremely metal-poor stars with [Fe/H] < –2.0.

This efficiency should be compared to the effective yield (EY) which was defined in Chapter 2. For the HK survey with visual inspection, the EY of stars with [Fe/H] < –2.0 was ~ 32% when B-V color information was available prior to conducting the spectroscopic follow-up. In our application, the efficiency of both hotter and cooler stars with [Fe/H] < –2.0 is about 76% with previous color information, which is a greatly improved result. Extremely metal-deficient cooler stars have an apparently better recovery than for hotter stars. This is attributed to the saturation of K18_2 near 2 Å again, from which cooler stars do not suffer. A re-calibration of the K18 index for hotter stars with K18_2 < 2 Å is likely to improve the recovery rate. This effort will be made in the near future.

Next, the mp-c.net was fed on known colors and K18_f to determine the MP-class of stars in the unseen set. The results are shown in Table 4.6. The second row gives correction rates; the number of stars in each group is provided in the last row. For example, of 148 known cooler metal-poor stars (MP-class 2) which are our ultimate targets, 82 stars are correctly classified into MP-class 2 by mp-c.net (correction rate: 58.8%). This enables us to make a sample of cooler metal-poor star candidates in a highly efficient manner. Stars in MP-class 1 have the lowest correction rate as a result of the saturation of K18_p.

Table 4.4 Recovery and Efficiency for Hotter Stars ($(B-V)_0 \leq 0.50$)

Cutoff	[Fe/H]	[Fe/H]_p	Correct	Recovery (%)	Efficiency (%)
≤ -3.5	4	0	0	0.0	N/A
≤ -3.0	17	0	0	0.0	N/A
≤ -2.5	68	6	2	2.9	33.3
≤ **-2.0**	230	129	99	**43.0**	**76.7**
≤ -1.5	385	340	278	72.2	81.8
≤ -1.0	497	576	426	85.7	74.0
≤ -0.5	739	793	680	92.0	85.8
≤ 0.0	885	884	875	98.9	99.0
≤ +0.5	895	894	894	99.9	100.0
≤ +1.0	895	895	895	100.0	100.0

Table 4.5 Recovery and Efficiency for Cooler Stars ($(B-V)_0 > 0.50$)

Cutoff	[Fe/H]	[Fe/H]_p	Correct	Recovery (%)	Efficiency (%)
≤ -3.5	5	0	0	0.0	N/A
≤ -3.0	21	1	0	0.0	0.0
≤ -2.5	63	45	24	38.1	53.3
≤ **-2.0**	148	122	93	**62.8**	**76.2**
≤ -1.5	233	280	172	73.8	61.4
≤ -1.0	414	571	329	79.5	57.6
≤ -0.5	686	831	663	96.6	79.8
≤ 0.0	852	870	851	99.9	97.8
≤ +0.5	874	874	874	100.0	100.0
≤ +1.0	874	874	874	100.0	100.0

Table 4.6 Classification Results

	Overall	MP-Class 1	**MP-class 2**	MP-class 3	MP-class 4	MP-class 5	MP-class 6
Correction Rate (%)	55.85 %	39.6 %	**58.8 %**	67.4 %	67.3 %	62.3 %	44.1 %
Number	1769	230	148	267	266	398	460

Chapter 5

COLOR INDEX CALIBRATION

5.1 Overview

With 821 unique stars for which observed $(B-V)_0$ colors are available from the HK survey photometric follow-up (HK1), their corresponding low-resolution digital spectra (HK2), and estimates of calibrated photographic apparent magnitudes in several bands (B,R,I) obtained from the SuperCOSMOS Sky Surveys (hereafter, SSS), the Artificial Neural Networks are trained in order to estimate the $(B-V)_0$ color index for stars *without* available photometric observations, directly from the low-resolution spectra extracted from the APM scans (HK2) and the SSS magnitudes. Piecewise linear fitting is performed between the predicted $(B-V)_0$ color (hereafter, referred as to $(B-V)_0$_p) and the observed $(B-V)_0$ color in order to obtain a new color estimate, the fit color (hereafter, called $(B-V)_0$_f), which is the best estimated value. The $(B-V)_0$_f colors are then used as one of the input variables into k18-h.net, k18-m.net, and k18-l.net (the trained networks discussed in Chapter 4) for the K18 index calibration. Finally, $(B-V)_0$_f and K18_f are used as inputs into mp-p.net and mp-c.net (the trained networks discussed in Chapter 3) to estimate [Fe/H] and to determine the MP-class. The efficiency and recovery of these results are discussed.

5.2 Color Index Calibration

5.2.1 Data Set

By matching up the positional coordinates for 5218 stars (including several thousand bluer FHB/A stars, as well as the metal-poor stars) with observed $(B-V)_0$ colors

(HK1), stellar spectra in the 87 digitally scanned plates (HK2), and stars with available apparent magnitudes (B, R, I) in the portion of the SSS which has been calibrated to date (the region $b < -55$, toward the South Galactic Pole), 899 stars were matched with a criterion of their angular separation being less than 20 seconds of arc. Among those, 28 stars were ruled out due to multiple matches (16) or mismatches (12) determined by comparison of B magnitudes in HK1 and SSS. An additional 50 stars were dropped, because only one magnitude band for them was available from the SSS. The remaining 821 unique stars with observed $(B-V)_0$, low-resolution (HK2) spectra, and multiple-band SSS magnitudes form the data set discussed in this section.

The SuperCOSMOS Sky Survey is an ongoing effort by the Wide Field Astronomy Unit (WFAU), Institute for Astronomy, with an advanced machine that digitizes photographic sky survey plates taken with UK Schmidt Telescope (UKST), the ESO Schmidt, and the Palomar Schmidt. The SSS presently covers some 5,000 square degrees (200 standard UKST fields with $b < -60$) around the South Galactic Cap (SSS 2000).

Figure 5.1 shows the relationship between the (calibrated) photographic B magnitude obtained from the SSS (hereafter, referred as to Bj) and the photoelectric B magnitude observed in the HK Survey for the 821 stars. There is a clear linear relationship between these two measures, but there exists a scatter of roughly 1 magnitude , and Bj is somewhat less than B, overall. The B magnitude is believed to be very accurate (Δ B ~ 0.01-0.02 mag; Beers et al. 1999). Bj is the roughly calibrated magnitude in digitized sky survey plates taken with the UK Schmidt Telescope (UKST) and may contain systematic errors as a function of position on the plate (SSS 2000). Bj is available for all stars in our data set, but the other three

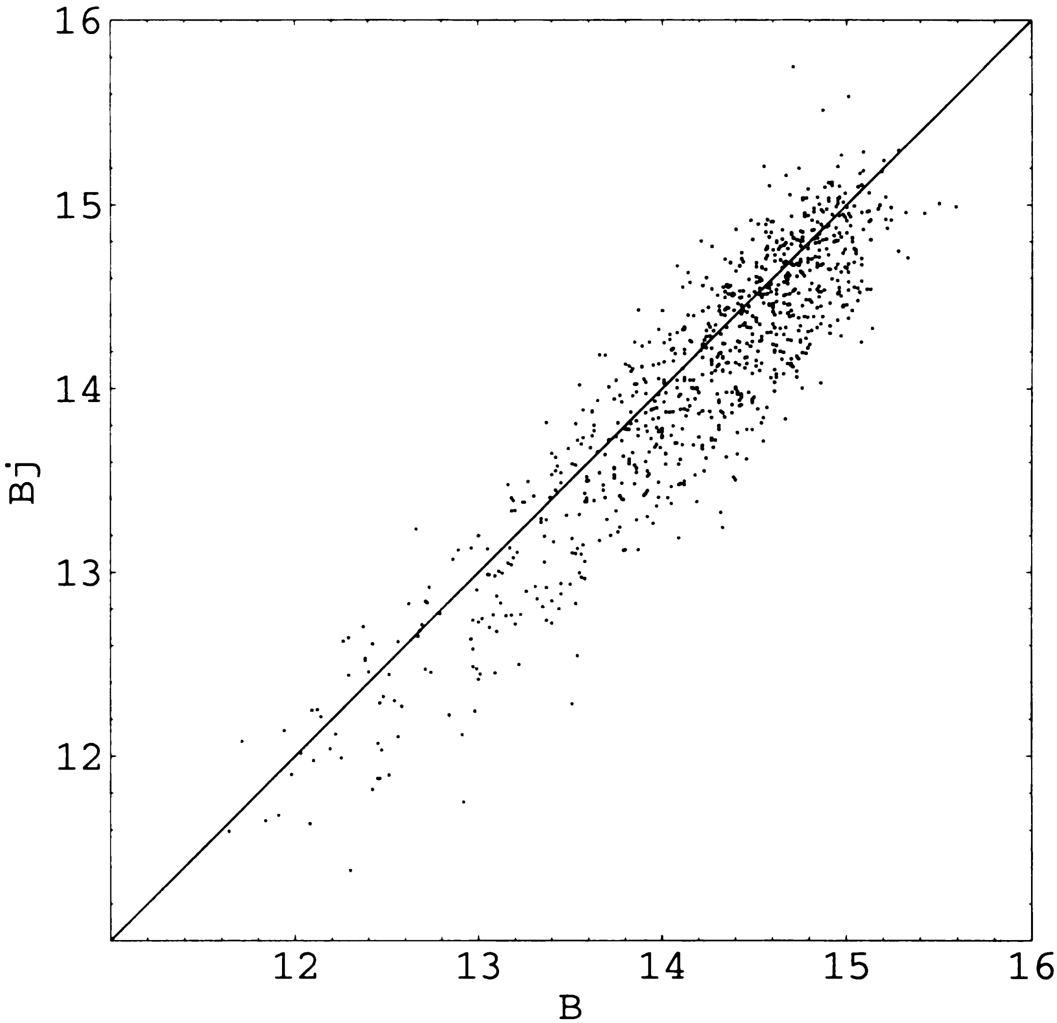

Figure 5.1 Relationship between photographic B magnitude in the SSS (Bj) and photoelectric B magnitude from the HK Survey (B). A one-to-one line is shown.

bands – R1 (ESO Schmidt and Palomar Schmidt), R2 (UKST), and I (UKST) – are not always available, as shown in Table 5.1. The marks O and X mean available and non-available, respectively.

Table 5.1 Data Set (Unique Stars) Obtained from SSS

Availability				Number
Bj	R1	R2	I	
O	O	O	O	370
O	X	O	O	185
O	O	X	O	35
O	O	O	X	84
O	X	X	O	22
O	O	X	X	22
O	X	O	X	103
Total				821

5.2.2 Predicted and Fit Color Index ($(B-V)_0$_p & $(B-V)_0$_f)

We make use of the ANNs to estimate $(B-V)_0$ color with as high an accuracy as possible at present. To achieve this goal, ANNs of various architecture were separately trained on each group of matched stars, categorized by the availability of magnitudes, by feeding on available SSS magnitudes, flux_m, and 200 flux estimates in the continua as derived in Chapter 2 (Figure 2.4 (a)). The position of the absorption peak of Ca II K line corresponds to the 75th pixel (of 200 input pixels). The combined use of the various magnitude bands provides information on the stellar color which we seek to extract. The stellar continua are the intensities of blackbody radiation at the surface temperature of the star, modified by the response of the photographic emulsion of the original HK survey, and the transmission of the interference filter + telescope optics + the Earth's atmopshere. Thus, the networks are expected to learn information regarding the color temperature of the stars from the shape of the individual continua. However, as discussed in Subsection 2.2.2, the continua can be distorted on the spectra of too bright (saturation) or too faint (noisy) stars. Therefore, flux_m needs to be fed into the network to provide information about the apparent brightness of the stars.

Table 5.2 Data Set for Color Estimation

	Availability				Total	Training Set	Validation Set	Ratio (V/T)
	Bj	R1	R2	I				
Group 1	O	O	O	O	370	240	130	0.54
Group 2	O	X	O	O	555	240	315	1.31
Group 3	O	O	X	O	405	240	165	0.69
Group 4	O	O	O	X	454	240	214	0.89
Group 5	O	X	X	O	612	240	372	1.55
Group 6	O	O	X	X	511	240	271	1.13
Group 7	O	X	O	X	742	240	502	2.09

Table 5.2 summarizes the data sample used in our neural networks for color estimation. The groups are determined by the available magnitude bands, as in Table 5.1, but the difference is that a single star can be used in several groups according to its available magnitudes. For example, stars in Group 1 can participate in the training process in all other groups since they have all magnitude bands available – Bj, R1, R2 and I. Because members in Group 2 have Bj, R2, and I, they can join the training process for Group 5, which requires only two kinds of magnitudes – Bj and I. The sixth column in the table indicates the number of stars in each group, collected by the above method. In each group, the training set (seen data) consists of 240 stars with their possible inputs (203 to 205) and one known output $(B-V)_0$ color. To ensure fairness of training for all groups, the same number of stars (240) was allocated into the training sets. This number, 240, was determined by considering the ratio of the number of stars in the validation set to the number of

stars in the training set. The ratio shown in the last column is intended to be between 0.5 and 2.0 to avoid unwanted over-fitting, due to a surplus of information, or incorrect fitting, due to lack of information. As always, the seen and unseen sets are evenly divided according to color and peak flux to obtain unbiased results from the trained networks.

As before, the feed-forward and back-propagation ANNs with a single hidden layer were tested by increasing the number of hidden neurons from 2 to 10. The trained networks were applied to both the seen set (on itself) and unseen set, and then the predicted $(B\text{-}V)_{0}$_p colors were compared to the known $(B\text{-}V)_0$ colors. The statistical results of this approach are presented by group in Table 5.3. For comparison, the last two columns show the same statistical quantities between true $(B\text{-}V)_0$ color and $(B\text{-}V)_{0}$_p, as estimated by the networks which were trained without the continuum information. In all cases, for both seen and unseen data, the results of the correlation coefficients and robust estimator S_{BI} derived from the networks trained with continuum information are clearly improved relative to those estimated from the networks trained without continuum information.

For the training sets, the correlation coefficients are always reasonably high, and the fluctuation of c.c and S_{BI} is not severe from group to group. However, the results from the validation sets are always worse than those with training sets, and are very different from group to group. For example, the difference of c.c. and S_{BI} between seen and unseen sets with the best architecture in Group 7 are 0.15 and 0.05 respectively, whereas nearly the same results are obtained in Group 5. As expected, the results for the validation sets become worse as the number of SSS magnitudes decreases, in general. There are two possible reasons for this behavior. As was the case for the K18 calibration, the trained networks may be tending to

Table 5.3 Color Calibration Results

	Architecture	Training Set		Validation Set		w/o Continuum	
		c. c.	S_{BI}	c. c.	S_{BI}	c. c.	S_{BI}
Group 1	205 : 2 : 1	0.92	0.11	0.8455	0.13		
	205 : 4 : 1	0.91	0.11	0.8475	0.13		
	205 : 6 : 1	0.91	0.11	**0.8622**	**0.13**		
	205 : 8 : 1	0.90	0.11	0.8387	0.13		
	205 : 10 : 1	0.90	0.12	0.8485	0.13	0.81	0.16
Group 2	204 : 2 : 1	0.90	0.12	0.8262	0.14		
	204 : 4 : 1	0.90	0.11	0.8261	0.14		
	204 : 6 : 1	0.89	0.11	**0.8277**	**0.14**		
	204 : 8 : 1	0.87	0.13	0.8153	0.15		
	204 : 10 : 1	0.86	0.13	0.8163	0.15	0.76	0.17
Group 3	**204 : 2 : 1**	0.92	0.10	**0.8378**	**0.13**		
	204 : 4 : 1	0.90	0.11	0.8326	0.14		
	204 : 6 : 1	0.90	0.11	0.8200	0.14		
	204 : 8 : 1	0.89	0.12	0.8278	0.13		
	204 : 10 : 1	0.89	0.12	0.8154	0.14	0.83	0.15
Group 4	204 : 2 : 1	0.88	0.12	0.7836	0.15		
	204 : 4 : 1	0.90	0.10	**0.7945**	**0.15**		
	204 : 6 : 1	0.90	0.10	0.7911	0.15		
	204 : 8 : 1	0.89	0.11	0.7790	0.14		
	204 : 10 : 1	0.88	0.12	0.7799	0.15	0.77	0.17
Group 5	203 : 2 : 1	0.88	0.13	0.8396	0.14		
	203 : 4 : 1	0.89	0.12	0.8212	0.14		
	203 : 6 : 1	0.88	0.12	0.8353	0.14		
	203 : 8 : 1	0.88	0.13	**0.8473**	**0.13**		
	203 : 10 : 1	0.88	0.13	0.8325	0.14	0.75	0.18
Group 6	203 : 2 : 1	0.84	0.14	0.76	0.15		
	203 : 4 : 1	0.86	0.13	**0.78**	**0.14**		
	203 : 6 : 1	0.86	0.13	0.74	0.15		
	203 : 8 : 1	0.85	0.14	0.75	0.15		
	203 : 10 : 1	0.88	0.13	0.74	0.15	0.73	0.18
Group 7	203 : 2 : 1	0.89	0.12	0.7215	0.15		
	203 : 4 : 1	0.88	0.11	**0.7303**	**0.16**		
	203 : 6 : 1	0.86	0.12	0.6969	0.16		
	203 : 8 : 1	0.84	0.13	0.7001	0.16		
	203 : 10 : 1	0.86	0.12	0.6846	0.17	0.69	0.19

remember the maps from inputs to the output, rather than developing general relationships. Secondly, although the addition of the 200 continua fluxes significantly contribute to the learning process for ANNs, the input significance of each SSS magnitude band cannot be ignored. Focus on the "good" results for unseen data in Groups 1, 2, 3, & 5, where the I magnitude was used as an input variable. This means that the I magnitude is providing very important information. In this context, if we had another kind of magnitude, bluer than the B band (e.g., a U magnitude), then the ANNs would do a better job in the $(B-V)_0$ calibration, since the networks would be able to feed on both bluer and redder information than supplied by the B and V magnitudes.

As a simple test of the above suggestion, two networks have been trained to predict from 4 magnitudes (Bj, R1, R1 and I) the B and V separately. As expected, the networks were able to predict V magnitude (c.c.: 0.98, S_{BI}: 0.17) better than B magnitude (c.c.: 0.95, S_{BI}: 0.28), because V is in between Bj and R in wavelength. The trained networks that show the best results in each group are picked up to be used in the $(B-V)_0$ calibration, and will be called bv-#.net where # is group number.

The distributions between $(B-V)_0$ and $(B-V)_{0}$_p for the validation sets only are displayed by group in Figure 5.2. Linear relationships with small scatter are seen the bluer regions, but the linearity is destroyed , with many outliers present, for $(B-V)_0 >$ 0.6, due to the lack of data to be trained in the region. In order to make $(B-V)_{0}$_p as reliable as possible, piecewise linear fittings were applied to to the distributions between $(B-V)_0$ and $(B-V)_{0}$_p. Each group is divided into two parts at $(B-V)_{0}$_p = 0.6, the point where the scatter becomes broader, and then fit separately to linear relations with $(B-V)_0$. The fit lines are shown together in Figure 5.2. The functional forms of the fit colors and their biweight estimators are presented in Table 5.4. The robust estimator S_{BI} is roughly 0.12 for hotter stars, and 0.20 for cooler stars. However, it should be kept in mind that the resulting errors which are imparted to stimates of [Fe/H] from mp-p.net will be rather *similar* for these two color regions.

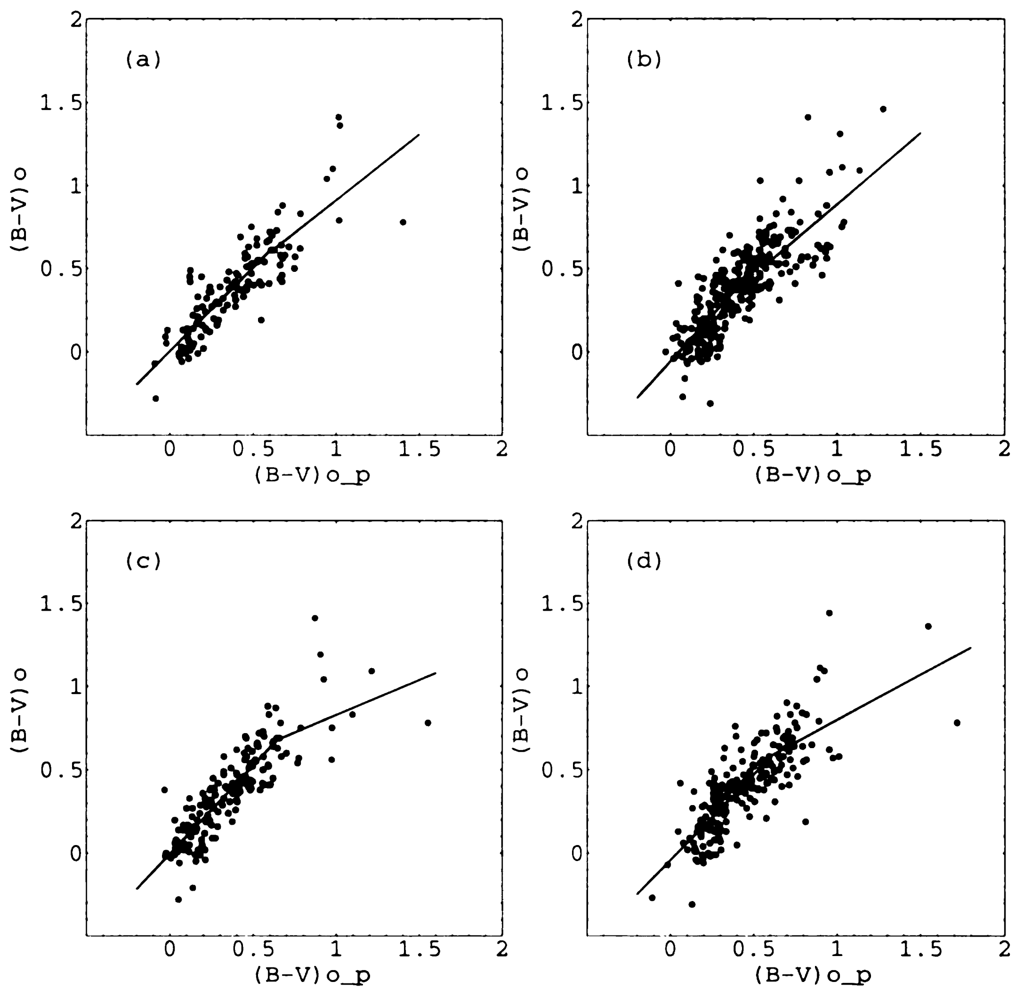

Figure 5.2 Predicted $(B\text{-}V)_0$, as compared to known $(B\text{-}V)_0$, for seven groups of stars separated by the availability of SSS magnitude bands. (a) group 1, (b) group 2, (c) group 3, (d) group 4, (e) group 5, (f) group 6, and (g) group 7. The lines shown are piecewise linear fits to the distributions.

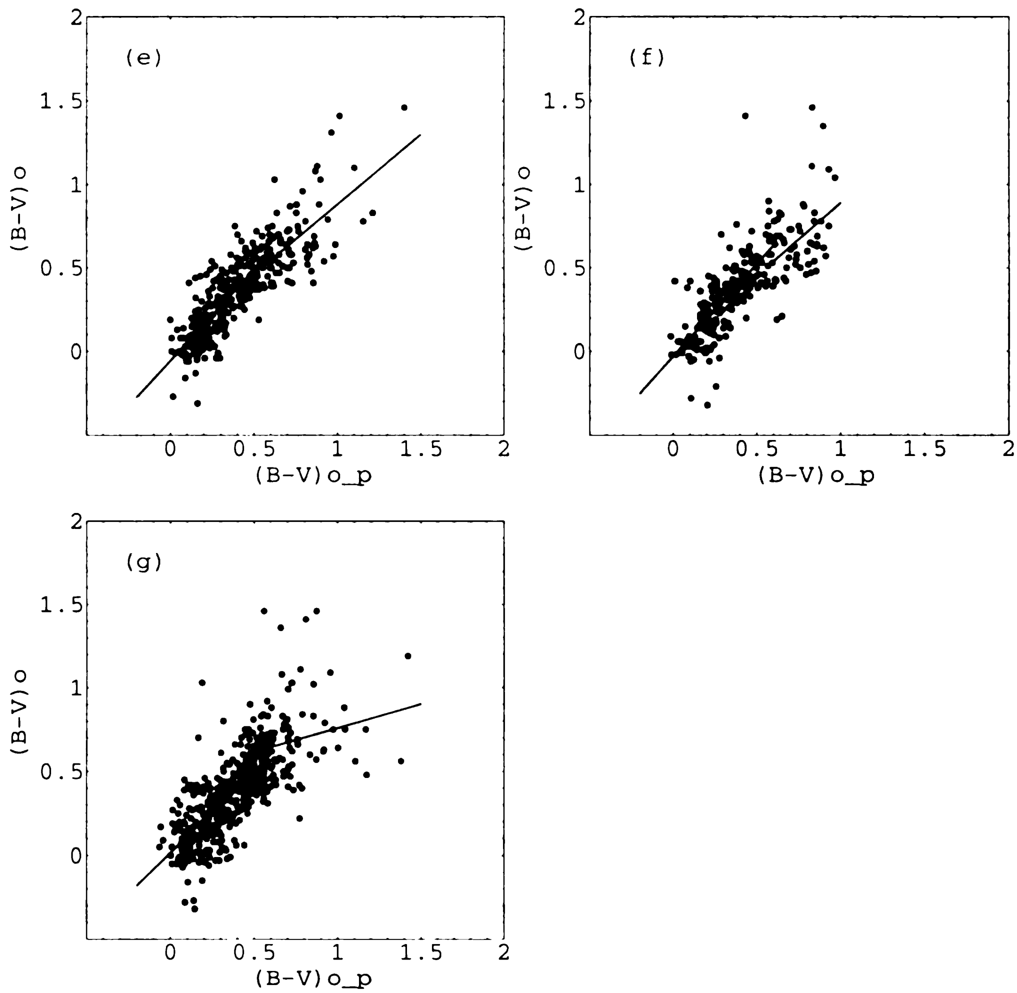

Figure 5.2 (continued)

Refer back to Figure 3.2. The slope of the iso-metallicity contours is steep in the hotter regions, but becomes more gentle in the cooler regions. Thus the scatter in [Fe/H]_p with $(B-V)_0$_f at a fixed K18 index is expected to be similar for these regions, on the order of about 0.5 dex. These fit colors, $(B-V)_0$_f, will be used as one of the inputs into k18-h.net, k18-m.net, and k18-l.net for the K18 index calibration, and then fed again into mp-p.net and mp-c.net for the process of prediction and classification.

Table 5.4 Fit Function for Color Calibration

	$(B-V)_0$_p ≤ 0.60		$(B-V)_0$_p > 0.60	
	Fit function	S_{BI}	Fit function	S_{BI}
Group 1	$(B-V)_0$_f = 1.003 $(B-V)_0$_p + 0.005	0.11	$(B-V)_0$_f = 0.789 $(B-V)_0$_p + 0.123	0.21
Group 2	$(B-V)_0$_f = 1.095 $(B-V)_0$_p – 0.057	0.13	$(B-V)_0$_f = 0.857 $(B-V)_0$_p + 0.030	0.19
Group 3	$(B-V)_0$_f = 1.062 $(B-V)_0$_p – 0.005	0.12	$(B-V)_0$_f = 0.418 $(B-V)_0$_p + 0.410	0.19
Group 4	$(B-V)_0$_f = 1.026 $(B-V)_0$_p – 0.043	0.13	$(B-V)_0$_f = 0.542 $(B-V)_0$_p + 0.256	0.19
Group 5	$(B-V)_0$_f = 1.089 $(B-V)_0$_p – 0.056	0.12	$(B-V)_0$_f = 0.835 $(B-V)_0$_p + 0.046	0.19
Group 6	$(B-V)_0$_f = 1.107 $(B-V)_0$_p – 0.031	0.12	$(B-V)_0$_f = 0.877 $(B-V)_0$_p + 0.013	0.20
Group 7	$(B-V)_0$_f = 0.976 $(B-V)_0$_p + 0.015	0.14	$(B-V)_0$_f = 0.286 $(B-V)_0$_p + 0.473	0.21

Figure 5.3 shows the relationship of the residuals ($(B-V)_0$ - $(B-V)_0$_f) over (B-V)$_0$_f, classified by color class and availability of various SSS magnitude bands. In the hotter region, they are evenly distributed around 0 in the vertical direction, but some outliers appear in the cooler region, as expected. Figure 5.4 presents the histograms of the residuals for the same groups shown in the previous pictures.

5.3 Prediction and Classification

Here, we demonstrate the entire procedure for the selection of metal-poor star candidates in the case where *both* known $(B-V)_0$ colors and measured K18 indices are not available. This is of course is the situation that will apply in general for the

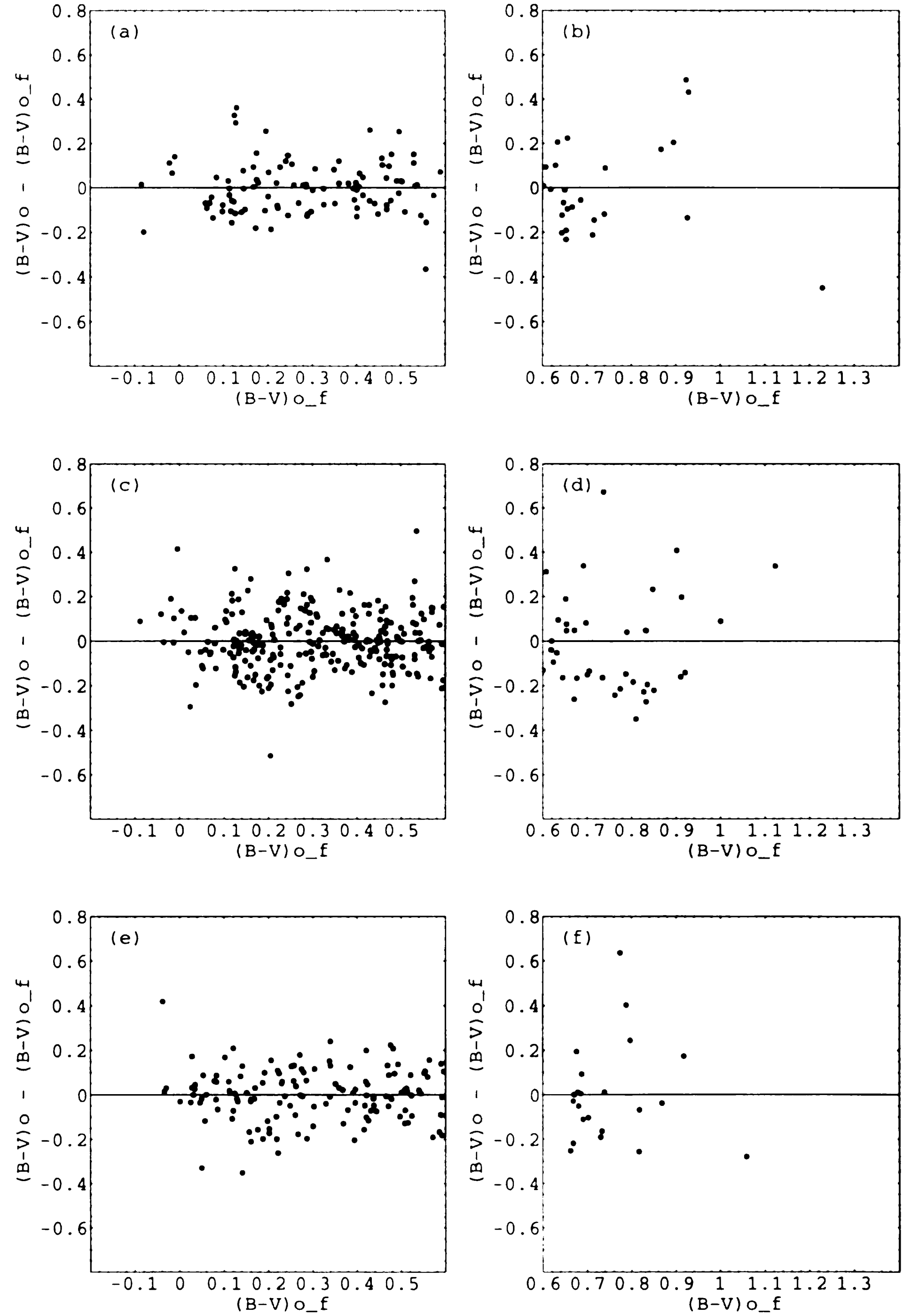

Figure 5.3 The residuals ((B-V)$_0$-(B-V)$_0$_f) shown as a function of (B-V)$_0$_f, grouped by temperature and availability of the SSS magnitude bands. The left-hand panels correspond to the hotter stars in each group, while the right-hand panels are the cooler stars in each group.

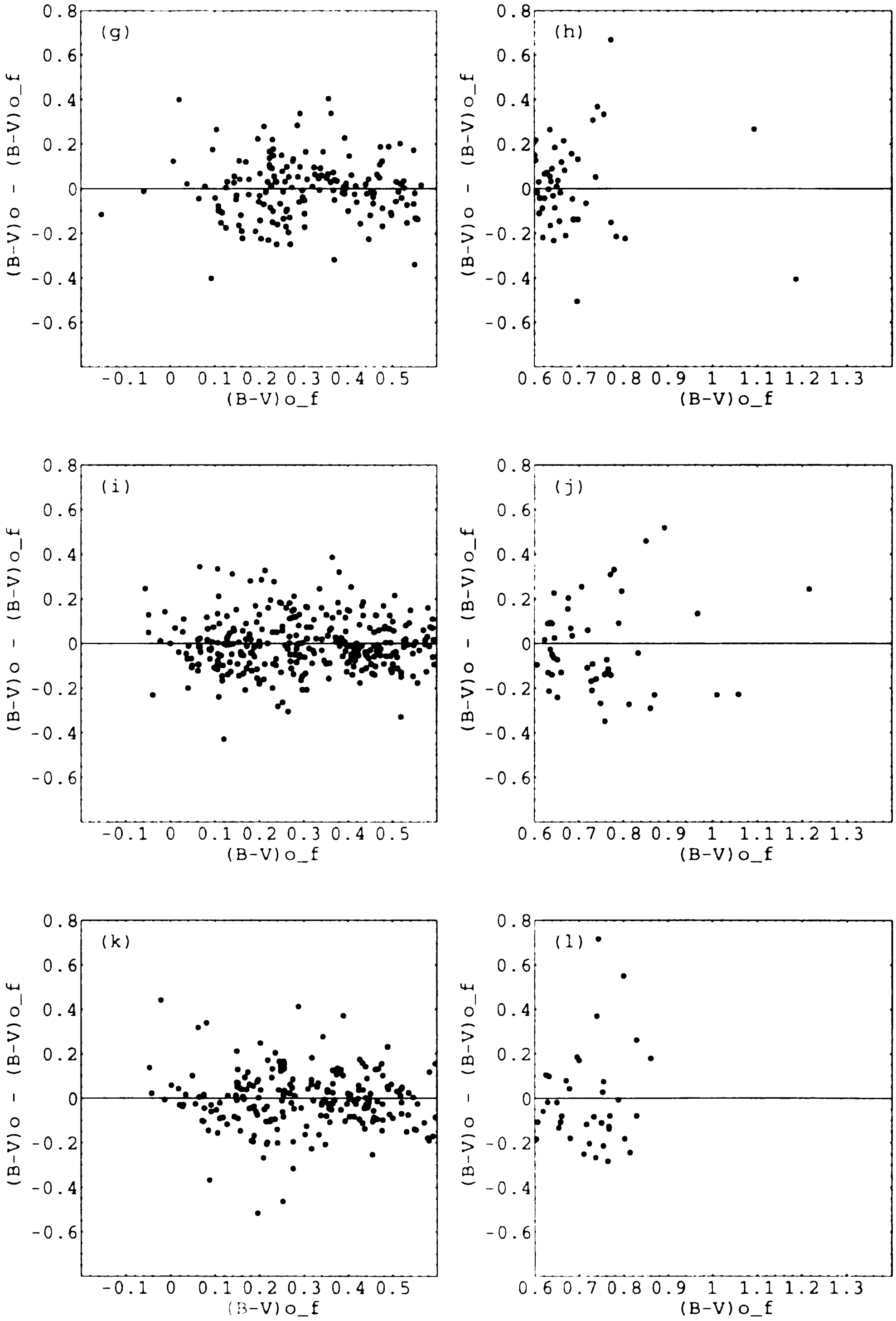

Figure 5.3 (continued)

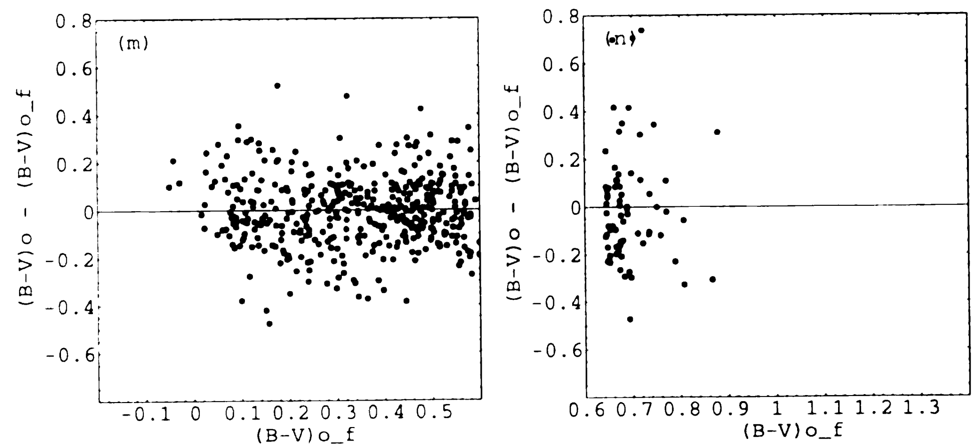

Figure 5.3 (continued)

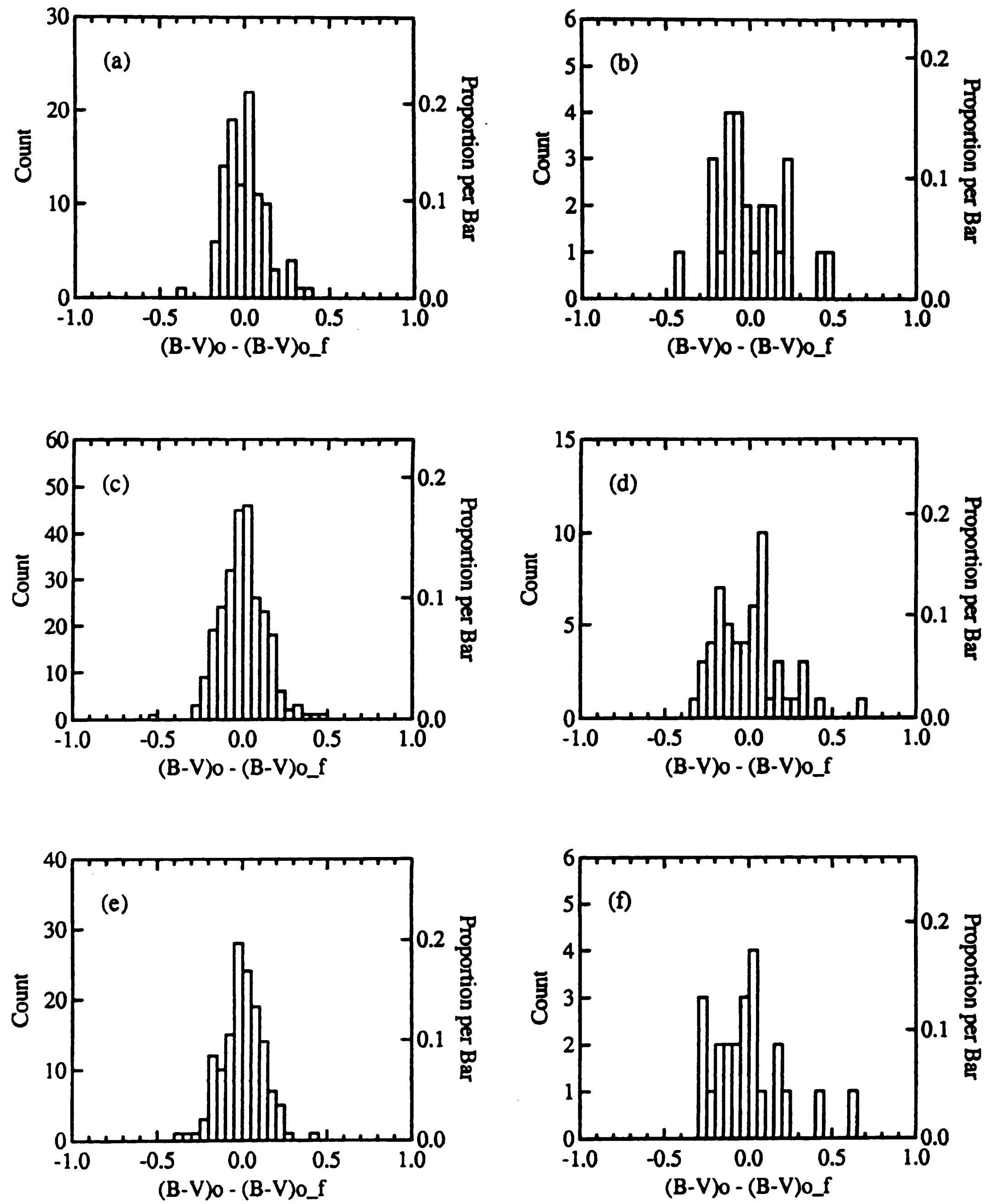

Figure 5.4 Histograms of the residuals for the groups, separated by temperature and availability of the SSS magnitude bands. Bins are 0.05 magnitude in width. The order of the panels are the sample as in Figure 5.3.

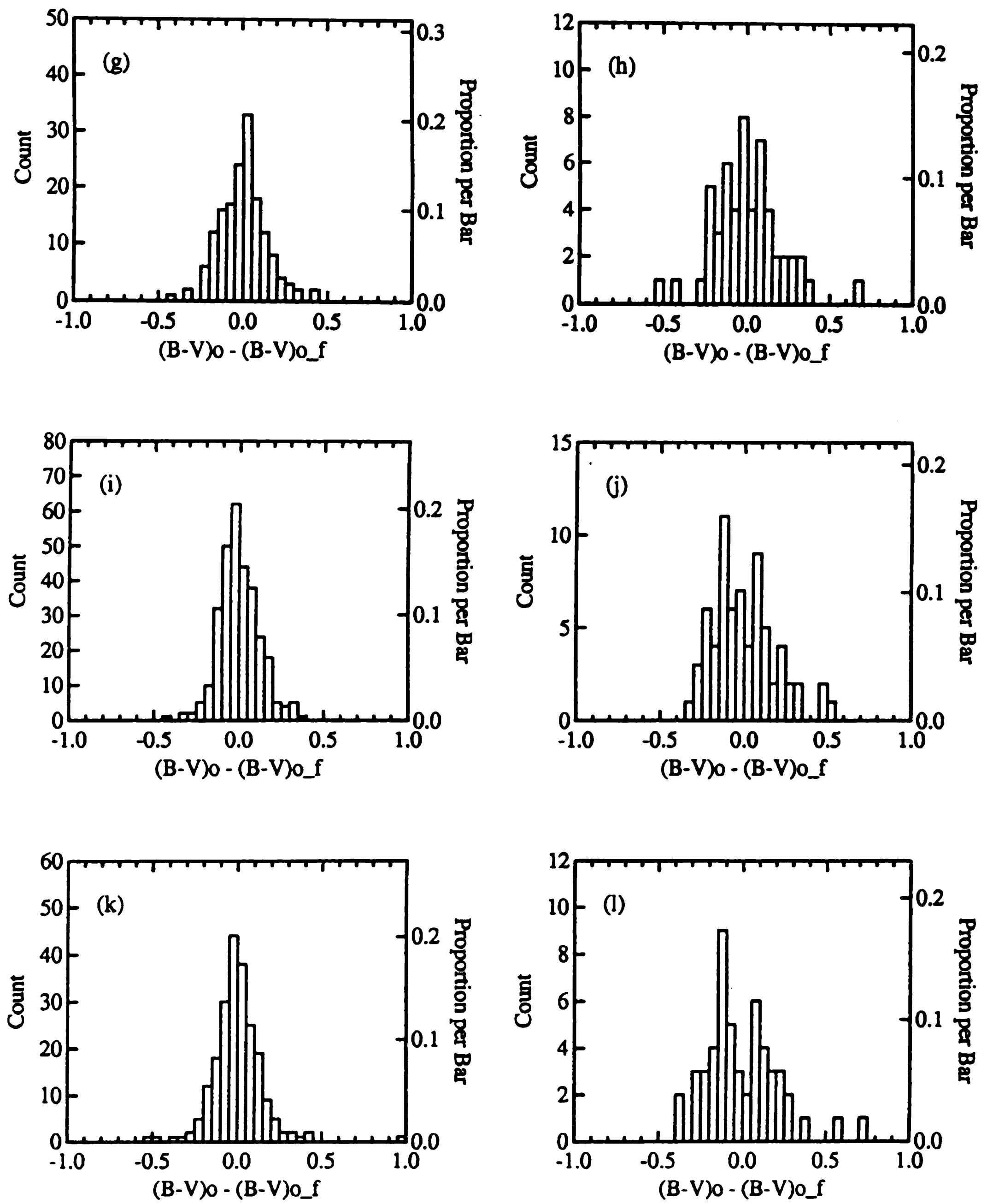

Figure 5.4 (continued)

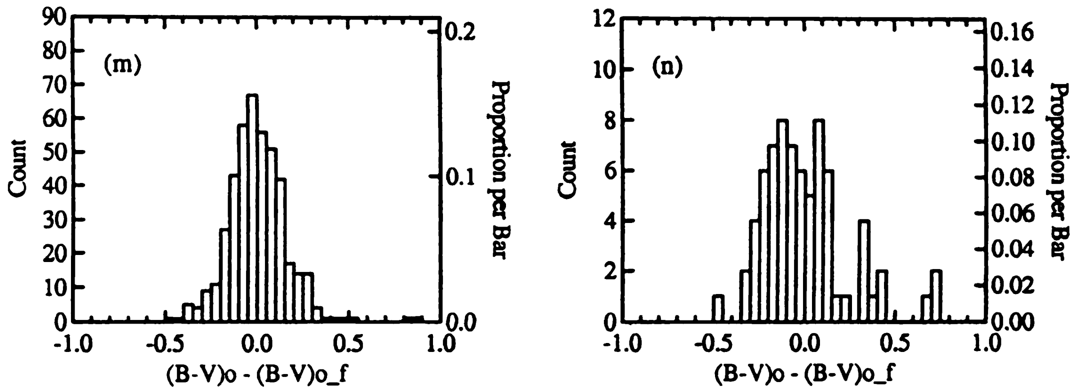

Figure 5.4 (continued)

identification of new candidates. First let us review the procedures for color calibration that were discussed in the previous section. By matching up the positional coordinates the K2 spectra are selected and then classified into 7 groups according to availability of various magnitude bands in the SSS. The trained networks for $(B-V)_0$ color calibration (bv-1.net to bv-7.net) feed on 200 continua fluxes, flux_m and the available SSS magnitudes to estimate $(B-V)_0$_p, and these are converted into $(B-V)_0$_f by making use of 14 fit functions. The procedures to produce K18_f and then to determine [Fe/H] and MP-class were already described in Section 4.3.

5.3.1 Seen Data

Matching up of the positional coordinates was performed among the samples in the known metal-deficient stars (HK1), digitally scanned stellar spectra (HK2), and the available magnitudes bands (SSS). Among those, 373 stars with observed $(B-V)_0$ colors were selected to be members in the validation set (seen data in this case), and most of them have been involved in the training process of the K18 calibration or $(B-V)_0$ calibration (or both). Three steps – color calibration, K18 calibration, and determination of metal abundance and MP-class – were accomplished for the 373 stars.

Figure 5.5 presents the relationships between the known [Fe/H] and predicted [Fe/H]_p estimated by mp-p.net with $(B-V)_0$_f and K18_f provided as inputs. The correlation coefficient and biweight estimator S_{BI} between [Fe/H] and [Fe/H]_p are 0.62 and 0.69 dex, respectively. As compared to the results with using *known* colors (Chapter 4), S_{BI} is increased by only about 0.1 dex and the c.c. is nearly identical. Even though only approximate colors and K18 indices are provided into mp-p.net, the results are still good. This is expected because these same stars have been

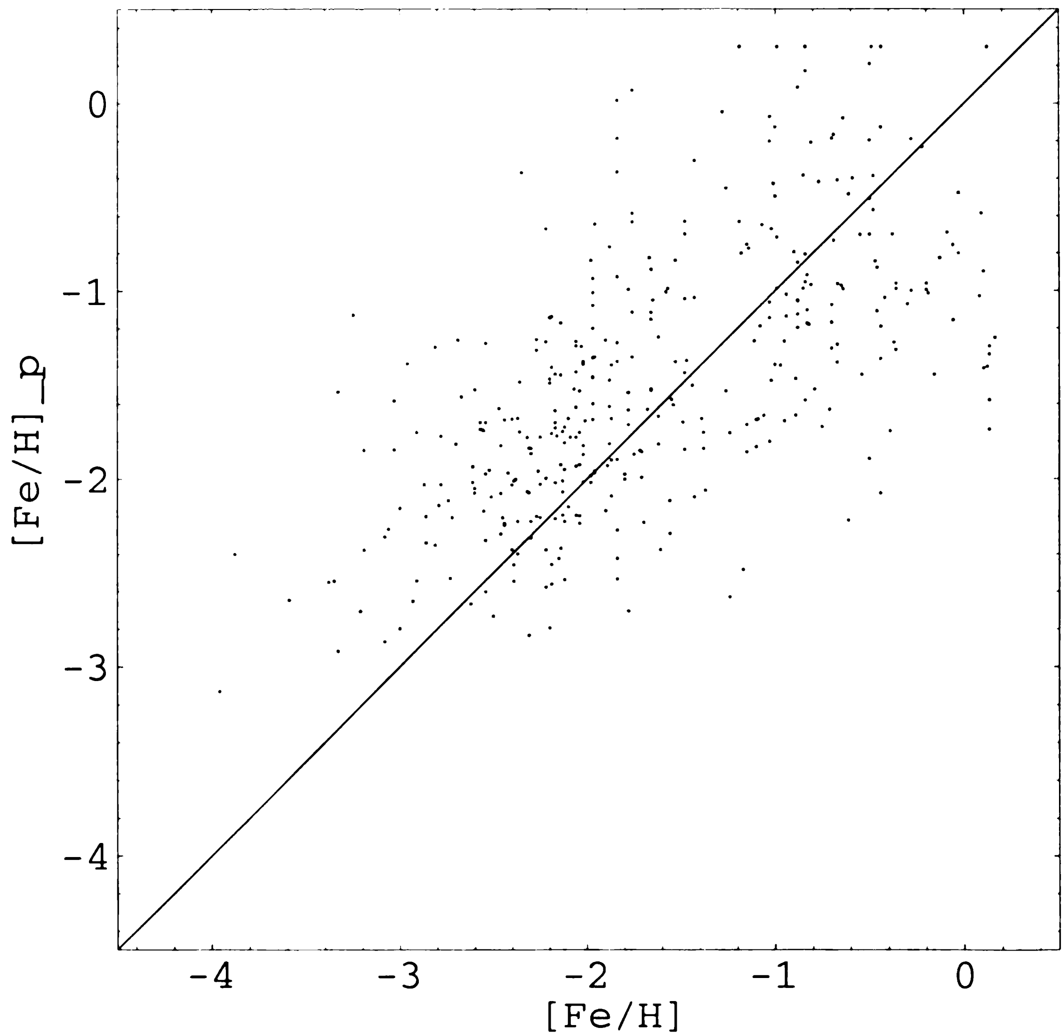

Figure 5.5 Predicted [Fe/H], as compared to known [Fe/H], for metal-poor stars in the "seen" data set. The metal abundance is estimated from the predicted colors and the calibrated K18_f index.

seen in the training process. As compared to Figure 4.6, the distributions in the region of higher metal abundance are improved (evenly distributed around the line of slope 1, while similar patterns occur for lower metal-abundance stars). Note that this can happen if mis-estimation of the colors compensates for the errors in the K18 indices. For example, K18_f can be underestimated in the hotter region, leading to a decreased [Fe/H] (downward in Figure 3.2), but if the star's color is underestimated (leftward = too blue) then the original [Fe/H] can be recovered. Actually, many stars are predicted to be bluer than 0.3, which is the limit of our target sample. Only one star is predicted to have metallicity less than [Fe/H] = –3.0, due to the K18 index saturation for hot stars and metallicity underestimation by mp-p.net for cooler stars. However, these effects are no so serious for stars in the cooler region. Statistical results for the seen hotter and cooler stars are displayed in Tables 5.5 and 5.6. In both cases, recovery and efficiency are still very good. Especially, the efficiency with cutoff [Fe/H] = –2.0 are good for the cooler stars, due to the same reasons discussed in Section 4.3.

Next, the mp-c.net fed on $(B\text{-}V)_0$_f and K18_f were used to determine the MP-class of stars in the seen data set. Table 5.7 shows the results of this application. Hotter metal-poor stars (MP-class 1) severely suffer from the saturation of K18 index near 2 Å. The correction rate (40.4%) for cooler metal-poor stars is definitely acceptable. The combined use of [Fe/H]_p and MP-class should increase the efficiency in the identification of the cooler metal-deficient stars.

Table 5.5 Recovery and Efficiency of Seen Hotter Stars ($(B-V)_0 \leq 0.50$)

Cutoff	[Fe/H]	[Fe/H]_p	Correct	Recovery (%)	Efficiency (%)
≤ -3.5	2	0	0	0.0	N/A
≤ -3.0	10	0	0	0.0	N/A
≤ -2.5	35	16	7	20.0	43.8
≤ **-2.0**	105	60	47	**44.8**	**78.3**
≤ -1.5	168	138	119	70.8	86.2
≤ -1.0	194	193	172	88.7	89.1
≤ -0.5	221	218	207	93.7	95.0
≤ 0.0	231	229	226	97.8	98.7
≤ +0.5	235	235	235	100.0	100.0
≤ +1.0	235	235	235	100.0	100.0

Table 5.6 Recovery and Efficiency of Seen Cooler Stars ($(B-V)_0 > 0.50$)

Cutoff	[Fe/H]	[Fe/H]_p	Correct	Recovery (%)	Efficiency (%)
≤ -3.5	1	0	0	0.0	N/A
≤ -3.0	8	1	1	12.5	100.0
≤ -2.5	20	7	7	35.0	100.0
≤ **-2.0**	47	30	26	**55.3**	**86.7**
≤ -1.5	58	58	45	77.6	77.6
≤ -1.0	79	91	66	83.5	72.5
≤ -0.5	109	118	94	86.2	79.7
≤ 0.0	131	133	126	96.2	94.7
≤ +0.5	138	138	138	100.0	100.0
≤ +1.0	138	138	138	100.0	100.0

Table 5.7 Classification Result of Seen Sets

	Overall	MP-class 1	MP-class 2	MP-class 3	MP-class 4	MP-class 5	MP-class 6
Correction Rate (%)	38.87	26.7	40.4	51.7	43.8	51.2	28.8
Number	373	105	47	89	32	41	59

5.3.2 Unseen Data

Among the stars which were collected by matching up the positional coordinates for the samples in the known metal-deficient stars (HK1), digitally scanned stellar spectra (HK2) and various magnitude bands (SSS), 199 stars were selected to be members in the validation set, all of them having never been involved in the training process of the K18 and $(B-V)_0$ calibrations. This data set should provide us with more objective results than the seen data discussed in the previous subsection. Three steps – color calibration, K18 calibration, and determination of metal abundance and MP-class – were performed for the 199 stars in the same way as described above.

Figure 5.6 shows the relationship between known [Fe/H] and predicted [Fe/H]_p estimated by mp-p.net with $(B-V)_0$_f and K18_f as inputs. The correlation coefficient and biweight estimator S_{BI} between [Fe/H] and [Fe/H]_p are 0.38 and 0.78 dex, respectively. Because of the wider spread in the distribution, the linear correlation coefficient is fairly low. However, S_{BI} increases about 0.2 dex only, as compared to the results shown in Chapter 4. Note that for the original HK survey, based on the visual selection of candidates, the EY of stars with [Fe/H] < –2.0 was just 11% without previous B-V color information. As shown in Tables 5.8 and 5.9, the efficiency for both hotter and cooler stars without any prior color and equivalent width information is about 57% at the cutoff [Fe/H] < –2.0. This is a *greatly* improved result. The recovery is not so good in that region, but better results are obtained if we consider stars with cutoff at [Fe/H] < –1.5. It is possible that the efficiency for cooler stars might be improved if our sample had more of the most metal-deficient stars with [Fe/H] < –2.0 (the current sample contains only 17 stars, which does not offer

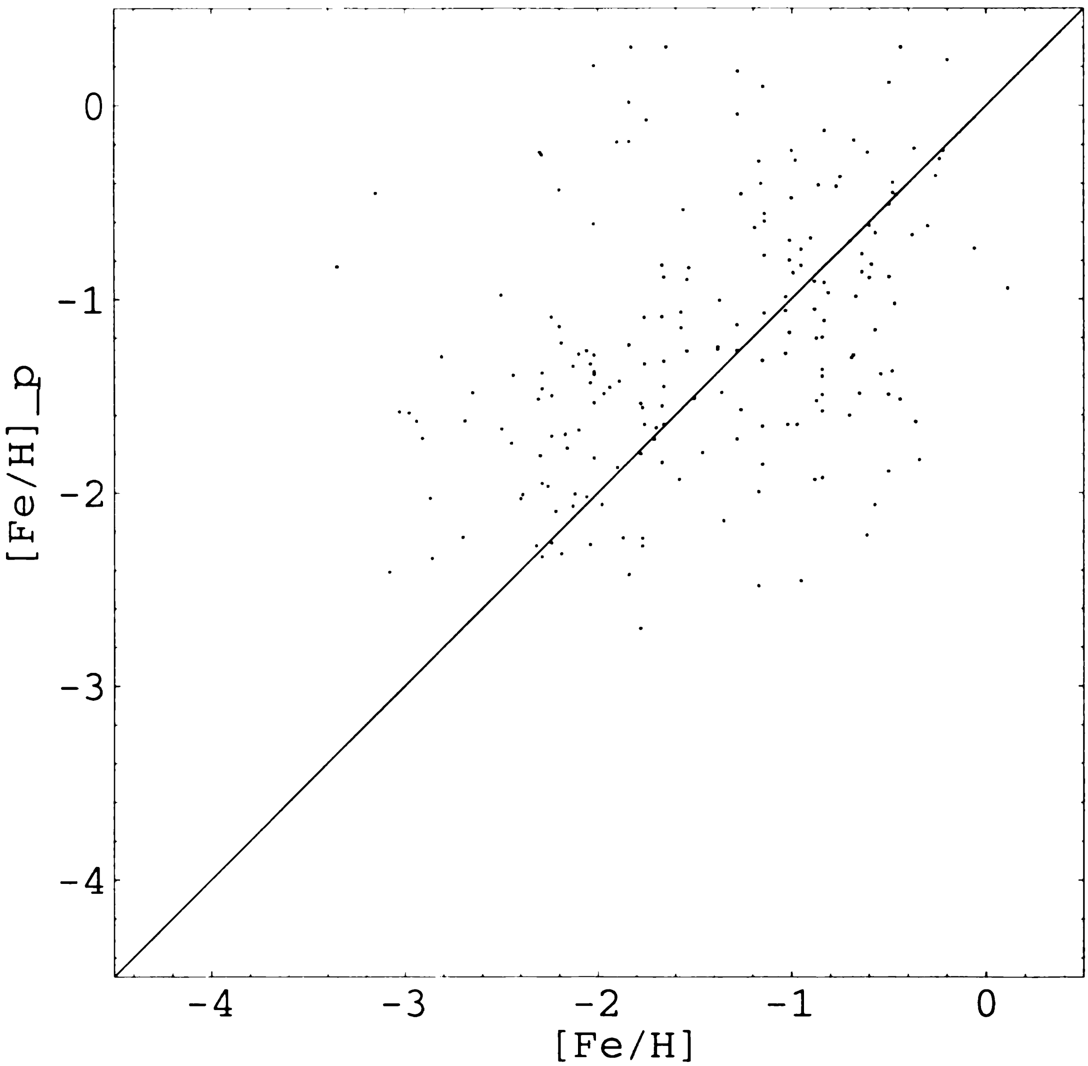

Figure 5.6 Predicted [Fe/H], compared to known [Fe/H], for metal-poor stars in the "unseen" data set. The metal abundance is estimated from predicted colors and the calibrated K18_f index.

appropriate statistics). This will be feasible in the near future, when the region of calibrated photographic magnitudes from the SSS expands to regions north of Galactic lattitude b = –60.

Once again, the mp-c.net fed on $(B\text{-}V)_0$_f and K18_f was used to determine the MP-class for stars in the unseen data set. The results of this application are shown in Table 5.10. For both the hot and cool stars, the correction rates for extremely metal-poor stars (MP-class 1 & 2) are too low, but one should keep in mind that the number of stars in each bin is not sufficient to give good statistical results at present.

Table 5.8 Recovery and Efficiency of Unseen Hotter Stars ($(B-V)_0 \leq 0.50$)

Cutoff	[Fe/H]	[Fe/H]_p	Correct	Recovery (%)	Efficiency (%)
≤ -3.5	0	0	0	N/A	N/A
≤ -3.0	2	0	0	0.0	N/A
≤ -2.5	11	1	0	0.0	0.0
≤ **-2.0**	40	19	11	**27.5**	**57.9**
≤ -1.5	71	46	36	50.7	78.3
≤ -1.0	93	83	71	76.3	85.5
≤ -0.5	119	107	104	87.4	97.2
≤ 0.0	127	123	122	96.1	99.2
≤ +0.5	128	128	128	100.0	100.0
≤ +1.0	128	128	128	100.0	100.0

Table 5.9 Recovery and Efficiency of Unseen Cooler Stars ($(B-V)_0 > 0.50$)

Cutoff	[Fe/H]	[Fe/H]_p	Correct	Recovery (%)	Efficiency (%)
≤ -3.5	0	0	0	N/A	N/A
≤ -3.0	2	0	0	0.0	N/A
≤ -2.5	4	0	0	0.0	N/A
≤ **-2.0**	17	7	4	**23.5**	**57.1**
≤ -1.5	27	26	14	51.9	53.8
≤ -1.0	40	44	28	70.0	63.6
≤ -0.5	62	56	50	80.6	89.3
≤ 0.0	71	67	67	94.4	100.0
≤ +0.5	71	71	71	100.0	100.0
≤ +1.0	71	71	71	100.0	100.0

Table 5.10 Classification Result of Unseen Sets

	Overall	MP-class 1	MP-class 2	MP-class 3	MP-class 4	MP-class 5	MP-class 6
Correction Rate (%)	40.20	15	11.8	49.1	52.2	65.7	35.5
Number	199	40	17	53	23	35	31

5.3.3 Future Improvements

In order to improve the results for prediction and classification, one more step to re-calibrate color and equivalent width will be necessary. The measured H18_2 index from the extracted spectra provides us with temperature information since, at least for hotter stars, the Balmer line dominates over the Ca II H line. This information has not been made use of at present. The reliability of $(B\text{-}V)_0$_f can be figured out as a function of H18_2. For example, if the trained network produces $(B\text{-}V)_0$_f of 0.2 (hot) but the strength of H18_2 is not so large (not so hot), then we should re-determine color of the stars. In addition, the problem with saturation of K18_f near 2 Å should be resolved. One of the possible solutions is to consider the measured K18_2 with K18_f simultaneously. For example, if K18_f is saturated at 2 Å and K18_2 is measured to 1 Å, then it would be reasonable to take 1 Å as the best estimate of K18. These efforts for improvement with re-calibration of color and equivalent widths will be carried out in the near future.

Chapter 6

NEW CANDIDATE METAL-POOR STARS

6.1 Methodology

In this chapter new candidate metal-poor stars are identified from the APM digital spectra and the multiple-band SSS magnitudes by application of the ANN methods described previously.

The entire procedures for this selection are summarized with a flowchart in Figure 6.1. First, the semi-automatic data reduction for the digitally scanned stellar spectra in the HK survey (HK2) is performed. By this procedure, the spectra are classified into useful and unusable ones, the positions of Ca II H and K lines are detected for useful spectra, their continua are constructed, and measurements of the equivalent widths (over bands of width ~ 18 Å) of the Ca II H and K lines, H18_2 and K18_2, are obtained.

By matching up the positional coordinates for the useful HK2 spectra and stars with available apparent magnitudes in the SSS, the sample to be involved in the selection process is collected. The stars in this sample are distributed into seven groups according to the available SSS magnitude bands. In each group, the trained networks bv-1.net to bv-7.net, which produce the best result for unseen data in the color calibration, feed on 200 flux estimates in the continua, the maximum flux level, flux_m, and available SSS magnitudes, in order to predict colors, $(B-V)_0$_p. The fit colors, $(B-V)_0$_f, are obtained by the use of 14 piecewise linear fitting functions.

Once the color calibration is finished, all stars are combined together once again. By consideration of their flux_m, the stars are then divided into three groups.

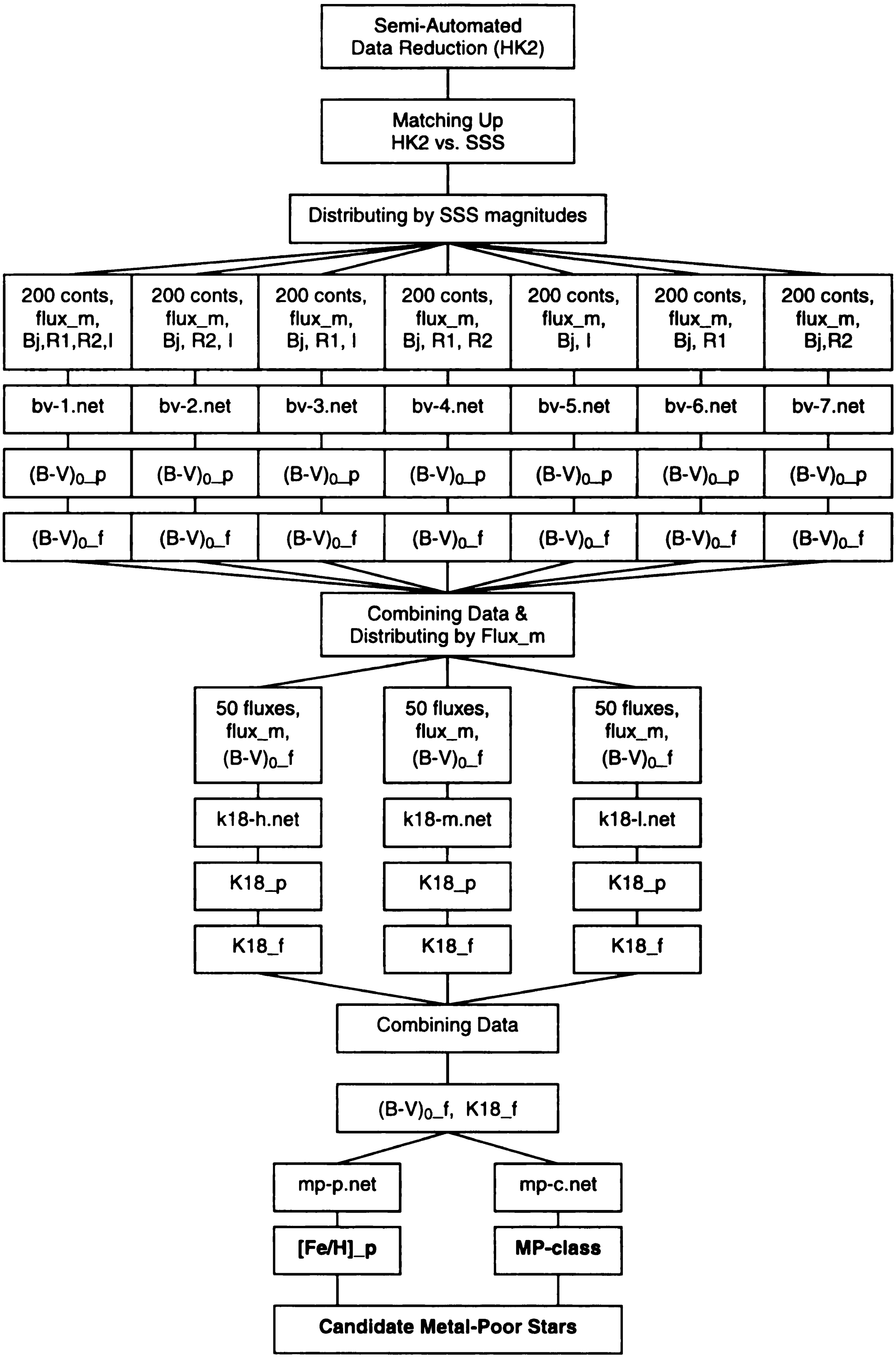

Figure 6.1 Flowchart of the selection procedure for candidate metal-poor stars.

In each group, the K18 index calibration is performed by providing 50 flux measurements around the Ca II K line, flux_m, and $(B\text{-}V)_0$_f into the trained networks k18-h.net, k18-m.net, and k18-l.net, the networks which produce the best results based on the validation sets. The predicted index, K18_p, is estimated by these networks. Then, K18_p is converted into K18_f making use of six piecewise linear fitting functions.

All stars with estimated $(B\text{-}V)_0$_f and K18_f are then joined together to participate in the final process. The quantities $(B\text{-}V)_0$_f and K18_f, are used as input variables into mp-p.net and mp-c.net, the networks which exhibited the best performance in the prediction and classification, respectively. The networks predict metallicity, [Fe/H], for all stars in the sample, and determine the MP-class, based on both the metal abundance and color (temperature).

Finally, a set of extremely metal-deficient star candidates is made according to [Fe/H]_p and MP-class. Future spectroscopic observations for these candidates should be obtained in order to assemble a new set of what should be a much more more objectively chosen and unbiased set of metal-poor stars in the Galaxy than were possible to assemble from the visually selected HK survey (HK1), in particular, amongst the cooler metal-poor stars. With these efforts, at least 28% of all extremely metal-poor stars in the observed region of the Galactic halo (in the magnitude range ($11.5 < B < 15$, the rough limits set by saturation and noise considerations) are expected to be detected with observing efficiency of 58% (Table 5.8). These very old stars will provide us with a much deeper understanding of the formation and evolution of the Galaxy.

6.2 New Candidate Metal-Poor Stars

We report 481 extremely metal-deficient star candidates ([Fe/H] < –2.0) in 10 plates of the HK survey, selected by employing the previously described methodology. Figure 6.2 presents the representative spectra of the candidate metal-poor stars with higher-, medium-, and lower-flux respectively. As explained in Chapter 2, the spectrum for higher flux is smooth and saturation occurs in right portion of Ca II H line, while the spectrum is noisy for lower flux. Among 30 known extremely metal-poor stars found together in 10 plates, 9 stars were correctly predicted below the cutoff (–2.0) – similar recovery rate of 30% as in Chapter 5. This result is quite encouraging. Table 6.1 shows the stars with their coordinates in the Besselian (equinox 1950.0) equatorial system. The 5th and 6th columns present measured equivalent widths for the Ca II H and K lines (H18_2 and K18_2) that will be used in a re-calibration of the color and equivalent widths to improve the selection results. The predicted quantities – K18_f, color $(B\text{-}V)_0$_f, [Fe/H]_p and MP-class – are listed in the 7th and 8th columns, and the last two columns. The 9th column, the flux class, provides us with rough apparent brightness information.

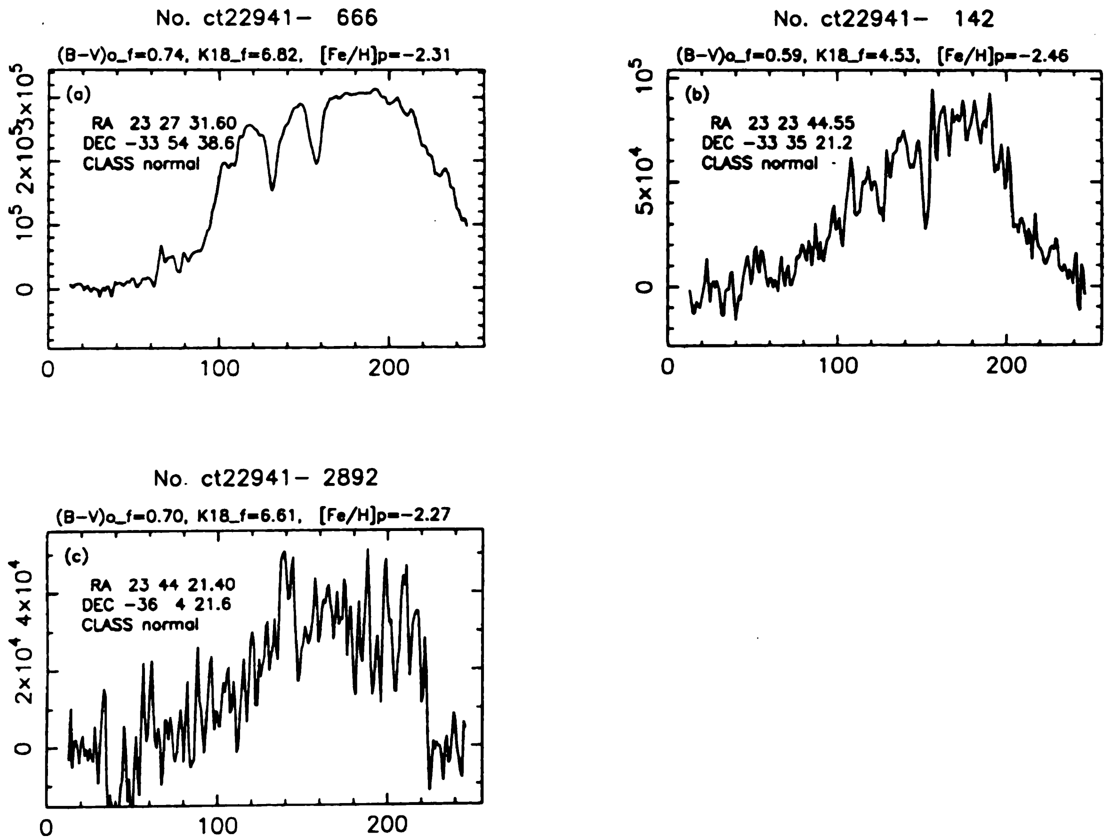

Figure 6.2 Representative spectra of metal-poor candidates exhibiting (a) high flux, (b) medium flux, and (c) low flux.

Table 6.1 New Extremely Metal-Poor Star Candidates with [Fe/H] < -2.0

Plate	HK2	RA (B1950)	DEC	H18_2	K18_2	K18_f	BV0_f	Flux-class	[Fe/H]_p	MP-class
22875	13	22 15 17.48	-42 -13 -55.80	3.848	6.331	7.773	0.805	2	-2.08	2
22875	31	22 15 23.87	-38 -42 -57.80	4.804	4.940	5.982	0.634	1	-2.26	2
22875	159	22 16 14.86	-41 -10 -32.50	6.352	3.728	5.346	0.602	1	-2.31	2
22875	227	22 16 37.95	-42 -39 -47.30	9.271	10.661	9.018	1.228	3	-2.12	4
22875	282	22 16 56.65	-38 -58 -21.00	6.220	6.317	6.832	0.663	1	-2.08	4
22875	478	22 18 12.08	-39 -13 -32.30	5.988	6.531	8.121	0.965	1	-2.22	2
22875	509	22 18 21.16	-41 -26 -9.50	3.399	4.707	5.617	0.569	1	-2.11	2
22875	620	22 19 3.09	-40 -40 -3.60	5.386	4.116	5.637	0.635	1	-2.35	2
22875	623	22 19 3.98	-40 -40 -19.40	5.371	4.163	5.407	0.646	1	-2.44	2
22875	702	22 19 38.48	-41 -39 -38.60	3.582	4.334	7.543	0.898	1	-2.37	2
22875	858	22 20 46.77	-38 -11 -0.40	3.043	4.461	8.475	0.946	1	-2.01	2
22875	1100	22 22 32.87	-40 -59 -55.80	5.497	1.863	3.684	0.626	1	-2.73	2
22875	1155	22 23 0.49	-38 -44 -36.40	3.284	2.465	2.527	0.400	1	-2.20	1
22875	1415	22 24 43.84	-42 -32 -46.70	7.742	4.596	6.291	0.610	2	-2.07	4
22875	1520	22 25 36.31	-41 -59 -25.10	4.279	-0.033	1.833	0.328	1	-2.08	1
22875	1615	22 26 19.74	-38 -23 -27.00	4.626	3.825	5.615	0.598	1	-2.23	2
22875	1788	22 27 42.10	-38 -20 -20.60	4.789	5.311	6.892	0.696	1	-2.16	2
22875	1859	22 28 9.31	-38 -40 -10.90	3.727	5.696	7.848	0.827	1	-2.09	2
22875	1871	22 28 14.63	-42 -10 -48.70	1.704	2.773	6.569	0.667	1	-2.18	2
22875	1944	22 28 46.89	-40 -46 -29.60	4.452	7.534	7.570	0.823	1	-2.21	2
22875	2063	22 29 39.49	-38 -53 -58.90	5.964	3.745	5.355	0.692	1	-2.58	2
22875	2063	22 29 39.49	-38 -53 -58.90	5.964	3.745	4.458	0.481	1	-2.01	3
22875	2116	22 29 57.56	-38 -18 -3.50	4.933	7.030	7.055	0.666	1	-2.00	4
22875	2199	22 30 28.06	-39 -7 -21.60	6.647	2.694	6.168	0.647	1	-2.25	2
22875	2246	22 30 43.16	-42 -14 -36.00	2.041	2.845	7.130	0.923	1	-2.56	2

Table 6.1 (continued)

Plate	HK2	RA	(B1950)		DEC			H18_2	K18_2	K18_f	BV0_f	Flux-class	[Fe/H]_p	MP-class
22875	2726	22	33	46.51	-41	-47	-39.40	2.804	2.844	3.491	0.550	1	-2.56	2
22875	2730	22	33	48.77	-38	-33	-43.80	2.869	2.315	3.317	0.441	1	-2.13	1
22875	2769	22	34	4.10	-40	-59	-32.30	4.504	3.462	4.095	0.564	1	-2.46	2
22875	2801	22	34	17.46	-41	-49	-59.20	4.219	3.709	4.322	0.508	1	-2.18	2
22875	3029	22	35	59.10	-37	-56	-37.00	2.668	4.867	7.797	0.888	1	-2.24	2
22875	3030	22	35	59.19	-37	-56	-49.70	2.722	4.997	7.756	0.888	1	-2.26	2
22875	3208	22	37	18.86	-37	-54	-5.00	5.282	6.550	8.757	1.168	1	-2.19	4
22875	3355	22	38	17.62	-38	-1	-47.80	9.654	6.594	7.830	0.891	3	-2.23	2
22875	3379	22	38	26.06	-42	-38	-31.40	2.280	3.466	7.270	0.977	1	-2.59	2
22875	3473	22	38	59.73	-42	-17	-28.90	2.468	3.668	7.902	0.832	1	-2.08	2
22875	3480	22	39	3.83	-40	-12	-12.70	2.383	3.587	6.957	0.656	1	-2.00	4
22875	3566	22	39	38.60	-41	-43	-16.00	2.047	3.564	7.885	0.823	1	-2.07	2
22875	3591	22	39	51.80	-38	-5	-6.00	4.024	15.419	8.704	1.125	3	-2.16	4
22875	3600	22	39	53.86	-38	-23	-48.50	7.119	7.495	8.415	0.922	2	-2.00	2
22875	3634	22	40	8.31	-40	-38	-16.10	4.210	5.139	5.704	0.607	1	-2.24	2
22875	3676	22	40	24.03	-41	-48	-20.70	2.076	3.185	8.249	1.056	1	-2.30	2
22875	3694	22	40	30.50	-42	-21	-17.30	9.655	11.381	9.231	1.291	3	-2.07	4
22881	242	22	16	16.06	-40	-47	-5.10	1.890	2.836	4.359	0.488	1	-2.07	3
22881	255	22	15	47.19	-40	-2	-42.90	6.890	4.198	7.438	0.725	1	-2.02	4
22881	468	22	15	8.66	-41	-11	-25.90	4.032	4.332	4.093	0.495	1	-2.18	2
22881	567	22	13	28.16	-38	-45	-8.40	5.831	2.797	3.764	0.450	1	-2.04	3
22881	664	22	13	58.25	-40	-43	-21.10	6.314	4.520	2.889	0.471	2	-2.42	1
22881	770	22	12	1.34	-37	-53	-24.00	6.523	4.348	5.250	0.627	1	-2.42	2
22881	844	22	12	18.61	-39	-23	-23.90	2.405	4.024	6.975	0.764	1	-2.31	2
22881	853	22	12	27.95	-39	-49	-45.30	4.906	6.334	8.112	0.867	1	-2.05	2

Table 6.1 (continued)

Plate	HK2	RA (B1950)	DEC	H18_2	K18_2	K18_f	BV0_f	Flux-class	[Fe/H]_p	MP-class
22881	1024	22 12 20.45	-41 -15 -28.10	6.391	3.302	3.985	0.502	2	-2.24	2
22881	1087	22 11 32.23	-40 -15 -31.10	5.385	3.559	2.901	0.666	1	-2.97	2
22881	1127	22 12 1.20	-41 -45 -23.00	2.458	3.850	6.408	0.668	1	-2.24	2
22881	1228	22 10 45.95	-40 -17 -49.10	2.185	3.740	6.921	0.708	1	-2.18	2
22881	1436	22 9 51.37	-40 -50 -11.50	3.783	1.439	2.600	0.403	1	-2.18	1
22881	1463	22 8 26.70	-38 -7 -59.20	2.478	3.781	5.983	0.571	1	-2.01	4
22881	1518	22 8 44.53	-39 -40 -3.10	4.494	2.659	3.432	0.425	1	-2.00	3
22881	1596	22 9 25.70	-42 -6 -43.00	4.173	3.782	5.465	0.538	1	-2.01	4
22881	1657	22 8 50.51	-41 -32 -24.00	5.977	3.928	3.042	0.433	1	-2.18	1
22881	1726	22 7 50.23	-40 -1 -49.40	4.306	4.908	5.316	0.527	1	-2.00	4
22881	1863	22 6 28.22	-38 -23 -5.70	4.654	5.412	6.869	0.693	1	-2.16	2
22881	1907	22 7 45.06	-42 -12 -57.20	4.747	5.502	7.747	0.854	1	-2.20	2
22881	1910	22 6 33.34	-39 -21 -57.20	2.976	5.130	7.885	0.798	1	-2.01	2
22881	2079	22 5 34.29	-39 -17 -24.80	1.601	2.183	4.912	0.533	1	-2.14	2
22881	2108	22 5 32.99	-39 -51 -54.40	4.925	6.192	6.168	0.671	1	-2.32	2
22881	2170	22 4 49.72	-38 -59 -59.30	2.453	4.075	7.538	0.860	1	-2.30	2
22881	2579	22 3 11.23	-40 -3 -5.80	6.765	5.034	7.358	0.757	1	-2.15	2
22881	2597	22 2 37.07	-38 -39 -20.30	4.028	5.706	7.718	0.876	1	-2.25	2
22881	2670	22 3 7.31	-41 -15 -36.60	5.378	0.651	2.115	0.363	2	-2.16	1
22881	2675	22 2 27.21	-39 -26 -9.90	3.421	2.882	2.893	0.430	1	-2.22	1
22881	2680	22 2 56.38	-40 -54 -23.90	8.298	8.364	8.517	0.989	2	-2.06	2
22881	2777	22 2 49.68	-42 0 -23.50	3.651	1.092	3.910	0.690	1	-2.83	2
22881	2792	22 1 29.91	-38 -18 -17.70	2.145	3.735	6.491	0.690	1	-2.28	2
22881	2794	22 1 29.19	-38 -18 -32.40	2.198	3.776	6.361	0.671	1	-2.26	2
22881	2821	22 2 7.02	-40 -38 -54.40	4.461	5.990	8.086	0.933	1	-2.19	2

Table 6.1 (continued)

Plate	HK2	RA	(B1950)		DEC			H18_2	K18_2	K18_f	BV0_f	Flux-class	[Fe/H]_p	MP-class
22881	2828	22	1	19.20	-38	-18	-14.80	4.858	5.101	4.955	0.567	2	-2.28	2
22881	3105	22	0	36.22	-41	-2	-52.40	7.585	4.772	6.530	0.625	1	-2.05	4
22881	3366	21	59	12.87	-41	-19	-53.70	3.688	4.056	4.969	0.646	2	-2.54	2
22881	3375	21	58	33.05	-39	-7	-47.40	7.354	6.580	7.125	0.674	1	-2.00	4
22881	3377	21	58	43.12	-39	-45	-57.60	9.526	6.962	7.263	0.711	1	-2.06	4
22881	3576	21	57	30.65	-38	-51	-48.50	1.901	2.836	5.506	0.612	1	-2.31	2
22881	3595	21	58	7.60	-41	-29	-44.00	4.953	2.000	2.236	0.383	1	-2.23	1
22881	3701	21	57	10.66	-40	-3	-0.10	1.919	3.682	6.580	0.637	1	-2.08	4
22881	3750	21	56	49.33	-39	-58	-34.60	2.035	3.010	6.628	0.697	1	-2.26	2
22881	3873	21	56	11.41	-39	-51	-27.60	3.893	4.796	6.232	0.600	1	-2.05	4
22881	3892	21	55	47.64	-38	-32	-0.50	3.649	5.171	6.370	0.644	1	-2.17	2
22881	3919	21	55	39.27	-38	-33	-23.20	2.397	3.680	6.618	0.670	1	-2.18	2
22881	3921	21	56	11.30	-40	-47	-36.50	5.229	5.400	4.260	0.486	1	-2.09	3
22881	3996	21	55	40.82	-40	-8	-30.20	2.677	4.529	7.012	0.681	1	-2.07	4
22881	4038	21	55	32.47	-40	-25	-26.30	4.711	5.912	7.514	0.749	1	-2.06	2
22881	4118	21	55	24.39	-41	-25	-51.10	1.992	3.346	5.831	0.586	1	-2.12	4
22881	4133	21	54	39.76	-38	-33	-48.90	2.181	3.578	7.928	1.183	1	-2.59	4
22881	4259	21	54	2.98	-38	-29	-5.20	4.528	6.563	3.895	0.466	2	-2.09	1
22881	4483	21	53	13.83	-40	-22	-43.60	3.459	3.236	5.477	0.607	1	-2.30	2
22888	291	23	0	17.35	-35	-43	-29.70	3.790	1.209	2.336	0.369	1	-2.09	1
22888	655	23	3	8.20	-37	-35	-4.90	6.654	5.524	6.549	0.738	1	-2.39	2
22888	743	23	2	58.76	-34	-38	-26.70	3.392	3.878	5.753	0.672	1	-2.43	2
22888	1070	23	5	25.00	-35	-53	-25.10	2.555	4.087	7.827	0.889	1	-2.23	2
22888	1176	23	6	16.41	-36	-11	-51.50	7.196	2.947	3.327	0.590	1	-2.71	2
22888	1517	23	8	5.77	-34	-39	-2.80	6.006	4.821	8.120	0.936	2	-2.18	2

Table 6.1 (continued)

Plate	HK2	RA (B1950)	DEC	H18_2	K18_2	K18_f	BV0_f	Flux-class	[Fe/H]_p	MP-class
22888	1556	23 8 2.60	-33 -48 -49.50	2.746	0.055	3.199	0.525	1	-2.54	2
22888	2004	23 11 21.28	-34 -30 -14.80	5.766	5.904	8.327	0.935	1	-2.07	2
22888	2190	23 13 32.01	-36 -47 -27.80	4.946	6.098	6.446	0.634	1	-2.11	4
22888	2432	23 15 29.59	-36 -40 -12.90	2.243	3.722	6.495	0.647	1	-2.14	2
22888	3015	23 19 59.05	-36 -19 -8.90	3.118	4.529	7.503	0.803	1	-2.20	2
22888	3040	23 18 57.78	-33 -46 -56.80	5.941	7.411	8.222	0.980	1	-2.20	2
22888	3249	23 21 27.38	-35 -58 -59.80	4.384	6.431	7.876	0.802	1	-2.02	2
22888	3279	23 21 4.45	-34 -52 -41.90	2.301	3.529	7.325	0.876	1	-2.41	2
22888	3348	23 21 4.12	-33 -49 -35.30	6.039	3.546	4.236	0.500	1	-2.16	2
22941	19	23 22 51.40	-36 -37 -22.50	2.872	4.282	8.274	0.969	1	-2.16	2
22941	142	23 23 44.55	-33 -35 -21.20	4.993	3.841	4.533	0.591	2	-2.46	2
22941	188	23 24 0.47	-36 -13 -3.10	6.043	5.501	6.377	0.602	1	-2.01	4
22941	271	23 24 36.31	-33 -58 -33.10	2.028	3.480	6.826	0.663	1	-2.08	4
22941	304	23 24 48.62	-35 -58 -30.80	2.983	3.659	6.255	0.621	1	-2.13	4
22941	384	23 25 19.68	-33 -18 -13.90	2.170	2.636	3.654	0.466	1	-2.16	1
22941	439	23 25 47.42	-35 -9 -51.00	2.707	4.193	5.735	0.579	1	-2.12	2
22941	466	23 26 0.64	-34 -46 -0.90	4.801	4.449	6.876	0.653	1	-2.02	4
22941	480	23 26 7.43	-37 -8 -6.80	4.540	3.390	4.780	0.582	1	-2.37	2
22941	666	23 27 31.60	-33 -54 -38.60	3.858	4.679	6.823	0.740	1	-2.31	2
22941	829	23 28 44.20	-33 -24 -1.40	6.378	5.956	5.979	0.594	1	-2.11	4
22941	939	23 29 38.23	-33 -7 -28.60	3.838	5.533	7.282	0.718	1	-2.07	2
22941	950	23 29 42.96	-36 -6 -13.40	2.553	3.842	5.739	0.564	1	-2.05	4
22941	1349	23 32 39.81	-35 -48 -48.80	6.324	6.704	7.311	0.841	1	-2.35	2
22941	1399	23 33 2.89	-33 -43 -25.40	7.823	4.542	3.641	0.469	1	-2.18	1
22941	1404	23 33 4.72	-33 -4 -12.20	3.647	3.151	3.764	0.648	1	-2.77	2

Table 6.1 (continued)

Plate	HK2	RA (B1950)	DEC	H18_2	K18_2	K18_f	BV0_f	Flux-class	[Fe/H]_p	MP-class
22941	1580	23 34 29.20	-33 -33 -31.90	3.678	5.043	7.131	0.684	1	-2.03	4
22941	1610	23 34 42.23	-34 -15 -39.30	2.268	3.441	7.122	0.704	1	-2.09	2
22941	1614	23 34 42.89	-33 -52 -58.50	3.313	4.335	8.218	0.985	1	-2.21	2
22941	1619	23 34 44.31	-33 -56 -45.60	4.306	5.694	8.505	0.963	1	-2.02	2
22941	1653	23 35 5.16	-36 -27 -19.20	4.550	5.843	7.984	0.901	1	-2.18	2
22941	1986	23 37 37.68	-33 -15 -22.20	2.901	3.907	6.121	0.607	1	-2.12	4
22941	2040	23 38 8.28	-34 -38 -42.40	3.008	5.073	8.408	0.992	1	-2.12	2
22941	2050	23 38 12.00	-34 -13 -54.20	4.060	3.160	5.422	0.843	1	-2.85	2
22941	2051	23 38 12.52	-34 -14 -27.30	3.859	3.493	3.493	0.484	1	-2.29	1
22941	2052	23 38 12.61	-35 -15 -17.70	3.856	5.079	5.864	0.564	1	-2.02	4
22941	2164	23 39 3.54	-36 -38 -56.40	2.256	3.749	6.576	0.629	1	-2.05	4
22941	2172	23 39 7.71	-36 -5 -17.40	4.795	6.220	6.012	0.571	1	-2.00	4
22941	2175	23 39 8.60	-35 -29 -41.30	2.786	3.807	7.790	0.870	1	-2.21	2
22941	2191	23 39 15.77	-32 -26 -20.20	2.736	3.793	6.972	0.675	1	-2.06	4
22941	2355	23 40 31.44	-32 -49 -49.20	3.052	4.216	7.708	0.957	1	-2.40	2
22941	2395	23 40 49.19	-35 -3 -36.90	6.853	5.860	6.943	0.891	1	-2.57	2
22941	2427	23 41 2.34	-36 -56 -9.90	2.044	3.200	6.838	0.696	1	-2.18	2
22941	2596	23 42 15.01	-32 -23 -9.00	2.269	3.028	7.041	0.799	1	-2.37	2
22941	2623	23 42 29.01	-35 -36 -50.60	2.269	3.054	3.321	0.449	1	-2.17	1
22941	2641	23 42 35.52	-36 -24 -5.10	6.154	6.488	6.320	0.616	1	-2.09	4
22941	2799	23 43 44.41	-34 -26 -59.80	4.961	2.704	2.560	0.520	1	-2.71	2
22941	2892	23 44 21.40	-36 -4 -21.60	5.188	6.328	6.610	0.701	3	-2.27	2
22941	2960	23 44 56.70	-35 -53 -56.80	2.522	3.832	7.075	0.709	1	-2.13	2
22941	3023	23 45 30.35	-36 -14 -37.40	4.054	2.934	7.209	0.735	2	-2.15	2
22941	3109	23 46 9.09	-36 -30 -22.70	2.414	4.058	7.894	0.901	1	-2.22	2

Table 6.1 (continued)

Plate	HK2	RA (B1950)	DEC	H18_2	K18_2	K18_f	BV0_f	Flux-class	[Fe/H]_p	MP-class
22941	3124	23 46 18.25	-34 -10 -32.30	5.086	6.109	7.133	0.693	1	-2.06	4
22953	22	0 58 44.37	-62 0 -17.20	3.301	3.982	7.456	0.779	1	-2.16	2
22953	75	0 59 31.66	-62 -21 -20.20	6.115	5.591	8.167	0.970	3	-2.21	2
22953	144	1 0 20.36	-58 -23 -0.50	5.575	7.075	9.239	1.348	1	-2.13	4
22953	149	1 0 24.22	-61 -41 -13.80	7.071	5.150	5.335	0.536	2	-2.04	4
22953	228	1 1 11.07	-61 -51 -43.10	5.511	3.802	4.459	0.676	1	-2.71	2
22953	387	1 2 53.04	-60 -35 -30.50	4.063	4.765	7.102	0.671	1	-2.00	4
22953	405	1 3 3.82	-57 -58 -38.00	5.326	4.604	8.302	0.910	2	-2.04	2
22953	408	1 3 4.31	-61 -5 -44.60	2.148	3.719	6.944	0.693	1	-2.13	2
22953	476	1 3 47.39	-62 -28 -36.40	5.206	3.798	4.277	0.502	1	-2.16	2
22953	489	1 3 56.00	-60 -53 -52.80	4.690	6.284	7.106	0.679	1	-2.02	4
22953	610	1 5 9.12	-61 -53 -13.90	3.454	3.289	4.898	0.538	1	-2.17	2
22953	808	1 6 44.48	-61 -1 -44.90	4.198	4.893	6.238	0.647	1	-2.22	2
22953	839	1 6 54.88	-58 -13 -6.20	4.554	4.029	6.273	0.591	1	-2.00	4
22953	896	1 7 23.62	-61 -18 -39.00	2.558	3.997	6.982	0.691	1	-2.11	2
22953	908	1 7 32.66	-59 -21 -8.50	5.061	5.469	6.311	0.643	1	-2.19	2
22953	931	1 7 42.88	-59 -23 -20.80	2.859	3.874	5.726	0.600	1	-2.21	2
22953	940	1 7 48.66	-61 -59 -23.10	2.064	2.804	5.435	0.548	1	-2.07	4
22953	974	1 8 11.27	-58 -7 -41.60	5.842	2.785	3.620	0.499	1	-2.33	1
22953	1018	1 8 35.64	-62 -17 -33.10	2.578	2.808	4.176	0.473	1	-2.04	3
22953	1042	1 8 46.12	-58 -50 -54.90	5.897	2.567	2.286	0.359	2	-2.05	1
22953	1075	1 9 9.12	-59 0 -49.60	4.715	2.780	2.649	0.465	2	-2.48	1
22953	1084	1 9 14.65	-62 -16 -9.70	3.249	3.201	5.535	0.576	1	-2.16	2
22953	1123	1 9 28.74	-62 -20 -3.20	7.580	6.277	5.766	0.558	1	-2.02	4
22953	1126	1 9 30.00	-59 -26 -43.50	3.631	1.754	2.238	0.353	1	-2.03	1

Table 6.1 (continued)

Plate	HK2	RA (B1950) DEC	H18_2	K18_2	K18_f	BV0_f	Flux-class	[Fe/H]_p	MP-class
22953	1150	1 9 45.76 -62 -24 -34.10	3.696	1.877	2.820	0.447	1	-2.33	1
22953	1162	1 9 52.96 -60 -36 -17.50	4.074	3.560	4.412	0.478	1	-2.00	3
22953	1302	1 11 18.25 -58 -45 -32.70	3.332	4.319	6.183	0.603	1	-2.08	4
22953	1324	1 11 27.08 -61 -55 -45.20	6.201	5.344	6.361	0.628	1	-2.12	4
22953	1383	1 11 59.16 -59 -38 -47.40	5.690	4.067	4.550	0.528	1	-2.21	2
22953	1419	1 12 14.58 -59 -46 -36.20	3.209	4.754	8.300	0.912	1	-2.04	2
22953	1438	1 12 29.98 -61 -30 -40.10	2.734	2.163	3.472	0.450	1	-2.13	1
22953	1574	1 14 0.05 -61 -45 -59.70	2.922	5.477	7.558	0.738	1	-2.01	4
22953	1608	1 14 18.68 -62 -2 -14.60	2.384	3.763	6.818	0.645	1	-2.02	4
22953	1684	1 15 9.00 -61 -30 -14.20	3.738	6.949	7.307	0.853	1	-2.38	2
22953	1728	1 15 34.11 -61 -11 -24.30	3.861	5.077	8.538	1.026	1	-2.11	2
22953	1730	1 15 34.88 -62 -29 -34.80	2.388	1.350	2.423	0.413	1	-2.32	1
22953	1833	1 16 28.88 -59 -4 -48.00	4.085	3.886	6.445	0.637	1	-2.12	4
22953	1838	1 16 29.91 -59 -4 -29.50	4.067	3.908	6.547	0.626	1	-2.05	4
22953	1839	1 16 30.35 -61 -22 -13.00	2.406	3.025	5.065	0.513	1	-2.00	3
22953	1868	1 16 50.55 -59 -25 -58.70	4.748	5.018	6.870	0.688	1	-2.14	2
22953	1870	1 16 52.15 -62 -2 -6.40	2.999	4.488	6.808	0.642	1	-2.01	4
22953	1892	1 17 3.25 -58 -2 -19.90	7.151	3.297	4.716	0.544	1	-2.24	2
22953	1942	1 17 35.28 -60 -8 -54.30	4.941	5.000	8.614	1.023	1	-2.06	2
22953	1949	1 17 38.76 -61 -52 -54.30	2.694	3.796	4.175	0.470	1	-2.03	3
22953	2008	1 18 6.13 -58 -40 -30.40	2.353	3.852	7.188	0.757	1	-2.21	2
22953	2023	1 18 12.78 -61 -31 -45.70	3.777	4.322	7.071	0.673	1	-2.02	4
22953	2061	1 18 33.82 -59 -16 -6.70	3.615	4.410	8.455	0.951	1	-2.03	2
22953	2099	1 18 57.14 -61 -40 -50.80	6.740	6.927	6.484	0.610	1	-2.01	4
22953	2120	1 19 13.60 -62 -23 -42.70	2.814	3.832	6.431	0.667	1	-2.23	2

Table 6.1 (continued)

Plate	HK2	RA (B1950)	DEC	H18_2	K18_2	K18_f	BV0_f	Flux-class	[Fe/H]_p	MP-class
22953	2165	1 19 42.90	-58 -16 -15.90	5.127	4.139	6.276	0.658	1	-2.25	2
22953	2314	1 21 25.92	-62 -7 -12.00	4.718	5.728	7.451	0.775	1	-2.15	2
22953	2332	1 21 40.10	-60 -40 -51.60	3.391	5.209	7.955	0.895	1	-2.18	2
22953	2346	1 21 46.19	-60 -8 -4.50	3.792	4.507	8.495	0.988	1	-2.07	2
22953	2365	1 21 59.46	-59 -50 -40.10	4.071	4.671	7.200	0.722	1	-2.12	2
22953	2399	1 22 16.49	-61 -22 -32.80	2.175	3.675	7.522	0.760	1	-2.08	2
22953	2546	1 24 6.41	-58 -19 -27.00	2.174	4.258	6.057	0.720	1	-2.48	2
22953	2547	1 24 6.75	-58 -19 -44.20	2.137	4.256	6.213	0.726	1	-2.46	2
22953	2562	1 24 14.14	-62 -15 -56.30	4.176	4.023	3.861	0.461	1	-2.07	3
22953	2570	1 24 19.26	-59 -1 -43.10	5.120	4.062	3.865	0.484	1	-2.19	1
22953	2619	1 24 52.08	-58 -58 -23.50	3.198	2.027	3.038	0.436	1	-2.20	1
22953	2631	1 24 59.56	-59 -13 -51.90	3.321	3.896	5.307	0.553	1	-2.13	2
22953	2704	1 25 52.25	-61 -6 -22.50	3.714	4.373	6.915	0.693	1	-2.14	2
22953	2798	1 26 51.59	-62 -7 -7.80	2.895	4.445	6.478	0.646	1	-2.14	2
22953	2848	1 27 21.30	-59 -33 -31.10	6.992	2.294	3.006	0.460	1	-2.33	1
22953	2857	1 27 25.03	-62 -9 -39.70	3.796	1.917	8.572	1.094	2	-2.19	4
22953	2930	1 28 11.32	-60 -40 -0.80	2.560	4.151	8.054	0.854	1	-2.05	2
22953	3093	1 29 50.58	-59 -8 -16.70	2.728	1.431	2.479	0.438	1	-2.42	1
22953	3315	1 32 2.62	-59 -55 -18.50	3.791	4.936	5.702	0.556	1	-2.03	4
22953	3325	1 32 10.44	-58 -10 -13.70	2.156	2.758	6.158	0.597	1	-2.06	4
22953	3359	1 32 31.59	-58 -59 -28.70	2.873	3.993	5.851	0.624	1	-2.26	2
22953	3409	1 33 2.61	-58 -23 -32.40	2.514	3.865	7.300	0.733	1	-2.11	2
22953	3474	1 33 43.88	-59 -28 -0.50	2.070	2.807	4.982	0.545	1	-2.18	2
22953	3512	1 34 0.25	-61 -58 -46.50	5.043	4.028	6.689	1.198	1	-2.97	4
22953	3515	1 34 1.05	-61 -59 -19.90	4.887	4.075	4.215	0.564	1	-2.44	2

Table 6.1 (continued)

Plate	HK2	RA (B1950)	DEC	H18_2	K18_2	K18_f	BV0_f	Flux-class	[Fe/H]_p	MP-class
22953	3561	1 34 30.65	-60 -45 -50.30	7.493	8.537	8.488	1.060	1	-2.18	2
22953	3575	1 34 38.92	-60 -37 -25.80	3.580	4.628	6.506	0.652	1	-2.15	2
22953	3607	1 35 0.33	-59 -48 -6.90	4.247	3.978	4.377	0.488	1	-2.07	3
22968	142	3 26 7.96	-53 -46 -45.90	2.677	3.552	4.948	0.538	1	-2.16	2
22968	151	3 27 30.79	-55 -19 -49.00	4.272	2.762	7.294	0.869	1	-2.41	2
22968	208	3 25 36.74	-53 -44 -13.10	3.113	4.466	7.657	1.105	1	-2.61	2
22968	220	3 26 25.44	-54 -44 -27.60	4.651	5.402	6.323	0.614	1	-2.08	4
22968	303	3 26 12.27	-55 -8 -56.60	2.983	4.216	5.840	0.604	1	-2.19	2
22968	318	3 26 44.85	-55 -51 -23.40	4.943	5.686	6.981	0.723	1	-2.20	2
22968	338	3 24 44.81	-53 -45 -50.80	3.640	4.572	6.667	0.721	1	-2.31	2
22968	386	3 26 21.50	-56 0 -1.50	4.048	5.292	8.622	1.080	1	-2.14	4
22968	408	3 23 16.08	-52 -33 -12.60	4.779	6.539	8.234	0.873	1	-2.00	2
22968	410	3 26 27.53	-56 -17 -24.60	3.204	2.206	4.588	0.985	1	-3.11	2
22968	414	3 26 26.84	-56 -17 -53.00	3.819	3.193	4.361	0.746	1	-2.86	2
22968	424	3 23 30.72	-53 -3 -49.70	7.488	5.986	8.542	1.031	1	-2.11	2
22968	431	3 26 26.41	-56 -30 -12.20	3.482	4.467	6.747	0.649	1	-2.06	4
22968	437	3 22 57.61	-52 -30 -47.50	5.228	5.222	5.993	0.592	1	-2.10	4
22968	448	3 26 20.84	-56 -33 -55.30	3.204	4.264	6.843	0.752	1	-2.33	2
22968	454	3 24 54.25	-55 0 -53.50	4.482	6.142	5.963	0.568	1	-2.00	4
22968	462	3 24 29.62	-54 -37 -10.90	3.786	4.380	4.704	0.496	1	-2.02	3
22968	483	3 23 7.08	-53 -6 -35.20	2.201	2.962	4.862	0.594	1	-2.40	2
22968	493	3 24 3.81	-54 -20 -49.00	6.685	4.533	4.413	0.656	1	-2.67	2
22968	502	3 22 56.30	-53 -4 -17.50	3.106	4.070	5.777	0.574	1	-2.09	4
22968	506	3 25 20.62	-55 -59 -45.60	3.155	3.977	5.915	0.581	1	-2.07	4
22968	508	3 22 40.42	-52 -48 -6.20	5.207	4.513	4.954	0.513	1	-2.04	3

Table 6.1 (continued)

Plate	HK2	RA (B1950)	DEC	H18_2	K18_2	K18_f	BV0_f	Flux-class	[Fe/H]_p	MP-class
22968	514	3 26 6.75	-56 -54 -49.20	5.386	7.929	8.439	0.984	1	-2.09	2
22968	518	3 23 38.83	-54 -9 -41.00	2.020	2.674	4.281	0.570	1	-2.44	2
22968	521	3 23 15.96	-53 -45 -41.90	4.253	5.797	7.374	0.727	1	-2.06	2
22968	529	3 24 0.74	-54 -45 -11.50	6.938	3.411	5.062	0.565	1	-2.24	2
22968	536	3 23 28.71	-54 -10 -16.70	4.259	5.897	7.548	0.847	1	-2.27	2
22968	555	3 23 46.32	-54 -43 -48.40	3.526	4.787	6.169	0.594	1	-2.05	4
22968	560	3 21 56.53	-52 -27 -22.80	4.065	4.148	7.615	1.031	1	-2.54	2
22968	570	3 25 33.86	-56 -54 -41.20	3.505	5.336	8.301	0.992	1	-2.18	2
22968	580	3 23 11.93	-54 -14 -44.80	3.227	4.229	6.673	0.828	1	-2.54	2
22968	592	3 23 11.56	-54 -19 -44.50	3.836	6.017	8.031	1.097	1	-2.45	4
22968	605	3 24 12.56	-55 -40 -27.80	2.430	3.434	5.078	0.599	1	-2.37	2
22968	615	3 23 36.96	-55 -8 -11.60	3.506	4.543	5.642	0.560	1	-2.06	4
22968	620	3 24 30.09	-56 -12 -52.00	7.766	1.394	2.673	0.409	1	-2.19	1
22968	622	3 22 34.75	-53 -56 -38.70	4.123	4.866	5.307	0.542	1	-2.08	2
22968	646	3 24 18.41	-56 -16 -6.60	2.564	4.005	5.454	0.574	1	-2.18	2
22968	721	3 23 51.55	-56 -22 -14.70	3.419	4.378	6.128	0.597	1	-2.07	4
22968	784	3 20 43.42	-53 -6 -50.20	2.165	2.934	3.847	0.501	1	-2.27	2
22968	791	3 22 32.93	-55 -33 -21.90	4.612	6.372	6.376	0.650	1	-2.19	2
22968	796	3 22 16.60	-55 -14 -58.80	4.003	6.184	7.492	0.760	1	-2.10	2
22968	808	3 21 34.79	-54 -30 -40.30	4.006	4.930	6.240	0.604	1	-2.07	4
22968	821	3 20 41.86	-53 -26 -1.20	2.316	3.065	4.839	0.581	1	-2.36	2
22968	826	3 21 17.23	-54 -17 -16.60	4.766	6.949	7.694	0.759	1	-2.00	4
22968	830	3 20 26.75	-53 -10 -33.40	6.497	7.646	6.374	0.636	1	-2.14	2
22968	843	3 22 13.27	-55 -37 -22.10	2.640	4.383	5.651	0.633	1	-2.34	2
22968	866	3 20 2.01	-53 0 -15.00	2.485	2.945	4.005	0.547	1	-2.42	2

Table 6.1 (continued)

Plate	HK2	RA (B1950) DEC	H18_2	K18_2	K18_f	BV0_f	Flux-class	[Fe/H]_p	MP-class
22968	877	3 21 11.50 -54 -45 -1.00	3.143	4.622	5.805	0.573	1	-2.07	4
22968	909	3 21 59.06 -56 -7 -29.00	3.309	5.415	8.011	0.978	1	-2.30	2
22968	911	3 19 55.53 -53 -27 -47.90	4.339	6.478	7.549	0.854	1	-2.28	2
22968	926	3 20 12.03 -53 -57 -56.00	3.147	3.651	4.366	0.498	1	-2.12	2
22968	931	3 19 21.79 -52 -48 -38.70	3.169	4.692	5.885	0.601	1	-2.16	2
22968	949	3 22 24.24 -56 -56 -49.20	2.294	2.812	4.694	0.531	1	-2.19	2
22968	967	3 20 50.42 -55 -17 -32.50	2.333	2.863	4.563	0.690	1	-2.72	2
22968	968	3 18 54.33 -52 -38 -5.70	3.535	5.544	7.902	0.882	1	-2.18	2
22968	1047	3 19 12.25 -53 -53 -54.40	3.079	4.444	5.966	0.606	1	-2.16	2
22968	1065	3 21 10.61 -56 -42 -15.80	4.627	6.486	8.020	0.865	1	-2.09	2
22968	1079	3 19 40.38 -54 -52 -39.80	2.127	3.595	6.054	0.675	1	-2.37	2
22968	1090	3 18 28.26 -53 -18 -25.30	5.765	4.300	5.911	0.605	1	-2.17	2
22968	1092	3 19 16.62 -54 -28 -30.00	3.610	5.999	3.196	0.422	2	-2.07	1
22968	1103	3 18 51.34 -54 0 -32.20	3.481	4.185	5.516	0.554	1	-2.07	4
22968	1108	3 18 48.44 -54 -2 -52.70	4.597	5.628	7.188	0.717	1	-2.11	2
22968	1154	3 18 15.69 -53 -51 -28.80	2.592	3.595	5.062	0.574	1	-2.28	2
22968	1158	3 20 29.95 -56 -56 -22.20	3.947	1.270	2.269	0.379	1	-2.19	1
22968	1164	3 18 20.52 -54 -5 -49.10	2.864	4.422	6.589	0.638	1	-2.08	4
22968	1173	3 17 52.02 -53 -26 -29.60	3.401	5.315	6.157	0.619	1	-2.15	2
22968	1188	3 18 28.00 -54 -28 -5.70	4.666	5.800	6.444	0.610	1	-2.02	4
22968	1237	3 19 13.45 -55 -53 -25.10	3.514	5.443	6.363	0.613	1	-2.06	4
22968	1245	3 19 32.69 -56 -22 -26.50	2.852	3.847	4.888	0.518	1	-2.08	2
22968	1261	3 17 44.60 -54 -8 -33.00	5.170	8.273	6.641	0.633	3	-2.04	4
22968	1300	3 19 9.60 -56 -34 -25.80	3.259	4.115	4.793	0.548	1	-2.24	2
22968	1331	3 16 48.74 -53 -27 -34.40	3.006	2.756	2.754	0.441	1	-2.33	1

Table 6.1 (continued)

Plate	HK2	RA (B1950)	DEC	H18_2	K18_2	K18_f	BV0_f	Flux-class	[Fe/H]_p	MP-class
22968	1351	3 18 24.51	-56 -2 -35.50	6.261	8.193	7.901	0.805	1	-2.02	2
22968	1362	3 18 26.87	-56 -13 -47.10	5.880	6.273	6.798	0.650	1	-2.04	4
22968	1375	3 16 29.76	-53 -33 -26.30	2.758	3.618	4.794	0.540	1	-2.20	2
22968	1391	3 15 46.69	-52 -42 -17.40	3.732	6.621	6.363	0.630	1	-2.12	4
22968	1393	3 16 13.99	-53 -29 -32.90	3.406	3.663	4.460	0.512	1	-2.16	2
22968	1395	3 17 12.05	-55 0 -46.20	2.917	4.339	6.132	0.583	1	-2.01	4
22968	1446	3 17 45.17	-56 -29 -56.80	3.432	4.798	6.410	0.705	1	-2.35	2
22968	1454	3 17 44.32	-56 -34 -10.40	2.380	3.834	6.928	0.886	1	-2.57	2
22968	1464	3 17 52.95	-56 -52 -35.20	2.687	3.853	5.538	0.560	1	-2.09	2
22968	1489	3 16 41.58	-55 -25 -58.90	3.683	5.598	7.831	0.874	1	-2.20	2
22968	1493	3 17 1.38	-55 -57 -1.50	3.422	4.450	6.163	0.608	1	-2.11	4
22968	1497	3 14 49.75	-52 -30 -10.40	2.043	2.902	6.546	0.899	1	-2.69	2
22968	1499	3 15 42.26	-54 0 -7.50	6.751	7.101	6.996	0.670	1	-2.04	4
22968	1500	3 16 49.61	-55 -43 -59.20	3.657	3.799	5.718	0.582	1	-2.14	2
22968	1517	3 16 27.10	-55 -19 -23.80	3.855	5.755	6.765	0.645	1	-2.04	4
22968	1526	3 15 8.17	-53 -21 -20.00	4.166	4.478	4.721	0.502	1	-2.04	3
22968	1531	3 14 57.01	-53 -7 -31.30	3.437	5.132	6.390	0.679	1	-2.28	2
22968	1541	3 14 56.40	-53 -15 -29.30	4.548	0.694	2.212	0.371	1	-2.17	1
22968	1594	3 16 19.22	-56 -13 -9.70	2.442	3.392	4.361	0.503	1	-2.15	2
22968	1613	3 15 39.96	-55 -31 -58.10	2.010	2.635	4.989	0.560	1	-2.24	2
22968	1615	3 13 48.50	-52 -27 -0.30	4.049	5.410	7.189	0.701	1	-2.06	4
22968	1637	3 14 16.40	-53 -33 -36.90	2.822	3.951	6.108	0.674	1	-2.35	2
22968	1639	3 16 18.74	-56 -47 -45.60	3.055	3.907	4.364	0.479	1	-2.02	3
22968	1645	3 14 40.76	-54 -22 -36.20	2.747	3.817	6.935	0.820	1	-2.45	2
22968	1654	3 14 30.86	-54 -15 -29.30	4.836	5.421	6.470	0.678	1	-2.25	2

Table 6.1 (continued)

Plate	HK2	RA (B1950)	DEC	H18_2	K18_2	K18_f	BV0_f	Flux-class	[Fe/H]_p	MP-class
22968	1661	3 15 37.68	-56 -5 -17.40	2.884	4.082	5.938	0.597	1	-2.13	2
22968	1669	3 14 11.04	-53 -51 -7.30	2.810	3.254	4.029	0.517	1	-2.30	2
22968	1694	3 14 8.43	-54 -3 -41.60	7.029	6.688	6.622	0.623	1	-2.01	4
22968	1700	3 14 25.77	-54 -36 -11.60	2.360	2.841	4.782	0.822	1	-2.91	2
22968	1713	3 14 39.05	-55 -8 -51.60	2.289	3.530	7.051	0.869	1	-2.50	2
22968	1714	3 15 45.35	-56 -52 -33.00	2.334	4.139	5.356	0.545	1	-2.08	2
22968	1719	3 13 27.40	-53 -10 -18.30	3.990	5.963	7.663	0.887	1	-2.30	2
22968	1720	3 13 27.68	-53 -11 -55.00	2.381	3.165	6.761	0.981	1	-2.75	2
22968	1738	3 12 55.41	-52 -30 -27.70	2.418	3.132	4.725	0.571	1	-2.35	2
22968	1755	3 12 51.14	-52 -35 -31.70	4.609	5.852	6.532	0.622	1	-2.04	4
22968	1771	3 14 38.32	-55 -51 -46.20	2.269	3.068	5.236	0.592	1	-2.30	2
22968	1841	3 14 48.33	-57 -2 -12.50	2.670	2.985	3.227	0.492	1	-2.41	1
22968	1880	3 14 30.90	-57 -2 -40.20	3.137	4.866	6.212	0.588	1	-2.01	4
22968	1887	3 12 44.99	-54 -10 -48.90	2.354	4.848	4.631	0.649	1	-2.61	2
22968	1905	3 14 6.86	-56 -40 -27.80	3.334	4.703	6.431	0.605	1	-2.00	4
22968	1915	3 12 39.05	-54 -25 -55.70	3.205	4.463	6.688	0.691	1	-2.22	2
22968	1956	3 11 35.69	-52 -52 -39.70	2.586	3.746	5.426	0.609	1	-2.32	2
22968	1998	3 13 7.81	-56 -17 -57.40	3.229	4.568	6.407	0.657	1	-2.20	2
22968	2020	3 13 10.22	-56 -40 -48.50	3.163	4.903	6.876	0.739	1	-2.28	2
22968	2038	3 11 11.87	-53 -24 -27.80	4.228	1.197	2.348	0.456	1	-2.55	1
22968	2099	3 11 35.00	-55 -7 -9.40	3.166	5.599	7.853	0.828	1	-2.09	2
22968	2136	3 12 3.94	-56 -32 -32.20	3.102	3.300	3.777	0.493	1	-2.26	1
22968	2144	3 10 4.21	-53 -2 -16.50	4.360	6.048	7.746	0.936	1	-2.35	2
22968	2146	3 11 46.54	-56 -27 -17.60	2.164	7.058	5.675	0.694	2	-2.51	2
22968	2150	3 9 56.64	-52 -54 -57.10	5.105	6.514	7.329	0.768	1	-2.19	2

Table 6.1 (continued)

Plate	HK2	RA	(B1950)	DEC	H18_2	K18_2	K18_f	BV0_f	Flux-class	[Fe/H]_p	MP-class
22968	2157	3 9 43.42	-52 -37 -39.90		3.841	4.574	5.458	0.568	1	-2.15	2
22968	2207	3 11 24.15	-56 -48 -7.20		4.557	3.204	6.298	0.660	1	-2.25	2
22968	2217	3 9 33.57	-53 -20 -3.20		3.948	5.116	6.318	0.607	1	-2.05	4
22968	2219	3 10 27.74	-55 -11 -44.90		3.329	2.375	2.665	0.384	1	-2.04	1
22968	2222	3 9 33.54	-53 -21 -49.20		5.483	6.328	6.831	0.928	1	-2.66	2
22968	2223	3 11 27.62	-57 -6 -17.40		4.714	4.018	4.268	0.490	1	-2.11	1
22968	2241	3 10 54.85	-56 -25 -19.30		3.318	4.767	6.329	0.653	1	-2.22	2
22968	2254	3 10 16.31	-55 -24 -47.00		5.255	2.993	2.617	0.417	1	-2.26	1
22968	2297	3 10 38.32	-56 -43 -38.30		2.447	3.785	4.396	0.498	1	-2.11	2
22968	2299	3 8 56.50	-53 -17 -21.00		4.782	6.216	7.660	0.796	1	-2.11	2
22968	2300	3 9 27.91	-54 -26 -3.50		4.463	6.720	7.513	0.766	1	-2.10	2
22968	2306	3 10 45.37	-57 -3 -56.00		4.699	6.323	7.572	0.783	1	-2.12	2
22968	2322	3 8 54.22	-53 -39 -49.80		5.085	5.796	7.494	0.775	1	-2.13	2
22968	2328	3 8 52.72	-53 -42 -38.30		5.792	6.460	6.372	0.600	1	-2.00	4
22968	2329	3 8 40.27	-53 -17 -27.80		4.914	5.526	5.499	0.549	1	-2.06	4
22968	2364	3 9 44.31	-56 -12 -37.50		4.115	5.710	7.528	0.746	1	-2.04	2
22968	2377	3 8 16.33	-53 -20 -0.10		4.521	6.412	6.513	0.613	1	-2.01	4
22968	2382	3 7 57.64	-52 -39 -8.80		4.894	5.270	6.187	0.617	1	-2.13	4
22968	2394	3 9 57.84	-57 -12 -47.50		2.230	2.510	4.208	0.676	1	-2.75	2
22968	2401	3 9 35.80	-56 -36 -16.50		4.548	6.038	6.978	0.666	1	-2.03	4
22968	2412	3 8 58.08	-55 -34 -38.00		3.054	3.445	5.582	0.556	1	-2.06	4
22968	2414	3 7 58.58	-53 -25 -44.40		3.302	4.235	6.150	0.602	1	-2.09	4
22968	2433	3 8 24.84	-54 -47 -12.10		4.065	2.061	3.301	0.591	2	-2.72	2
22968	2434	3 8 24.49	-54 -46 -45.20		4.214	2.336	6.851	1.079	2	-2.83	2
22968	2445	3 8 37.93	-55 -26 -20.40		2.293	3.173	6.166	0.610	1	-2.11	4

Table 6.1 (continued)

Plate	HK2	RA (B1950)			DEC			H18_2	K18_2	K18_f	BV0_f	Flux-class	[Fe/H]_p	MP-class
22968	2495	3	7	12.67	-53	0	-57.00	3.757	2.691	2.960	0.455	1	-2.32	1
22968	2511	3	8	20.94	-55	-54	-21.10	3.093	4.960	6.757	0.646	1	-2.04	4
22968	2551	3	8	30.23	-57	-8	-8.80	3.085	4.730	7.954	1.034	1	-2.40	2
22968	2562	3	7	56.44	-56	-7	-10.50	2.563	4.011	6.001	0.577	1	-2.03	4
22968	2563	3	6	48.14	-53	-31	-8.10	3.173	3.496	4.642	0.540	1	-2.24	2
22968	2568	3	6	57.56	-54	-2	-10.20	5.249	6.014	7.225	0.721	1	-2.10	2
22968	2584	3	6	27.13	-52	-58	-21.30	3.326	4.804	6.520	0.648	1	-2.14	2
22968	2593	3	7	30.94	-55	-47	-40.40	2.420	3.001	5.093	0.561	1	-2.22	2
22968	2597	3	6	33.30	-53	-31	-23.80	2.900	3.893	5.566	0.610	1	-2.29	2
22968	2598	3	6	32.03	-53	-31	-12.90	2.895	3.885	5.862	0.608	1	-2.20	2
22968	2633	3	6	51.92	-55	-7	-40.40	5.912	4.866	5.834	0.575	1	-2.07	4
22968	2653	3	6	45.29	-55	-5	-26.00	3.785	4.815	7.032	0.713	1	-2.16	2
22968	2675	3	7	28.42	-57	-3	-26.60	2.814	4.290	5.736	0.554	1	-2.01	4
22968	2680	3	6	11.24	-54	-6	-27.30	3.161	3.918	6.000	0.592	1	-2.09	4
22968	2702	3	6	9.66	-54	-28	-3.60	5.186	6.574	8.112	0.843	1	-2.00	2
22968	2705	3	5	48.39	-53	-34	-52.50	2.709	4.190	6.301	0.629	1	-2.14	2
22968	2713	3	6	19.79	-55	-3	-5.90	3.326	4.059	6.851	0.644	1	-2.00	4
22968	2718	3	6	15.46	-54	-55	-12.60	5.384	6.589	8.046	0.862	3	-2.07	2
22968	2734	3	7	7.61	-57	-11	-55.40	2.471	3.924	7.337	0.791	1	-2.24	2
22968	2735	3	5	28.45	-53	-6	-32.50	2.934	3.964	4.863	0.573	1	-2.32	2
22968	2741	3	7	5.72	-57	-12	0.00	1.997	3.635	6.871	0.873	1	-2.56	2
22968	2756	3	6	17.93	-55	-36	-36.10	4.193	5.955	7.717	0.842	1	-2.19	2
22968	2760	3	6	18.63	-55	-49	-13.50	2.956	3.638	5.135	0.557	1	-2.19	2
22968	2800	3	6	15.96	-56	-28	-17.20	3.172	3.435	4.311	0.491	1	-2.10	3
22968	2825	3	4	49.29	-53	-16	-22.70	2.762	4.070	6.133	0.690	1	-2.39	2

Table 6.1 (continued)

Plate	HK2	RA (B1950)			DEC			H18_2	K18_2	K18_f	BV0_f	Flux-class	[Fe/H]_p	MP-class
22968	2831	3	4	39.90	-52	-53	-53.30	1.953	2.571	4.463	0.597	1	-2.49	2
22968	2852	3	4	36.16	-53	-3	-14.80	3.507	4.758	5.129	0.610	1	-2.39	2
22968	2861	3	5	23.20	-55	-21	-38.60	2.661	4.164	6.795	0.678	1	-2.14	2
22968	2902	3	4	25.46	-53	-49	-15.10	2.692	3.807	6.329	0.665	1	-2.25	2
22968	2906	3	4	25.19	-53	-59	-51.80	3.315	5.062	6.010	0.570	1	-2.00	4
22968	2917	3	4	31.91	-54	-39	-16.20	2.370	4.104	7.242	0.835	1	-2.37	2
22968	2922	3	5	3.10	-56	-14	-9.00	3.092	3.471	4.770	0.534	1	-2.18	2
22968	2923	3	3	54.42	-53	-2	-17.90	3.570	4.954	8.050	1.056	1	-2.39	2
22968	2933	3	5	7.02	-56	-38	-6.40	2.642	3.616	4.804	0.529	1	-2.15	2
22968	2949	3	4	54.99	-56	-28	-15.10	3.116	5.147	7.220	0.725	1	-2.12	2
22968	3007	3	3	36.46	-53	-51	-36.00	3.623	4.388	5.884	0.573	1	-2.05	4
22968	3049	3	3	21.83	-54	-1	-55.30	3.759	5.648	7.400	0.771	1	-2.16	2
22968	3052	3	3	25.38	-54	-18	-28.90	4.552	2.991	3.340	0.605	1	-2.75	2
22968	3087	3	2	57.94	-53	-33	-22.00	3.157	0.717	2.057	0.339	1	-2.03	1
22968	3130	3	2	55.15	-54	-22	-37.80	3.333	3.968	5.293	0.610	1	-2.35	2
22968	3161	3	2	41.64	-54	-22	-9.10	4.393	5.927	8.299	0.921	1	-2.06	2
22968	3162	3	3	8.16	-55	-47	-28.20	4.032	5.830	6.454	0.609	1	-2.01	4
22968	3167	3	2	39.71	-54	-27	-20.00	4.732	4.510	5.972	0.623	1	-2.22	2
22968	3183	3	2	32.35	-54	-29	-57.90	3.510	4.504	6.253	0.611	1	-2.09	4
22968	3264	3	2	11.46	-55	-29	-45.30	3.058	3.963	6.747	0.779	1	-2.42	2
22968	3304	3	1	55.09	-55	-40	-35.40	3.083	4.593	6.895	0.821	1	-2.46	2
22968	3316	3	0	58.98	-52	-35	-9.20	3.142	2.984	4.026	0.461	1	-2.02	3
22968	3319	3	1	57.57	-56	-8	-2.70	4.903	4.828	4.906	0.517	1	-2.07	2
22968	3343	3	0	58.41	-53	-6	-42.80	2.689	4.070	6.626	0.740	1	-2.37	2
22968	3487	3	0	22.40	-55	-4	-28.40	6.548	3.137	3.565	0.518	2	-2.42	2

Table 6.1 (continued)

Plate	HK2	RA (B1950)	DEC	H18_2	K18_2	K18_f	BV0_f	Flux-class	[Fe/H]_p	MP-class
22968	3500	2 59 51.95	-53 -21 -37.90	3.227	4.674	6.722	0.682	1	-2.18	2
22968	3589	2 59 5.54	-53 -9 -25.70	2.446	3.610	5.128	0.545	1	-2.14	2
22968	3594	2 59 19.92	-54 -28 -9.80	3.123	4.779	7.023	0.746	1	-2.25	2
22968	3681	2 58 23.90	-53 -8 -18.80	4.056	5.297	6.464	0.613	1	-2.03	4
22968	3746	2 58 3.25	-53 -58 -54.60	6.447	4.548	6.284	0.601	2	-2.04	4
22968	3839	2 57 59.15	-56 -59 -56.50	2.072	3.556	6.697	0.651	1	-2.08	4
22968	3887	2 57 6.62	-53 -56 -34.70	5.772	5.073	5.158	0.520	1	-2.01	3
22968	3999	2 56 5.53	-53 -6 -7.60	2.347	4.009	6.164	0.615	1	-2.13	4
22968	4015	2 56 0.78	-53 -19 -57.50	2.697	3.819	6.532	0.711	1	-2.33	2
22968	4025	2 56 7.95	-54 -44 -2.10	3.993	5.567	6.761	0.646	1	-2.04	4
22968	4027	2 56 6.98	-54 -44 -4.00	3.974	5.540	6.795	0.637	1	-2.00	4
22968	4166	2 55 25.67	-56 -57 -56.20	4.991	7.054	7.274	0.787	1	-2.25	2
22968	4181	2 54 50.51	-52 -53 -53.20	6.106	5.059	7.800	0.865	1	-2.20	2
29499	134	23 54 46.55	-23 -36 -56.70	4.203	4.371	7.278	0.776	2	-2.23	2
29499	262	23 53 51.09	-23 -11 -29.50	10.291	5.221	7.082	0.808	3	-2.37	2
29499	350	23 53 13.39	-23 -15 -4.50	2.711	4.732	7.925	0.820	1	-2.04	2
29499	583	23 51 29.82	-25 -43 -58.80	3.970	3.672	4.626	0.661	2	-2.64	2
29499	713	23 50 28.23	-23 -50 -2.20	2.229	3.918	7.684	0.756	1	-2.00	4
29499	997	23 48 31.20	-23 -2 -11.80	2.196	7.024	7.109	0.683	1	-2.03	4
29499	1437	23 45 13.40	-27 -15 -30.50	6.797	5.540	5.304	0.526	2	-2.00	3
29499	1932	23 42 21.78	-24 -42 -56.20	6.243	4.536	5.014	0.596	2	-2.37	2
29499	1933	23 42 21.66	-24 -43 -32.70	6.208	4.502	4.559	0.523	2	-2.19	2
29499	2424	23 39 17.83	-27 -18 -57.20	7.018	5.512	5.875	0.604	2	-2.18	2
29499	2841	23 37 5.95	-23 -50 -51.00	2.308	4.597	5.845	0.640	1	-2.31	2
29505	210	3 38 2.25	-45 -49 -3.10	5.732	3.091	2.124	0.351	3	-2.08	1

Table 6.1 (continued)

Plate	HK2	RA (B1950)	DEC	H18_2	K18_2	K18_f	BV0_f	Flux-class	[Fe/H]_p	MP-class
29505	1016	3 34 19.41	-45 -17 -38.30	4.040	4.003	6.032	0.768	1	-2.60	2
29505	1811	3 30 13.19	-44 -9 -20.10	2.999	3.838	4.855	0.677	1	-2.64	2
29505	1817	3 30 10.13	-43 -32 -27.60	4.704	1.717	2.216	0.427	1	-2.47	1
29505	1849	3 30 4.27	-44 -9 -44.30	2.751	3.526	7.923	0.975	1	-2.33	2
29505	2506	3 26 31.37	-46 -6 -15.10	5.756	12.358	8.438	0.929	3	-2.00	2
29505	2809	3 24 7.44	-44 -30 -2.90	2.469	8.548	7.275	0.724	1	-2.09	2
29505	3187	3 21 11.08	-44 -34 -40.30	10.078	5.979	5.495	0.602	2	-2.27	2
29505	3208	3 20 38.72	-47 -26 -3.60	7.056	3.858	3.522	0.503	1	-2.37	2
29505	3224	3 20 48.40	-45 -22 -37.20	7.210	5.051	6.089	0.717	1	-2.47	2
29505	3674	3 17 5.94	-47 -5 -30.20	5.590	5.769	7.463	0.787	1	-2.18	2
29505	3884	3 16 10.79	-44 -24 -19.70	5.290	4.255	3.414	0.528	2	-2.50	2
29505	4089	3 14 38.64	-45 -12 -31.90	4.913	6.806	6.698	0.640	1	-2.04	4
29505	4151	3 14 2.00	-45 -43 -27.70	2.824	4.041	8.394	0.935	1	-2.03	2
30315	964	23 29 19.54	-24 -12 -43.60	8.102	3.135	3.546	0.559	2	-2.57	2
30315	1192	23 27 54.28	-22 -46 -29.30	5.742	5.236	7.019	0.797	1	-2.37	2
30315	1193	23 27 54.28	-22 -46 -17.60	5.646	5.298	6.934	0.769	1	-2.34	2
30315	1623	23 24 58.50	-25 -46 -58.50	5.509	5.930	7.934	0.943	1	-2.28	2
30315	2056	23 22 26.98	-22 -50 -31.30	5.667	4.115	3.735	0.497	1	-2.29	1
30315	2199	23 21 13.80	-24 -59 -46.60	2.854	6.904	7.144	0.711	1	-2.11	2
30315	2860	23 16 36.80	-26 -45 -44.80	7.018	5.723	5.888	0.602	1	-2.17	2
30315	3060	23 15 23.80	-26 -47 -36.80	5.307	3.321	3.467	0.484	1	-2.30	1
30315	3157	23 14 47.04	-25 -43 -5.20	7.285	4.330	6.213	0.626	2	-2.16	2
30493	192	23 21 1.76	-35 -54 -54.30	8.270	3.213	3.829	0.658	2	-2.78	2
30493	539	23 18 4.93	-34 -10 -28.30	2.382	3.635	7.865	0.827	1	-2.09	2
30493	978	23 15 0.97	-33 -22 -4.70	6.414	6.595	8.354	0.905	1	-2.00	2

Table 6.1 (continued)

Plate	HK2	RA (B1950)	DEC	H18_2	K18_2	K18_f	BV0_f	Flux-class	[Fe/H]_p	MP-class
30493	2050	23 7 23.59	-34 -10 -48.80	2.844	3.960	8.546	0.969	1	-2.01	2
30493	2094	23 7 1.05	-35 -6 -41.10	2.978	3.493	8.307	0.891	1	-2.00	2
30493	2216	23 6 10.23	-34 -25 -14.20	5.374	6.459	8.977	1.157	1	-2.05	4
30493	2383	23 4 50.20	-36 -20 -32.70	2.379	3.522	8.162	0.954	1	-2.19	2
30493	2385	23 5 3.58	-33 -18 -34.70	4.803	3.936	4.431	0.523	1	-2.22	2
30493	2706	23 2 58.76	-34 -38 -26.70	4.126	5.214	7.277	0.769	1	-2.21	2

Chapter 7

CONCLUSIONS

The objective of this thesis was to develop algorithms to reduce a large set of objective-prism data in a highly efficient manner, and to use the techniques developed to select extremely metal-poor star candidate stars in the Galaxy with great reliability. This first task was successfully accomplished, and we now have a procedure by which on the order of 1.5 million prism spectra can be rapidly and accurately reduced and analyzed. New methodology making use of an Artificial Neural Network approach was developed in order to achieve the second goal. The results of this effort are quite encouraging. The application of this technique to obtain estimates of stellar metallicity for a large set of comparison stars, using accurate input data obtained from medium-resolution spectroscopy and broadband colors, demonstrated that the trained networks were able to predict the metallicity of a star, [Fe/H], with high accuracy (with a scatter of only $S_{BI} = 0.13$ dex). Application of the ANN approach with the inherently less accurate information obtained from the digitized scans of the HK objective prism plates, and a rough estimate of colors provided by a calibration of photographic photometry, yielded a metal abundance estimate with a scatter of $S_{BI} = 0.78$ dex. Though this is larger than we would prefer, it is still quite acceptable for use in the candidate selection process. We expect, based on our tests with stars of known abundance, that if spectroscopic follow-up of the candidates predicted to have an abundance [Fe/H] < -2.0 were carried out, on the order of 60% of them would indeed turn out to be at or below this metallicity, and that we would have identified at least 30% of all such stars that are present on the plates. In order to improve the results for prediction and classification, we suspect that an additional step will be required, which will recalibrat the equivalent widths and color estimates for the hotter stars. This is the next task for this program, and should be carried out in the near future.

The metal-poor stars identified in the HK survey to date have been used to explore many aspects of the early nucleosynthesis and stellar dynamics in the Milky Way. However, owing to the visual selection criteria used in the original HK survey, it should be kept in mind that most of the presently known metal-poor stars are stars that are hotter than the Sun, and located in the solar neighborhood (within a few kpcs). In order to assemble a more representative data set, we need to identify additional metal-poor stars at greater distances, and over a wider range of temperatures. A large fraction of the cooler metal-deficient stars that were missed in the visual selection will likely be recovered by the selection procedure employed in this thesis.

During the past few years, and in the coming decade, new astrometric surveys (such as the Yale SPM, and the NASA satellite missions FAME and SIM) hold the possibility of providing proper motions for most of the HK survey stars. With this information in hand, and with medium-resolution spectroscopic follow-up of the newly identified candidates from this thesis, it will be feasible to construct a very large catalog of stars with highly accurate positions, distance estimates, proper motions, and radial velocities, over the entire range of metallicities known to exist in the Galaxy ($-4.0 < [Fe/H] < +0.3$). Importantly, this catalog will not suffer from any of the kinematic selection biases which have confounded the analysis of stellar motions in the past. The full space motions of these stars that will be derived will uncover the dynamical history of the thick disk and halo populations of the Galaxy, and aid in the identification of kinematic substructure in the halo, which in turn will place constraints on galaxy formation scenarios. High-resolution spectroscopic observations of the *most* metal-deficient stars identified by procedures such as ours are already underway with 8m-10m class telescopes (VLT, KECK, SUBARU), and are beginning to provide exquisite information on the early chemical evolution of our Galaxy. The next decade will see a literal explosion of insight into the workings of the early Universe, as recorded by these special, but extremely rare, stars.

APPENDIX

APPENDIX

ARTIFICIAL NEURAL NETWORKS

This portion of the thesis is intended to provide basic concepts of Artificial Neural Networks (ANNs) for those unfamiliar with the techniques. More detailed information can be found in some general references, for example, Hertz, Krogh, & Palmer (1991) and Bailer-Jones (1996).

A.1 Motivation

An Artificial Neural Network (ANN) is a computational tool which enables us to map from a few available measured variables (inputs) to some desired physical variables (outputs). ANNs were originally motivated by the possibility of imitating the networks of nerve cells in the human brain. The brain consists of roughly 100 billion neurons, each of which are connected with some 1,000 to 10,000 other neurons, typically. This large number of multiple connections makes it possible for the brain to learn from experience, memorize, and solve new problems utilizing the stored information. Although the technology is termed "neural network," one should keep in mind that it only mimics the behavior of real biological neurons.

A.2 Neuron

Figure A.1 shows the basic structure of a single neuron. There are four parts – dendrites, the soma (cell body), the axon, and synapses. The dendrites receive inputs from the synapses of other neurons and the soma processes the inputs. When the processed inputs attain some threshold value, outputs are transmitted through the axon into synapses where other neurons accept the outputs.

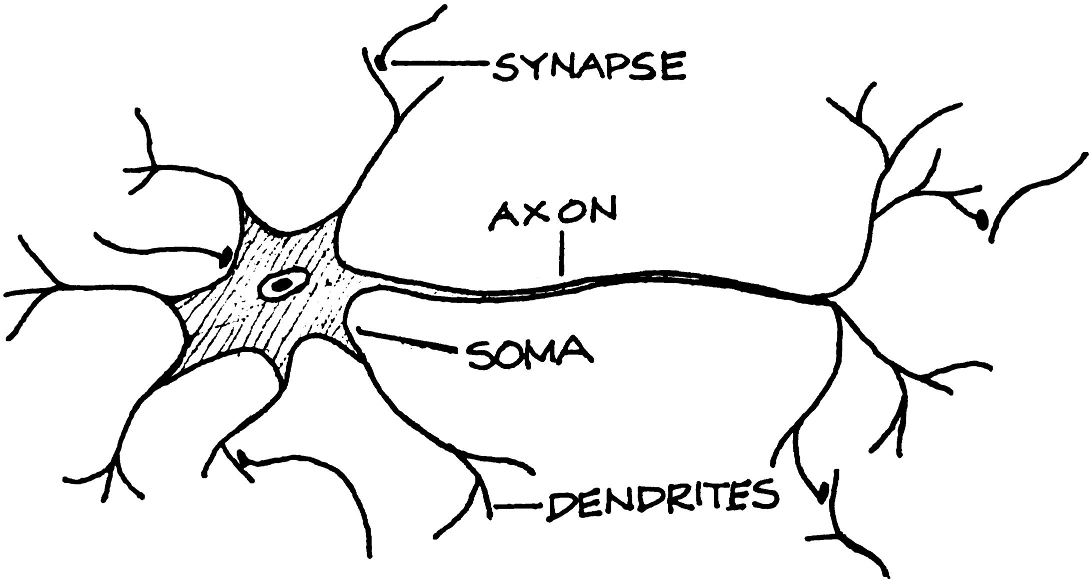

Figure A.1 Structure of a "biological" neuron (after Hertz et al. 1991).

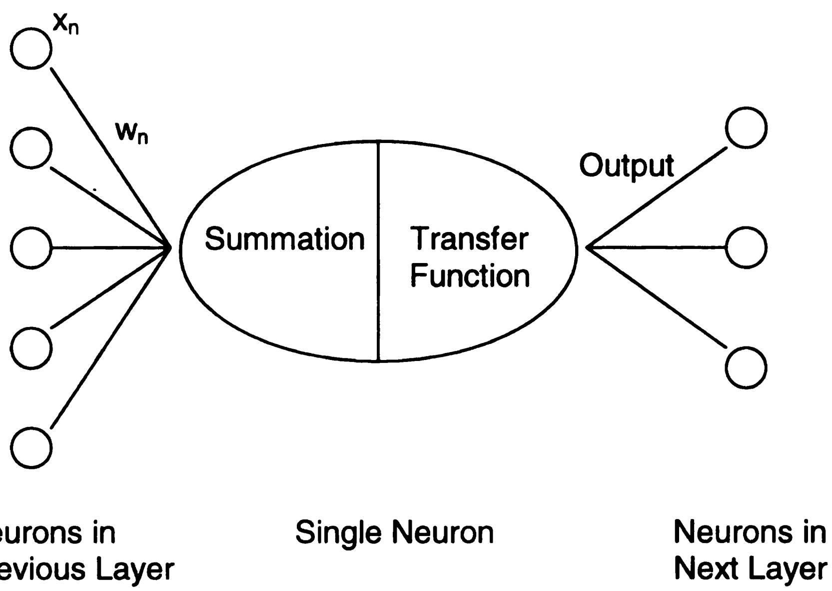

Figure A.2 Schematic diagram of a single "artificial" neuron (after Bailer-Jones 1996).

Figure A.2 is a schematic diagram of an artificial neuron (or node). Each neuron is connected with various inputs (x_n) which are the processed outputs, typically from the previous layer. Each connection has its own weight (w_n). The neuron receives the summation of weighted inputs ($y=\Sigma w_n x_n$), and then lets it pass through a transfer function to generate a result (z) that will be an input for other neurons in the next layer. In general, a non-linear sigmoid function of the form $z = 1 / (1+Exp(-y))$ is used as a transfer function. Note that y takes on values between $-\infty$ and $+\infty$ and is nonlinearly converted into a z value between 0 and 1.

A.3 Multi-Layer Perceptron (MLP)

A MLP neural network architecture is shown in Figure A.3. Neurons in the input layer feed on input variables (e.g., the spectrum or equivalent width of a line) without the summation and pass them into all neurons in next layer. All layers between the input layer and output layer are referred to as "hidden layers" since they do not have entrances or exits to outside. Neurons in the hidden layer process their inputs with the method explained in previous section and transmit the non-linearly generated results to other neurons in the next layer. The output layer can have a single neuron or multiple neurons, depending on one's preference, and the application in hand. Because the data stream from input layer to output layer via hidden layers (that is, they make a one way trip), these architectures are often called feed-forward networks.

The training or learning step means a process to find out the optimized connection weights that produce final outputs that are closest to the desired results. There are two training methods: supervised and unsupervised. In supervised learning, a trainer provides the network with both inputs and corresponding outputs.

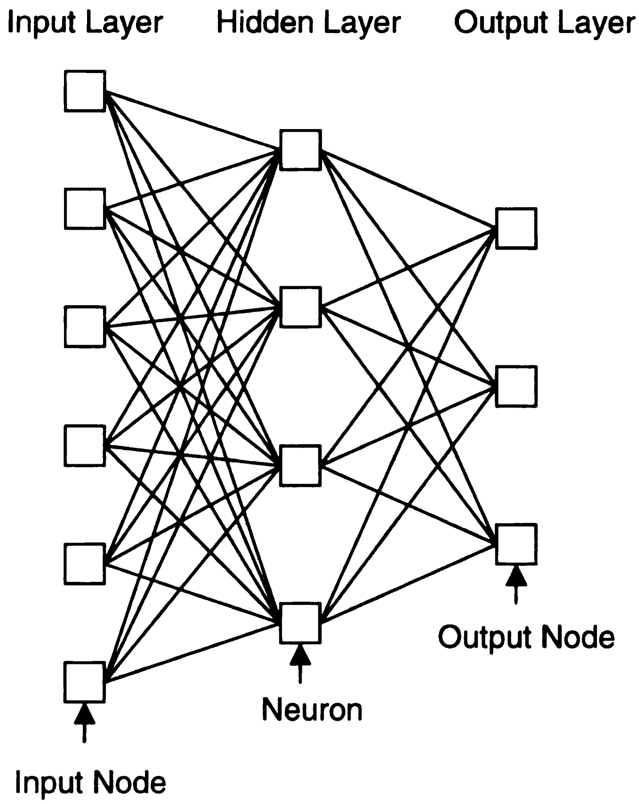

Figure A.3 Architecture of a multi-layer neural network with a single hidden layer (after Hertz et al. 1991).

The network then tries to find optimized weights by comparing answers and the results derived from it. In unsupervised learning, only inputs are provided into a network so that it should determine for itself some useful predictive features associated with the input data. Currently only the supervised training is well understood, and it is the approach used in the vast majority of ANN applications. I also made use of the supervised learning in this thesis.

If the desired output is a continuous variable, such as temperature or the metallicity of a star, the number of neurons in output layer is only one, for that particular variable. On the other hand, if one wishes to classify data into groups by some physical characteristics (e.g., luminosity class), the number of neurons in output layer needs to be the same as the number of groups. The former case is often called prediction or continuous mode, while the latter case is referred as to classification or probabilistic mode. In classification mode, the outputs are probabilities for corresponding class (output nodes), whereas the physical parameter directly comes out as an output in the prediction mode.

The training process starts with randomly chosen (small) weights. Once the network produces some outputs, a comparison between the outputs and desired target is done using a cost function defined as,

$$E = \frac{1}{2}\sum_{k}(O_k - T_k)^2$$

where O_k is the output of k^{th} output neuron and T_k is the target for it. The goal is to minimize the cost function in weight space (Note that E is a function of weights). The error information is propagated backward to a previous layer to update weights (and is thus often called a back-propagation network). After numerous iterations, the step size of weights is determined by using the gradient descent, and adding a momentum term to the chain rule as follows.

$$\Delta w_{pq}(t+1) = -\eta \frac{\partial E}{\partial w_{pq}} + \alpha \Delta w_{pq}(t)$$

The learning rate, η, controls the rate of updating. The second term, which includes the momentum parameter, α, increases the possibility of finding the true minimum of E over the entire weight space, rather than have the procedure become trapped into local minima. If there is no improvement with the errors, the training process is halted.

The complexity of networks depends on the number of hidden layers and the numbers of neurons in them. If there are not sufficient connection weights, the network will generally produce an "under-fit" solution. On the other hand, if too many weights are used, the training time increases enormously and an "over-fit" solution is obtained. In addition, training data set should be composed of representative values over inputs and outputs to avoid over-fitting or incorrect fitting, with too much emphasis put on certain regions of the data space. Therefore, the use of appropriate numbers of neurons and hidden layers is the key to successfully produce a well-trained network. Masters (1993) provides some general guideline in designing network architecture. A single hidden layer is recommended to be used in most cases, except when desired parameter exhibits some discontinuities. Masters recommends that, at least for a starting point, the number of neurons should be taken to be the square root of the product of the number of inputs and the number of outputs.

LIST OF REFERENCES

LIST OF REFERENCES

Alcock, C. et al. 1995, ApJ, 445, 133

Anthony-Twarog, B. J., Sarajedini, A., Twarog, B. A., & Beers, T. C. 2000, AJ, 119, 2882

Armandroff, T. E. 1989, AJ, 97, 375

Armandroff, T. E. 1993, The Globular Cluster – Galaxy Connection, ASP Conference Series, Vol. 48, G. H. Smith, and J. P. Brodie, eds. (Astronomical Society of the Pacific, San Francisco), p. 48

Bailer-Jones, C. A. L. 1996, Ph.D. Thesis, University of Cambridge, United Kingdom

Bailer-Jones, C. A. L. 1997, MNRAS, 292, 157

Bailer-Jones, C. A. L. 2000, A&A, 357, 197

Bailer-Jones, C. A. L., Irwin, M., & von Hippel, T. 1998a, 298, 361

Bailer-Jones, C. A. L., Irwin, M., & von Hippel, T. 1998b, 298, 1061

Bazell, D., & Peng, Y. 1998, ApJS, 116, 47

Beers, T. C. 1999a, Ap&SS, 265, 105

Beers, T. C. 1999b, astro-ph/9911171

Beers, T. C., Flynn, K., & Gebhardt, K. 1990, AJ, 100, 32

Beers, T. C., Preston, G. W., & Shectman, S. A. 1985, AJ, 90, 2089

Beers, T. C., Preston, G. W., & Shectman, S. A. 1992, AJ, 103, 1987

Beers, T. C., Rossi, S., Anthony-Twarog, B., Twarog, B., Hawley, S., Rhee, J., Tourtellot, J., Wilhelm, R., & Sarajedini, A. 2000, in preparation

Beers, T. C., Rossi, S., Norris, J. E., Ryan, S. G., & Shefler, T. 1999, AJ, 117, 981

Beers, T. C., & Sommer-Larsen, J. 1995, ApJS, 96, 175

Bharadwaj, S., Sahni, V., Sathyaprakash, B. S., Shandarin, S. F., & Yess, C. 2000, ApJ, 528, 21

Binney, J. J., Gerhard, O. E., & Spergel, D. N. 1997, MNRAS, 288, 365

Cannon, A. J. 1925-36, Annual Harvard College Observatory, 100, 1 (The Henry Draper Extension)

Cannon, A. J. 1949, Annual Harvard College Observatory, 112, 1 (The Henry Draper Extension Charts)

Cannon, A. J., & Pickering, E. C. 1918-24, Annual Harvard College Observatory, 91-99 (The Henry Draper Catalogue)

Carney, B. W. 1996, Formation of the Galactic Halo...Inside and Out, ASP Conference Series, Vol. 92, H. Morrison and A. Sarajedini, eds. (Astronomical Society of the Pacific, San Francisco), p. 103

Cawson, M. G. M., Kibblewhite, E. J., Disney, M. J., & Phillipps, S. 1987, MNRAS, 224, 557

Cayrel, R., Beers, T. C., Nissen, P. E., Andersen, J., Nordstrom, B., Rossi, S., Spite, F., Spite, M., & Barbuy, B. 2000, in preparation

Chiba, M., & Beers, T. C. 2000, AJ, 119, 2843

Colless, M. 1998, Wide Field Surveys in Cosmology, 14th IAP Meeting (Editions Frontiers, Paris), p. 77

Colless, M. The 2dF Galaxy Redshift Survey, [Online] Available http://msowww.anu.edu.au/~heron/Colless/colless.html, 2000

Christlieb, N., & Beers, T. C. 1999, Proceedings of Workshop on Subaru HDS

Da Costa, L. N. et al. 1994, ApJL, 424, 1

Dinescu, D. I., Girard, T. M., & van Altena, W. F. 1999, AJ, 117, 1792

Doinidis, S. P., & Beers, T. C. 1990, PASP, 102, 1392

Doinidis, S. P., & Beers, T. C. 1991, PASP, 103, 973

Eggen, O. J., Lynden-Bell, D., & Sandage, A. 1962, ApJ, 136, 748

Geller, M. J. 1990, Mercury, 19, 16

Gulati, R. K., Gupta, R., Gothoskar, P., & Khobragade, S. 1004, ApJ, 426, 340

Hartwick, F. D. A. 1976, ApJ, 209, 418

Hartwick, F. D. A. 1987, The Galaxy, Proceedings of the NATO Advanced Study Institute, G. Gilmore and B. Carswell, eds. (Dordrecht, D. Reidel Publishing Co., Cambridge), p. 281

Hearnshaw, J. B. 1986, The Analysis of Starlight (Cambridge University Press, United Kingdom)

Hearnshaw, J. B. 1987, Vistas in Astronomy, 30, 319

Hertz, J., Krogh, A., & Palmer, R. G. 1991, Introduction to the Theory of Neural Computation (Addison Wesley, U.S.A.)

Irwin, M. J., The APM Catalogue, [Online] Available http://www.ast.cam.ac.uk/~apmcat/content.html, 2000

Irwin, M. J., & Trimble, V. 1984, AJ, 89, 83

Kibblewhite, E. J., Bridgeland, M. T., Bunclark, P., & Irwin, M. 1984, Astronomical Microdensitometry Conference, NASA Conference Publication 2317, D. A. Klinglesmith, ed. (NASA), p. 277

Kurtz, M. J. 1982, Ph.D. Thesis, Dartmouth College, Hanover, NH

LaSala, J. 1994, The MK Process at 50 Years, ASP Conference Series, Vol. 60, C. J. Corbally, R. O. Gray, and R. F. Garrison, eds. (Astronomical Society of the Pacific, San Francisco), p. 312

LaSala, J., & Kurtz, M. J. 1985, PASP, 97, 605

Lindegren, L., & Perryman, M. A. C. 1996, A&ASS, 116, 579

Maddox, S. J., Sutherland, W. J., Efstathiou, G., & Loveday, J. 1990, MNRAS, 243, 692

Majewski, S. R. 1992, ApJS, 78, 87

Majewski, S. R. 1993, ARA&A, 31, 575

Masters, T. 1993, Practical Neural Network Recipes in C++ (Academic Press, Inc., San Diego, CA)

McWilliam, A., & Rich, R. M. 1994, ApJS, 91, 749

Miller, A. S. 1993, Vistas in Astronomy, 36(2), 141

Naim, A., Lahav, O., Sodre, Jr., L., & Storrie-Lombardi, M. C. 1995, MNRAS, 275, 567

Norris, J. E. 1986, ApJS, 61, 667

Norris, J. E., Beers, T. C., Ryan, S. G., & Rossi, S. 2000, in preparation

Norris, J. E., Ryan, S. G., & Beers, T. C. 1999, ApJS, 123, 639

Odewahn, S. C., Humphreys, R. M., Aldering, G., & Thurmes, P. 1993, PASP, 105, 1354

Odewahn, S. C., Stockwell, E. B., Pennington, R. L., Humphreys, R. M., & Zumach, W. A. 1992, AJ, 103, 318

Pagel, B. E. J. 1997, Nucleosynthesis and Chemical Evolution of Galaxies (Cambridge University Press, United Kingdom)

Penzias, A. A., & Wilson, R. W. 1965, ApJ, 142, 419

Perryman, M. A. C., Lindegren, L., & Turon, C. 1997, Hipparcos - Venice '97, Proceedings of the ESA Symposium, (Venice), p. 743

Preston, G. W., Shectman, S. A., & Beers, T. C. 1991, ApJS, 76, 1001

Prieto, C. A., Rebolo, R., Lopez, R. J. G., Serra-Ricart, M., Beers, T. C., Rossi, S., Bonifacio, P., & Molaro, P. 2000, astro-ph/0005598

Press, W. H., Teukolsky, S. A., Vetterling, W. T., & Flannery, B. P. 1992, Numerical Recipes in Fortran 77, 2nd Ed. (Cambridge University Press, U.S.A.), p 644

Ratnatunga, K. U., & Freeman, K. C. 1989, ApJ, 339, 126

Rebolo, R., Beers, T. C., Callende, C., Molaro, P., Rossi, S., & Bonifacio, P. 2000, in preparation

Rodgers, A. W., & Paltoglou, G. 1984, ApJL, 283, 5

Sandage, A., & Fouts, G. 1987, AJ, 93, 592

Sarajedini, A., Chaboyer, B., & Demarque, P. 1997, PASP, 109, 1321

SDSS, Sloan Digital Sky Survey, [Online] Available http://www.sdss.org, 2000

Searle, L., & Zinn, R. J. 1978, ApJ, 225, 357

Singh, H. P., Gulati, R. K., & Gupta, R. 1998, MNRAS, 295, 312

Snider, S., Prieto, C. A., von Hipple, T., Beers, T. C., Sneden, C., Qu, Y., & Rossi, S. 1999, astro-ph/9912404

SSS, SuperCOSMOS Sky Surveys, [Online] Available http://www-wfau.roe.ac.uk/sss/intro.html, 2000

Stanek, K. Z., Mateo, M., Udalski, A., Szymanski, M., Kaluzny, J., & Kubiak, M. 1994, ApJL, 429, 73

Storrie-Lombardi, M. C., & Lahav, O. 1994, Vistas in Astronomy, 38(4)

Storrie-Lombardi, M. C., Lahav, O., Sodre, Jr., L., & Storrie-Lombardi, L. J. 1992, 259, 8

Talbot, R. J., & Arnett, W. D. 1971, ApJ, 170, 409

Vieira, E. F., & Ponz, J. D. 1995, A&ASS, 111, 393

von Hippel, T., Storrie-Lombardi, L. J., Storrie-Lombardi, M. C., & Irwin, M. J. 1994, MNRAS, 269, 97

Weaver, W. B, & Torres-Dodgen, A. V. 1995, ApJ, 446, 300

Weaver, W. B, & Torres-Dodgen, A. V. 1997, ApJ, 487, 847

Zeanah, J. 2000, Private Communication

Zekl, H. 1982, A&A, 108, 380

Zinn, R. 1985, ApJ, 293, 424

Zinn, R. 1993, The Globular Cluster – Galaxy Connection, ASP Conference Series, Vol. 48, G. H. Smith, and J. P. Brodie, eds. (Astronomical Society of the Pacific, San Francisco), p. 38